EUROPEAN ORGANIZATION FOR NUCLEAR RESEARCH

CERN-EP/83-175
November 14th 1983

THE CENTRAL CALORIMETER OF THE UA2 EXPERIMENT AT THE CERN $\bar{p}p$ COLLIDER

A. Beer, F. Bonaudi, L. Bonnefoy, M. Borghini, F. Bourgeois, A.G. Clark, J.-M. Chapuis, Y. Cholley, A. Corre, G. Critin, P. Darriulat, L. Di Lella, P.-A. Dorsaz, O. Gildemeister, G. Gurrieri, J.R. Hansen, T. Himel, V. Hungerbühler[1], P. Jenni, L. Mapelli, J.-P. Marcelin, H. Pflumm, J. Ringel[2], A. Rothenberg, G. Schuler, J.L. Siegrist, A. Sigrist, P. Wicht and K. Zankel.

CERN, Geneva, Switzerland

[1] Present address : LeCroy, Research Systems SA, 27 rue Cardinal-Journet, 1211 Meyrin, Switzerland.

[2] Present address : IST GMRM, Alsfelder Str. 11, 6900 Darmstadt, West-Germany.

(Submitted for publication in Nuclear Instruments and Methods)

1 - INTRODUCTION

1.1 - Physics motivations.

The successful operation of the CERN $\bar{p}p$ Collider [1,2] provides a unique opportunity to study highly excited hadronic states with masses up to $\sqrt{s}$ = 540 GeV, ten times higher than available from previous machines. In such collisions the $W^{\pm}$ and Z^{o} bosons which mediate electroweak interactions [3] are produced at an approximate rate of two per day [4] for the present luminosity of 10^{29} cm^{-2} s^{-1}.

In the present mode of operation three equidistant proton bunches collide with three equidistant antiproton bunches in the six long straight sections of the SPS machine, of which two are available for collider experimentation. One (LSS5) is instrumented with the 2000 ton UA1 multipurpose magnetic detector [5]. The other (LSS4) houses the UA2 experiment which, despite its much smaller size and cost, is competitive in several fields [6] and in particular in detecting the electroweak bosons [7].

The UA2 detector [8], Fig. 1, covers almost the whole solid angle with the exception of two narrow cones (20^{o} half-angle) along the beams, where a system of wire chambers and scintillator telescopes is located to measure the total $\bar{p}p$ cross-section [9]. The UA2 acceptance is not sufficient to observe the full rapidity plateau populated by secondaries from normal $\bar{p}p$ collisions [10]. However, it is well suited to the study of those collisions which probe the hadronic matter at very short distances. These collisions result in large transverse momentum secondaries, which are kinematically confined to the central rapidity region. In fact all hadronic jets with transverse energies exceeding 90 GeV and $\sim$ 60% of all $W^{\pm}$ and Z^{o} decay products are contained in the UA2 solid angle.

The $W^{\pm}$ and Z bosons decay mostly into quark-antiquark and lepton-antilepton pairs. The quark-antiquark decay mode is expected to have a large branching ratio, typically 70%, and to yield two-jet final states with invariant masses equal to that of the parent boson.

The identification of these two-jet decay modes above the continuum of non-resonant two-jet events depends to a large extent upon the mass resolution which can be achieved. Even in the case of a perfect detector, the two-jet invariant mass resolution is limited by ambiguities in

assigning soft secondaries to their parent jet. Therefore, the leptonic decay modes are more convenient candidates to detect W and Z production, in spite of their smaller branching ratios. In particular, the $Z^{o} \to e^{+}e^{-}$ channel is expected to yield a virtually background-free signature. The neutrinos from $W \to e(\mu)\nu$ escape detection but the Jacobian peak in the transverse momentum distribution of the charged lepton exceeds the continuum of leptons from other sources by a factor of at least 50 [7].

The UA2 detector is instrumented to identify electrons and measure their energy over the whole acceptance but it does not detect muons. This choice was suggested by the possibility of achieving excellent energy resolution in compact electromagnetic calorimeters, whereas muon detection techniques imply the use of bulky equipment, such as thick absorbers and large magnetic field volumes, in order to achieve comparable energy resolutions. In addition, electromagnetic calorimeters acting as front sections of hadronic calorimeter cells allow for a design in which electrons and hadronic jets can be detected by the same apparatus.

This is the approach taken by UA2 in the central region, which is instrumented with a highly segmented electromagnetic and hadronic calorimeter covering the region of polar angles $40^{o} < \theta < 140^{o}$ over the full azimuth (Figs. 1-3). The calorimeter is limited to the central region because the desire to measure the important charge asymmetry predicted for $W \to e\nu$ decays at polar angles closer to the beam directions implies the use of a magnetic field to distinguish between e^{+} and e^{-}.

The present article describes the design and performance of the UA2 central calorimeter.

1.2 - General design considerations.

In the light of the physics motivations outlined in the previous subsection we now survey the main considerations which have led to the design of the UA2 central calorimeter.

A high angular segmentation is necessary to ensure an optimum separation of the particle - or jet of particles - of interest from the many other secondaries produced in the event. This is important for many reasons :

a) to resolve localised clusters of energy deposition ;

b) to provide a means of triggering on local energy depositions to discriminate against very large multiplicity events or against multiple interactions ;

c) to minimise the overlap probability of a hard π^0 with a soft $\pi^{\pm}$ which could be misinterpreted as an electron.

The requirement that a calorimeter cell and its 8 surrounding neighbouring cells should not see more than one particle on the average gives at least one hundred cells as an order of magnitude estimate of the minimum number of cells for a typical multiplicity of 12 secondaries in the calorimeter acceptance.

A single particle may deposit energy in several cells either because the lateral shower extension exceeds the cell size or because the particle trajectory crosses several cells as a result of the finite size of the $\bar{p}p$ interaction region. Here the relevant parameters are the radiation and absorption lengths of the calorimeter material, which define the lateral shower sizes, and the vertex distribution of the events (a Gaussian with $\sim$ 10 cm rms along the beam and with negligible transverse dimensions). These considerations define a minimum cell size below which there is no advantage to go. It is always possible, of course, to construct a large enough calorimeter to accomodate the desired segmentation. However, the weight and cost of the detector grow as the square of its diameter and a compromise must be found between optimum performance and the desired compactness and low cost. In the UA2 design, a segmentation of 240 cells is chosen. Each cell covers 10° in polar angle and 15° in azimuth and has its front face located 60 cm away from the centre of the $\bar{p}p$ interaction region. Each cell has the shape of a truncated pyramid with the vertex in the centre of the interaction region in order to minimise the energy sharing between adjacent cells. For reasons of convenience in light collection the same angular cell size is adopted for both electron and hadron calorimetry. As a result, while a good match is achieved between hadron shower and cell sizes, showers induced by electrons and photons have a much smaller lateral extension. This is overcome by the use of a multiwire proportional chamber located behind a 1.5 radiation length tungsten converter and in front of the calorimeter cells to provide the desired accuracy in angular measurement and to discriminate against events

in which a charged hadron and one or more photons (e.g. from π^0 decay) hit the same calorimeter cell.

The cell design aims at achieving good energy resolutions - for both electrons and hadron jets - and an efficient discrimination between electrons and hadrons. Uranium is known [11] as the optimum calorimeter material ; it allows for a most compact design and its similar response to electromagnetic and hadronic showers result in the best energy resolution attainable by calorimetry. However we did not retain it as a feasible solution because of the difficulty to purchase uranium plates machined at the appropriate sizes within reasonable time and at reasonable cost. The UA2 design uses more conventional materials ; lead for electron calorimetry and iron for hadron calorimetry, with longitudinal segmentations sufficient to ensure energy resolutions at 40 GeV of $\sim$ 2% rms for electrons and $\sim$ 10% rms for hadron jets.

Scintillator was preferred to liquid argon as being more convenient to operate in the underground area, given the constraint of having to move the whole detector between the SPS tunnel and a storage hall as quickly as possible before and after each running period. Two different types of scintillator are used in the electron and hadron compartments in order to match their respective performance requirements. Wave-length shifting plates allow for light collection from each compartment separately while minimising intercell dead spaces.

Each calorimeter cell is segmented in three longitudinal sections : the electromagnetic compartment, 17.5 radiation lengths deep, and two hadronic compartments each 2 absorption lengths deep. This segmentation gives good electron-hadron separation capability. The total cell length of approximately 4.5 absorption lengths is not always sufficient to completely contain high-energy hadronic showers and a significant deterioration of the resolution due to longitudinal escape is observed at energies exceeding 40 GeV. The segmentation of the hadron calorimeter in two individual compartments allows a partial correction for this effect.

1.3 - Outline of the article

The remaining Sections are devoted to the description of the calorimeter design (Sections 2 to 4) and performance (Sections 5 to 7).

Section 2 gives a detailed description of the calorimeter construction : mechanical structure, light collection, photomultipliers. Section 3 is entirely devoted to the various techniques implemented in order to monitor the calibration of the energy response : this is essential in order to avoid an effective deterioration of the energy resolution over long periods. Section 4 deals with the electronics systems involved in the treatment of the phototube signals. This involves both trigger electronics allowing for fast pattern recognition of simple cluster configurations and energy measurement electronics with severe accuracy and stability requirements.

The results of the energy calibration measurements obtained over 2 years of operation are presented in Section 5 and discussed in terms of stability of the response and of the ability of the calibration methods to control its variations and correct them. Sections 6 and 7 report on the performances of the electromagnetic and hadronic calorimeters, respectively. They discuss the dependence of the response upon energy, (linearity, resolution, etc...) and upon impact on the calorimeter front face (crossing intercell boundaries, dependence upon incidence angle, etc...).

Section 8 briefly describes the method of pattern recognition.

2 - CALORIMETER DESIGN AND CONSTRUCTION

We describe in this Section the implementation of the general design considerations which were presented in the Introduction.

2.1 - Mechanical structure.

A modular structure was retained to allow an efficient organisation of the various steps of the construction : machining the basic steel structures, equipping them with scintillators, phototubes, etc ... and calibrating in e^- and μ^- beams.

This implies that the modules are identical and that each module is light-tight, instrumented with an independent calibration monitoring system (see Section 3) and rigid enough to be transported without changing its characteristics. A division in 24 modules, each covering 15^o in

azimuth and including 10 calorimeter cells spanning the whole range of polar angle, was adopted.

We retained a spherical rather than cylindrical geometry (Fig. 4) to ensure that all cells are, on average, traversed at normal incidence and have their front faces at the same distance ($\sim$ 60 cm) from the calorimeter centre. Each cell covers 10^{o} in polar angle and 15^{o} in azimuth and has the shape of a truncated pyramid (tower structure) with the vertex in the center of the $\bar{p}p$ interaction region. A cylindrical geometry would imply either inclined angles between the faces and edges of the scintillator plates causing a poor light collection or in the case of edges cut perpendicularly the intercell dead space would increase considerably. Both solutions would result in a strong dependence of the light collection on polar angle. However such a dependence is also present in a spherical geometry, for which different cells have different trapezoidal cross-sections. The main disadvantage of the spherical geometry is the restriction it imposes for a given weight to the space available to the central cylindrical tracking detector.

The basic steel structure of each module (Fig. 5) consists of the 400 absorber plates of its hadronic compartments and of two 5 mm thick lids between which they are bolted in a rigid assembly. The lids extend beyond the calorimeter region to form a light-tight structure housing the light guides and supporting the phototubes. The ten electromagnetic compartments are independent units suspended from the front absorber plates of the corresponding cells. The lids do not extend into the electromagnetic region, thus allowing a smaller dead space between electromagnetic compartments of adjacent modules.

The 24 modules are assembled between two large ring structures (Figure 2) on a movable platform serving as a common support for the whole UA2 detector.

All cables of the UA2 experiment are channelled via a set of chariots suspended from overhead rails allowing for the movement of the detector from (to) the SPS tunnel to (from) the storage hall without having to disconnect any cable. The movable platform slides on air cushions : the transfer from one location to the other takes approximately two hours.

2.2 - Design considerations.

The choices concerning converter and scintillator materials, granularity (number of scintillator-converter pairs per unit length) and total cell length result from studies taking into account the state of the art [12] at the time of the design and prototype measurements performed by us using high energy SPS beams (π^-, e^- and μ^-).

The following considerations were found to be relevant :

a) Sampling fluctuations for a fully contained shower are proportional to the square root of the converter plate thickness (expressed in g/cm^2). Our prototype measurements using iron plates of 1.5, 3.0 and 4.5 cm confirmed published results [13].

b) Longitudinal shower escapes increase with the logarithm of the energy and undergo important fluctuations. In the case of the electromagnetic compartment the escape energy is measured - though less accurately - in the hadronic compartment. More relevant however is the rejection power against charged hadrons when identifying electrons.

In the case of the hadronic compartments the contribution of longitudinal shower leakage to the energy resolution of a 10 GeV shower varies from $\sim$ 3 GeV to $\sim$ 1.5 GeV when the total depth increases from 1.5 to 4.5 absorption lengths [12]. Our prototype measurements confirmed these results.

c) Light output.

The contribution of photon statistics to the energy resolution allows in principle for relatively thin scintillator plates. For example our prototype measurements on a 17 radiation length thick cell (comparing the signals from two independent wave-shifting light guides) indicate that a total thickness of 10 cm of aromatic scintillator contributes $\sim$ 1% to the resolution of a 40 GeV electron shower. However, other factors of relevance favour a large light output :

- preserving the possibility to check the energy calibration of the electromagnetic compartment with minimum ionising traversing particles;
- keeping the ratio between the scintillator signal and the contribution of Cerenkov light in the wave-shifting light guides at a high level ;
- minimising the effect of possible surface problems (optical

contact, crazing, etc ...) by using thick scintillator plates (but edge effects become in this case more important near the wave-shifting light guides).

In addition aromatic scintillators are less sensitive to radiation damage than acrylic scintillators.

The final design (Figure 6) is the result of a cost optimisation process taking into account the above factors.

The electromagnetic compartments (Figure 7) are stacks of twenty-six 3.5 mm thick lead converter plates and twenty-seven 4 mm thick PVT*) scintillator plates adding up to a total length of 20 cm (17 radiation lengths).

The two hadronic compartments of each cell consist of respectively 19 and 21, 15 mm thick steel converter plates. The total cell length (electromagnetic and hadronic compartments) is 106 cm, corresponding to $\sim$ 4.5 absorption lengths. The converter plates in the hadronic compartments are interspaced with 5 mm thick plates of acrylic scintillator **) (PMMA doped with 1% PBD, 0.1% POPOP and 10% naphtalene), wrapped in aluminium. The separation in two hadronic compartments with independent read out aims at providing information on the longitudinal shower development. For the same purpose the last three scintillator plates of the second hadronic compartment are viewed by a wave-shifting rod inserted in a 2 cm diameter hole at the center of the cell (backtag).

The total weight of a fully equipped 10 cell module is $\sim$ 4 tons.

2.3 - Light collection.

Light is collected via wave shifting light guides [14] from the two sides of the calorimeter cells which are normal to the lids of the module (Figure 8). The effect of the dead spaces which they introduce is strongly reduced by the longitudinal spread of event vertices in the Collider experiment. The light guides are inserted in intercell gaps having widths of 5.8, 10.4 and 15.0 mm between the electromagnetic and the two hadronic

---

*) NE104B, manufactured by Nuclear Enterprises, Edinburgh, United Kingdom.

**) type GS2030, manufactured by (a) Röhm GmbH, Darmstadt, West-Germany and by (b) Polivar SPA, Pomezia, Italy.

compartments respectively. They are cut from 2 mm thick acrylic plates and all sides not facing the scintillators are wrapped in aluminium. Over the length of their associated calorimeter compartments - where they act as wave-length shifters - they are doped with 90 mg/l BBQ *). The efficiency of the BBQ absorption in the wave-length shifter plate is about 80% averaged over the spectrum from the scintillator used in the electromagnetic compartments. Two thin nylon wires tightened on the cell sides prevent optical contact between the scintillator and the light guide.

The UV absorption edge of the acrylic base material has been chosen to absorb as much as possible Cerenkov light produced by traversing particles (Figure 9). For the same reason filters which transmit most of the BBQ emission spectrum but absorb shorter wave lengths (50% absorption at λ = 430 nm) are located in front of each phototube. Between these filters and the intercell plates, light is guided via twisted strips providing the desired match and made of the same acrylic material.

Light attenuation in the wave-shifting light-guides is not important in the spectral region of interest, the attenuation length being of the order of 3 m.

In the scintillator, however, we measured much shorter attenuation lengths, $\lambda_{att} \sim 27$ cm, in the relevant part of the spectrum. When exciting scintillator sample plates ($20 \times 5 \times 0.5$ cm^3) with a Ru^{106} source and collecting light via the same wave-shifting light-guide as used in the calorimeter assembly, we observed that the effective attenuation length of scintillator increases with the source to light guide distance, d. Typically, the photomultiplier signals drop by a factor of 0.7 (0.6) between d = 1 cm and d = 10 cm, and by a factor of 0.9 (0.87) between d = 10 cm and d = 19 cm for the scintillators of the electromagnetic (hadronic) compartments. This results in significant dependences of the energy response on impact coordinates (see Sections 6 and 7).

2.4 - Electromagnetic compartments.

In order to minimise intercell dead space each electromagnetic cell is assembled as an independent self-supporting stack (Figure 7) using

---

*) GS2029, manufactured by Röhm GmbH, Darmstadt, West-Germany.

the first iron absorber plate of the corresponding hadronic compartment as a base plate. The stack is pressed between this plate and two spring-loaded aluminium plates (18 mm total thickness) on its front face using two 0.5 mm thick steel side walls. In the final calorimeter assembly a 1 mm tolerance gap is left between the side walls of the cells of adjacent modules.

Each stack is machined on its four sides as a single unit, using diamond tools to produce a high quality surface finish. In order to achieve stable conditions of total and normal reflection on the scintillator faces, thin teflon (refractive index 1.34) and aluminium foils are inserted between these and the lead plates against which they are pressed (teflon facing the scintillator and aluminium facing the lead).

The segmentation of the electromagnetic calorimeter is not sufficient to provide the angular accuracy and resolving power necessary to discriminate efficiently, when searching for electrons, against events in which a charged hadron and one or more photons hit the same cell. For this purpose a preshower counter, consisting of a 1.5 radiation length thick tungsten cylinder surrounded by a 71 cm diameter multiwire proportional chamber, is inserted between the central tracking detector and the electromagnetic calorimeter. Its solid angle coverage matches that of the calorimeter.

The proportional chamber [8], the detailed description of which is beyond the scope of the present article, contains a single layer of anode wires parallel to the beam line and distant from each other by 4 mm. The cathode potential is provided by equidistant helicoidal strips at $\pm 45^{\circ}$ to the wires. We measure the pulse heights on the cathode strips and the charge division on the wires.

The resolving power thus obtained is better than 2 cm in space and the position accuracy is $\sim \pm 3$ mm.

2.5 - Photomultipliers.

The photomultipliers have been chosen to have high stability and linearity and to show negligible changes after initial turn-on and ageing. This is important to maintain a good overall energy resolution during several years of operation. Philips XP 2008 and XP 2012 photomultipliers*)

*) Manufactured by R.T.C. La Radiotechnique Compelec, Paris, France.

were retained as having satisfactory performances (Table 1) for an acceptable cost. They are 10-stage limeglass photomultipliers differing only in the nature of their 32 mm diameter photocathodes (Sb Cs type Super A for XP 2008 and Sb-K-Cs type D for XP 2012). Because of a better long range stability we equipped the electromagnetic compartments with the latter type.

The tubes were ordered socketless and used with a CERN made base in which a tube socket, the resistors of the divider chain and the signal and high voltage cables were potted with an epoxy resin.

Dark-current, photocathode efficiency and linearity were measured by the manufacturer and stability acceptance tests were performed at CERN using a semi-automatic computer controlled test-bench. Batches of 64 tubes were subject to a three day stability test. They each saw the same incandescent light to establish the desired average anode current, and the same pulsed light emitting diodes which were used to monitor the gains. A typical test result for a single tube is shown in Figure 10.

The fraction of tubes passing the acceptance tests was much higher for XP 2012 tubes than for XP 2008 tubes. Approximately 6% of the XP 2008 tubes exhibited the surprising behaviour of very occasional jumps in gain in excess of 1%. Almost all of these tubes also failed the stability test ; thus the stability test served to reject the tubes that would have shown this behaviour if we had been able to observe their response over a longer time period. After testing, the accepted XP 2008 tubes were sorted according to their stability and the better ones were used for the more important first hadronic compartments while the worst were saved for the back-tags. Retrospectively we believe that it would have been more appropriate to use exclusively XP 2012 tubes in spite of their slightly higher cost.

The tubes are placed in light-tight mountings on the module back plates (Figure 8) and pressed with springs against the associated light guides, avoiding optical contact. Each tube is surrounded by a cylindrical mu-metal shield connected to the photocathode potential.

3 - THE CALIBRATION MONITORING SYSTEM

At the $\bar{p}p$ Collider we have no source of particles of known momentum which could be used to obtain an energy calibration for each calorimeter cell. Using electron and muon beams we have calibrated all calorimeters before their installation in the experiment, as described later in Section 5, and we have monitored afterwards changes in their overall response with a calibration monitoring system.

Two methods are used to monitor the gain of the electromagnetic calorimeters as schematically shown in Fig. 11. One uses a light flash system and the other one measures the direct current induced in the photomultipliers by a movable Co^{60} radioactive source in front of the calorimeter cell. Two flash boxes allow independent illumination of the light guides and scintillator plates. The hadronic calorimeters are only equipped with one light flash system. This system, as described below in more detail , includes a light flash generator, optical fibers and two types of light stability monitors, one with vacuum photo-diodes and one with specially gain-calibrated photomultipliers (J-counters). With flash box 1, which is common to the electromagnetic and the hadronic calorimeters, we have chosen to monitor mainly the stability of the PM gains. Particular emphasis has been given to the knowledge of the energy calibration stability of the electromagnetic calorimeters, which is the major contribution to the accuracy of the mass determination for the intermediate vector bosons in the UA2 experiment. A second flash box is therefore implemented for the electromagnetic compartments to obtain a measurement of the response to light passing through a scintillator plate, converting in the wave length shifter plates and travelling back to the PM. This overall response, including the scintillator light output, is also independently measured with a Co^{60} radioactive source (Section 3.4).

The general philosophy was to provide each module with its own independent light flash system. In this way the calibration system could be operated during the calibration of each module in its final configuration except for the J-counter which was added at a later stage and which is common to all central calorimeter modules.

3.1 - The light flash generator

The light flash generator consists of a Xenon flash tube plugged into a HV pulse transformer*). A capacitor (typically 2 nF) charged at + 1.5 to 2 kV provides the flash energy. A thyristor switching + 200 V is used to produce a prepulse in the Xe bulb to ignite the light flash. The flash light is emitted into a cylindrical light scrambler box with its internal walls painted white. A blue filter selects a wave length band similar to that of the light from particles showering in the calorimeter. There is no direct light from the flash tube to the bundle of optical fibers. These accept only the light diffused from the walls of the box.

The light flash has a rise-time of 20 ns and an exponential decay time of about 150 ns. The pulse-to-pulse variations in light output are generally < 5%. In a calibration run the light flash generators of each module are operated at a frequency of about 1 Hz. The total flash calibration time (typically 3 mn . for 50 counts per flash generator) is minimized by scanning such that events from different modules are interleaved.

3.2 - The optical fibers and their light couplings.

The flash light is carried from the generator to the calorimeter cells by single polymer fibers**) with a core diameter of 0.98 mm and an external diameter of 1 mm protected by a polyethylene jacket. The fiber is rated to have a numerical aperture of 0.5, an attenuation of about 500 dB/km (at 600 nm wave length) and a minimum curvature radius of 15 mm.

The flash light from flash box 1 (Fig. 11) is carried to each light guide at the back of the calorimeter module. The light is not transmitted directly to the light guide but is sent into a thin plate of wave length shifting material (BBQ, see Sect. 2.3) which is glued onto the light guide. The BBQ plate and the light guide are in optical contact, and only the converted light reaches the PM. The fibers from the second flash box go directly to the electromagnetic calorimeter compartments. There the light is deflected from the fiber into a scintillator plate by a small

---

*) Xe flash tube EG + G FX-280 with EG + G Lite-Pac trigger FY-507.

**) FP-01 made by Fort (France).

plexiglass prism. The fiber is glued into the prism which in turn is glued onto the scintillator. Two fibers per cell bring the light to opposite sides. One illuminates a plate in the front and the other a plate in the back of the cell.

In addition to the fibers carrying the flash light to the PMs there are bundles of fibers from both flash boxes which transmit the light to the stability monitors described below. The length of an individual fiber is $\sim$ 4 m so that each of the 24 calorimeter modules is equipped with a total of about 500 m of fibers.

3.3 - The light stability monitors.

Two independent systems of light stability monitors are used to provide a normalization for the Xe flash light output.

Each calorimeter module has a diode box with three vacuum photodiodes*). These receive the flash light from both flash boxes by fibers. The applied voltage between the anode and the cathode of these diodes is 12 V. The signals are amplified in the diode box by a factor 200 with operational amplifiers. The gain of the amplifiers can be calibrated by injecting known charges at the input of each channel. This is done by charging a coaxial cable in the diode box with an external voltage and discharging it through the amplifiers using a triggerable Hg-relay switch. The diode box gives three amplified diode signals, and an OR-ed output which is used for triggering purposes.

In addition the light from one of the two flash boxes is also channelled through about 10 m of fibers to a single monitoring device, the J-counter, common to all modules. It contains a 16 × 10 × 3 cm^3 NE114**) scintillator block viewed on one side by three XP 2012 PMs. On the other side optical fibers are coupled to the scintillator via diffusing lucite cubes. These fibers are connected to fibers from the calorimeter flash light generators by means of precise cylindrical connectors with a reproducibility of the connection of better than 1%. In addition to recording independently the flash signals from the light flash calibrations the

---

*) EMI type PD1900 with S-4 cathode response.

**) Manufactured by Nuclear Enterprises, Edinburgh, United Kingdom.

scintillator can also be exposed to an accurately positioned radioactive source (150 μCi Co^{60} or 50 μCi Sr^{90}) on the fiber side. The PM signal outputs are in this case switched to a measurement of the direct currents induced by the radioactive sources. This procedure allows a gain calibration of the J-counters.

3.4 - Co^{60} source current measurements.

We also monitor the calibration of the electromagnetic calorimeter cells with a method independent of the light flash system, which consists of measuring the response to a 4 mCi Co^{60} radioactive source ($\tau_{\frac{1}{2}}$ = 5.27 years). For these measurements the PM signals are read in a direct current mode with a precise digital voltmeter. These measurements are referred to as source current measurements in the following.

The electromagnetic calorimeter cells are not directly accessible in the UA2 detector. The source is attached to a string and guided through plastic tubes of 8 mm diameter which run along the calorimeter module front faces. At the centre of each cell the source container is accurately positioned by a click-stop. The shape of the container is designed such that its orientation is reproduced for each measurement.

Contrary to the light flash calibrations, which are fully computer-controlled and fast, the source current measurements can be done only with access to the detector and require typically 12 hours for the full central calorimeter.

4 - ELECTRONICS

4.1 - Introduction.

The electronics associated with the central calorimeter must perform two main functions :

- to convert the analog signals form the PMs into digital form with the required precision and stability ;
- to provide a trigger for the physics events of interest.

A major simplification in the electronics is achieved by adjusting the gains of the PMs (see Section 5) so that their response is proportional

to transverse energy rather than energy. This results in similar pulse height distributions from all PMs of a given compartment type, because the event rates depend primarily on transverse energy, and because each calorimeter cell subtends approximately the same interval of azimuth ϕ and pseudo-rapidity η.

Since the energy deposition is proportional to the charge collected at the PM anode, we use charge-sensitive 12-bit analog-to-digital converters*) (ADCs) which integrate the input current over the gating time.

For the electromagnetic calorimeter we aim at an energy resolution of $\sim$ 2% at 40 GeV, which corresponds roughly to the expected transverse energy of electrons from W and Z^0 decay. The choice of 12-bit ADCs does not limit the resolution down to transverse energies of the order of 2 GeV, even in the presence of pedestal fluctuations of the order of one or two channels. At the same time, it allows a measurement of a transverse energy deposition as large as 80 GeV in a single cell.

Another simplification in the electronics is permitted by the mode of operation of the $\bar{p}p$ Collider itself. The two circulating beams are distributed into three short ($\sim$ 2 ns) equidistant bunches, which cross the centre of the apparatus once every $\sim$ 8 μs (eventually $\sim$ 4 μs in the six-bunch operation mode). The time of the potential events is very well defined, therefore, and it is known in advance by means of pick-up electrodes located in the machine $\sim$ 50 metres upstream of the collision point. The signals from these electrodes are sent by means of air-core cables to the counting room, where they are used to generate gate signals for all relevant electronics, including the ADCs. The triggering electronics needs about 800 ns for a first level trigger to determine if the event associated with the bunch crossing is to be kept or not. In the latter case, a general reset signal is issued 3 μs before the next bunch crossing.

In the following subsections we describe in more detail the method adopted to fan out the PM signals to the ADCs and to the trigger logic. We then discuss trigger algorithms and their implementation, as well as the method used to monitor the stability of the whole electronics chain. We finally give some details on the system adopted to supply the high voltage to the 1680 PMs of the central calorimeter.

---

*) Le Croy model 2282E.

4.2 - Signal Fan-out.

The signals from each PM are sent via two metres of miniature coaxial cable to a 20-channel terminal box mounted at the detector end of a 90 m long multicoaxial cable which transmits the signals to the counting room. There are four terminal boxes on each calorimeter module : one for the electromagnetic compartments, two for the two hadronic compartments and one for the backtags.

The multicoaxial cable consists of 20 independent miniature coaxial cables of a type chosen because of its very small ohmic resistance. This cable*), when used in association with a charge-sensitive ADC operated with a relatively long gate time (400 ns in our case) attenuates the transmitted charge by 12% over the 90 m distance.

Coaxial cables were preferred to twisted wire pairs because the impedance was found to be much more uniform.

In the counting room the multicoaxial cable is connected to the back of a fan-out module named OLIFAN [15], which transmits the signals from the 20 PMs to :

a) an ADC, via a gain 1 buffer and multicoaxial ribbon cables ;
b) another ADC, via a gain $\sim$ 10 amplifier to measure with good electronic resolution the low energy part of the spectrum. This is particularly relevant to the measurement of non-interacting minimum-ionising particles, which are used to monitor the calibration stability (see Section 5.4) ;
c) a monitor output via a gain 1 buffer, for easy oscilloscope inspection of the individual PM signals ;
d) an integrating sample-and-hold amplifier (ISH) [16], which adds the two PM signals from the same cell, integrates the resulting signal and transmits it to the trigger electronics (see Section 4.3) ;
e) an output of a fast analog sum of the 20 input signals (Σ).

There are three OLIFAN modules for each calorimeter module, one for the electromagnetic compartment and one for each hadronic compartment.

---

*) Cable 0.5 1/1.5 - 50 ohms, made by Felten & Guillaume A.G., West-Germany.

The 10 backtags share an OLIFAN with the 10 backtags of an adjacent calorimeter module.

The OLIFAN uses the mechanics of a double-width CAMAC module. It consists of a printed circuit (PC) board, into which are plugged 20 small PC boards (one for each PM signal) containing the two gain 1 buffers and the gain 10 amplifier, and another 10 small PC boards containing the ISH amplifiers. The OLIFAN modules used for the electromagnetic compartments are fully equipped with all of these small PC boards ; those for the hadronic compartments and the backtags contain only the two gain 1 buffers.

The OLIFAN needs two NIM level signals to gate and clear the ISH amplifiers.

A schematic diagram of the electronics which receive the two PM signals of a single electromagnetic compartment is shown in Fig. 12.

4.3 - Trigger Electronics.

The trigger algorithms are largely dictated by the physics events of interest.

The Z and W triggers are based exclusively on the information from the electromagnetic compartments of the calorimeter. Because of the transverse dimensions of the cells, there is an appreciable probability that an electromagnetic shower from an electron is shared among neighbouring cells. Trigger thresholds must be applied, therefore, to linear sums of signals from neighbouring cells, rather than to each individual cell. For this reason the signals from all possible 2 × 2 clusters of neighbouring cells are linearly summed ; each cell contributes to four clusters, with the exception of the 48 edge cells which contribute to two clusters only.

The Z and W triggers are implemented in the hardware by means of special modules called ROLAND [15]. Each ROLAND (a double-width CAMAC module) receives the 20 ISH voltage levels generated by the two OLIFAN modules associated with two adjacent calorimeter modules. These voltage levels, which are kept constant to better than 20 mV for a maximum of 3 μs, are proportional to the transverse energy deposited in a cell and saturate above 25 GeV.

The front end of a ROLAND module sums up the ISH levels of adjacent

cells in 2 × 2 clusters by means of a resistor network. Each summed voltage level so obtained is then compared to a reference voltage V_{ref}, which is common to all 9 clusters of a ROLAND and to all ROLAND modules. V_{ref} is generated by a fast 8-bit digital-to-analog converter (DAC), with a settling time of less than 10 ns, which is controlled by a synchronous counter. A one-bit step of the DAC corresponds to about 100 MeV of transverse energy. Loading any digital value into the counter results in applying a common threshold to all clusters. Any cluster exceeding this threshold sets an associated flip-flop, and the state of all flip-flops is sent to the decision-making electronics, which is implemented in MBNIM standard [17]. The OR of the 9 flip-flops in a ROLAND module is also available as a NIM output level. Several thresholds can be applied in sequence with a frequency of 10 MHz.

The ROLAND modules can also be used as fast ADCs, capable of converting all clusters simultaneously to 8-bit numbers in 2.5 μs. For this purpose the synchronous counter is loaded to the highest possible value and then required to count down. Whenever a flip-flop is set during the count-down, a shift register is loaded with the value of the counter, memorising the digital value of the cluster transverse energy. The counter value is converted to Gray code before memorisation in order to avoid errors due to synchronisation problems. A simplified block diagram of a ROLAND module is shown in Fig. 13.

Figure 14 shows the trigger timing. After gating the ADCs and the ISHs, a first threshold (corresponding to $\sim$ 3.5 GeV) is applied to all ROLAND modules, and the decision making digital electronics test if there are at least two clusters above threshold, separated in azimuth by at least 60°. This is the so-called Z-trigger, which is recorded in a MBNIM strobed coincidence register used as a memory.

About 100 ns later a second, higher threshold (corresponding to a transverse energy of $\sim$ 8 GeV) is applied, and at least one cluster is required to set the so-called W-trigger bit.

Other triggers are implemented using conventional NIM electronics : in particular, a total hadronic transverse energy trigger is defined by linearly summing all of the Σ signals provided by the OLIFAN modules and requiring that the resulting signal exceeds a given threshold (typically set at 35 GeV). This trigger, as well as triggers involving other parts

of the UA2 detector , set bits in the same MBNIM strobed coincidence register recording the Z- or W-bits. After 800 ns a decision is taken on whether to keep or reject the event, based on the pattern of trigger bits and on a computer defined trigger-enable mask. More details on the UA2 triggers can be found elsewhere [15].

If the event satisfies the trigger requirements, all clusters in the ROLAND modules are converted to digital values in 2.5 μs, as described above, before reading out the event.

4.4 - Calibration Electronics.

The requirement of good energy resolution implies strong constraints on the stability of the electronics because of the long data taking periods.

The solution to this problem adopted in the UA2 experiment consists in monitoring the gains of all electronic channels by means of a number of precision pulse generators (PPG) which inject a known charge into each PM channel on the detector side. In this way gain variations can be followed and corrected for, by performing calibration runs as often as needed and in particular whenever an electronic component is replaced in a given PM channel after a failure.

The PPGs perform also the functions of calibrating the attenuation of the signal cables, measuring the gain and linearity of the combined OLIFAN-ADC system, and testing the trigger logic.

There are 24 PPGs, one for each calorimeter module, which are installed on the detector support structure. A PPG is a single-width CAMAC module which consists of 8 independent pulse generators, one for each group of 10 PMs, producing signals with a pulse shape similar to that of real PM signals.

These signals are obtained by discharging a cable of known length charged up to a known variable voltage V_o, by means of a Hg relay. The charge is injected into a group of 10 channels by a passive splitter made of 500 Ω high precision resistors mounted in the terminal box on the detector end of the 90 metre long signal cables (Fig. 12). The common point of the splitter is connected to ground for normal operation to avoid cross-talk among the channels ; however during calibration this ground connection is removed by a relay switch.

A PPG module contains also a triggering circuit to provide a gate for the ADCs and the ISH amplifiers.

The maximum operation frequency of the PPG is about 100 Hz. A PPG calibration run consists in measuring and analysing the response for typically 14 different values of V_o chosen such that the signals cover the full ADC range. Accumulating 20 counts per voltage step the total PPG calibration time for all PM channels is about 40 minutes. The measurements are repeated typically once per week.

The xenon light flash system described in the previous section is controlled by CAMAC modules called CALIBUA2 located on the detector support structure. One double-width module CALIBUA2 controls six light flash generators and three diode boxes, corresponding to three calorimeter modules. It contains the trigger outputs for the flashers and the Hg relays for the charge injection into the diode amplifiers, the low voltage supplies for the diode boxes, and the discriminator part for the diode OR signals. The ORs of the three calorimeter modules can be OR-ed further with other CALIBUA2s or PPGs to provide the UA2 master logic with a global calibration trigger signal.

The electronics associated with the light flash system is located together with the PPG modules in CAMAC crates near the calorimeter. The main online computer*) controls the calibration electronics via a single standard long distance link.

4.5 - High Voltage System.

A very simple method to supply the high voltage (HV) to the 1680 PMs of the central calorimeter has been adopted in the UA2 experiment.

This method consists of using a small number of "master" HV power supplies and a high stability voltage dropping resistor in series with each PM voltage divider. The values of these resistors are determined during the initial calibration of the calorimeter modules (see Section 5).

The obvious advantages of this method are simplicity and low cost ; however, it lacks the flexibility of other HV systems, in which the voltage can be easily varied for an individual channel whenever needed.

---

*) VAX 11/780, Digital Equipment Corporation, Maynard, Massachusetts, USA.

Four master HV supplies*), capable of delivering 600 mA at 2000 V are used together with 24 HV distributors, one for each calorimeter module, which are located in the counting-room. The voltage from each master supply (-1900 V) is daisy-chained through six distributors.

Each HV distributor contains 10 plug-in cards, one for each cell. A card supplies the HV to the seven PMs of a cell by means of seven independent channels, each consisting of two 1% high-stability series resistors which are plugged into the card. It is possible to change the total value of the voltage dropping resistance in steps of 1 kΩ, which correspond to ∿ 1 V steps in the PM cathode voltage.

If the current drawn by any one of the seven channels in a card exceeds a threshold of 3.5 mA (the value for normal operation is ∿ 1 mA), a relay cuts the HV on the card and an alarm signal to the computer is generated. When this happens, the faulty channel is identified by light-emitting diode on the front panel of the HV distributor, and the corresponding voltage dropping resistor can be removed until the fault is repaired.

The 70 HVs are fed to a calorimeter module by means of 4 multi-conductor cables**).

The experience gained during two running periods at the $\bar{p}p$ Collider in 1981 and 1982 has shown that this system works well.

5 - ENERGY CALIBRATION AND STABILITY

5.1 - Introduction.

One of the main goals of the UA2 experiment is the detection of the decay $Z^o \to e^+e^-$ and a measurement of the Z^o mass and width, which are predicted to be about 94 and 3 GeV/c^2 respectively. This requires an initial calibration of the electromagnetic compartments with a precision of the order of 1%. Furthermore, because of the very low event rate (of the order of few $Z^o \to e^+e^-$ events per running period of three months) the calibration constants must be known with comparable precision over periods

*) Type HTN 1200M-2000 made by FUG, West-Germany.

**) Cable made by Thomson Brandt, France.

of time as long as several years.

For the hadronic compartments the constraints on the calibration are less severe, since the energy resolution is only $\sim$ 10% at 40 GeV. However, the possibility to observe peaks in the two-jet invariant mass distribution due to the hadronic decays of the intermediate vector bosons still requires precisions of the order of 2 to 3%, and stabilities of the same order of magnitude.

In this section we describe the procedure followed to calibrate the central calorimeter with the required accuracy, and we present results on the calibration stability observed during a period of almost two years of operation. We also give a description of the beam set-up used in the initial calibration and in additional studies of the calorimeter performance reported in Sections 6 and 7.

5.2 - Test Beam Set-up.

The 24 calorimeter modules were all calibrated before installation in the UA2 apparatus using a 10 GeV beam of negative particles from the CERN PS.

The beam particles (mostly π^-) were defined by a telescope of scintillator counters which included an air light-guide circular scintillator with a diameter of 15 mm. A 1.5 radiation lengths thick tungsten plate followed by a scintillator counter equipped with pulse height measuring electronics was installed behind the circular counter just in front of the calorimeter module, in order to simulate the cylindrical tungsten converter actually used in the UA2 experiment (see Section 2.4).

Electrons in the beam were identified by a coincidence of two 4 m long gas Cerenkov counters filled with helium at a pressure of 2.5 atmospheres. These electrons were used to calibrate the electromagnetic compartments of the calorimeter, as discussed in the next Section.

The calibration of the hadronic compartments was made using the muons contained in the beam. These muons were identified by removing the two Cerenkov counters from the coincidence and replacing them with a signal from a scintillator counter behind a 2 m thick iron wall.

The value of the beam momentum was measured directly by magnetic deflection to be 10.10 GeV/c, with a systematic uncertainty of $\pm$0.05 GeV/c.

Practically the same set-up was also used at the SPS for the studies of the calorimeter performance described in Sections 6 and 7. Some of these measurements needed a better space resolution for the incident beam particles than that of the 15 mm diameter circular counter. In these cases, this counter was replaced by a pair of 2 mm wide finger counters at 90° to each other.

Collimators on the incident beam line were used to keep pile-up effects at a negligible level.

5.3 - Initial calibration.

In order to calibrate the calorimeter and adjust the PM gains, each module was mounted on a motorized table, which could be moved by remote control so that the axis of each cell could be aligned with the beam. The same electronics and cables as at the $\bar{p}p$ Collider were used in these measurements.

As mentioned in Section 4, the gain of each PM was adjusted so that the charge measured by the corresponding ADC was proportional to transverse energy. This calibration constant was chosen to be 0.08 GeV/pC for all three compartments of a cell, so that the largest measurable transverse energy deposition in an individual compartment was 80 GeV.

The calibration procedure for the electromagnetic compartments consisted of varying the PM high voltage by means of a computer controlled high voltage power supply until the most probable charge measured by the ADC was given by

$$Q_0(\text{pC}) = 12.5\ E(\text{GeV})\ \sin\theta \qquad (1)$$

where E is the most probable energy deposition in the electromagnetic compartment expected for the beam electrons, and θ is the polar angle of the cell centre when the calorimeter module is mounted in the UA2 experiment.

In pratice the voltage adjustment procedure was stopped when the most probable charge differed from Q_0 by $\lesssim$ 2%. At this point the information from a sample of $\sim$ 2000 electrons and $\sim$ 500 flash triggers was written onto magnetic tape for a further more refined off-line determination of the calibration constants.

The calibration of the hadronic compartments was made using the muons contained in the beam. Muons were preferred to hadrons in spite of their lower flux because they gave rise to a narrow pulse height spectrum in each compartment. Hadrons, on the contrary, gave energy depositions in each compartment having a much broader spectrum, which furthermore depended upon the cell size because of the large transverse dimensions of the hadronic showers at 10 GeV.

The equivalent muon energy deposition in the two hadronic compartments and in the backtags had been previously determined in special studies performed at the CERN SPS (see Section 7), by comparing the calorimeter response measured with hadrons of known energies, to that measured with muons. The values adopted were 0.453 and 0.698 GeV in the first and second compartment, respectively, for all cells.

Because of the chosen calibration constant of 0.08 GeV/pC, muon peaks would occur around channel 20 in the ADCs and a precise determination of the peak positions would be difficult. Therefore an amplifier with a nominal gain of 12 was inserted for the calibration on each hadronic channel and its exact gain value was determined by means of the electronics calibration system described in Section 4.4 . To avoid pile-up effects arising from the large number of hadrons in the beam, which produced signals saturating the electronics in the presence of this additional gain, a 1 m long copper block was inserted in the beam upstream of the calorimeter module to absorb most of the incident hadrons.

The calibration procedure was similar to that of the electromagnetic cells. Special flash runs were taken with these amplifiers by-passed to avoid saturation of the electronics.

In the case of the backtags the PM gains were adjusted so that the muon peaks corresponded to a charge of 2 pC at the ADC inputs for all cells.

As a final check of the high-voltage setting the calorimeter module was connected to the high-voltage system described in Section 4.5 and measurements with incident electrons and muons were again performed for each cell.

5.4 - Calibration stability measurements.

The initial calibration of all 24 calorimeter modules in the 10 GeV CERN PS beam was performed between the end of 1980 and March 1981. The only calibration system implemented at that stage was the light flash generator with the vacuum photodiodes as a light monitor. The first 20 calorimeter modules, complemented with the facility to make Co^{60} source current measurements and the addition of the J-counter as second light monitor, were then assembled into the UA2 detector during Summer 1981. The initial source current calibration of the electromagnetic calorimeters could be made in November 1981 shortly before the first $\bar{p}p$ running period of the SPS Collider.

The 4 remaining calorimeter modules were periodically recalibrated at intervals of a few months in beams both at the CERN SPS and PS, using all components of the calibration system. These measurements, obtained up to now over a period of about two years, as well as systematic Co^{60} source current measurements and studies of the energy response in minimum-bias $\bar{p}p$ events for all calorimeter modules are used to study in detail the long-term stability of the calorimeter response and the ability of the calibration system to correct for the observed changes in the energy calibration.

A further check on the stability has been performed in December 1982 with the recalibration of 4 calorimeter modules which were dismounted from the UA2 detector after the 1982 running period of the $\bar{p}p$ Collider. These last measurements also provide information on possible radiation damage during Collider operation.

The result of the recalibration measurements with the 8 modules is that we have observed a decrease of the overall calorimeter response to particles of a given energy. For each module the average drift in the electromagnetic calorimeters for 10 GeV electrons in shown in Fig. 15a. It amounts to $-6.7 \pm 0.3\%$ per year on average. No significant difference is seen between the modules which have been used in the UA2 detector during $\bar{p}p$ Collider runs and the others. This observation excludes a large contribution from radiation damage, in agreement with the results of Co^{60} source current measurements performed before and after $\bar{p}p$ runs. They showed an additional drop of typically 2% per two-month running period.

The distribution of the ratio R_{em} of the response to 10 GeV electrons in the last recalibration to that in the initial beam calibration is shown in Fig. 15b for all 160 PM channels contributing to Fig. 15a. The two measurements are separated by about 2 years. The rms value of only 3.0% indicates that the observed loss in sensitivity ($R_{em} < 1$) is affecting all the channels in a similar way, with the exception of 4 of them for which either a mechanical or an optical damage of the light guide has been found to be responsible for very large drops of sensitivity ($R_{em} < 0.75$).

The decrease of the electromagnetic calorimeter response has occurred in a uniform way during the two years, as established by the periodic calibration runs on the 4 modules not yet installed in the UA2 detector as well as by several Co^{60} source current measurements on all the modules.

A similar result, albeit more pronounced and with larger channel to channel and module to module fluctuations, is observed for the hadronic calorimeters. Fig. 16 shows the average drop per module for both hadronic compartments. The average drop in R_{had}, the ratio of the response for 10 GeV muons in the last calibration runs to that in the initial beam calibration, is typically 10% per year, but with non-statistical module-to-module differences (see below). The rms value for the distribution of R_{had} within a compartment of a module (20 channels) is typically 8%.

A direct measurement of the calibration stability for each calorimeter module is also obtained from the average energy flow observed in minimum-bias $\bar{p}p$ events. As an example , Fig. 17 displays the transverse energy distribution ΣE_T in the first hadronic compartments summed over all eight non-edge cells of a given module. The energy flow method consists of measuring the fraction p of events having $E_T^{min} < \Sigma E_T < E_T^{max}$. A calibration error δ would change the measurement of ΣE_T to $(1 + \delta)\Sigma E_T$ and result in a value p different from p_0, where p_0 corresponds to the true ΣE_T distribution. The relation between δ and p/p_0 is a function of E_T^{min}, E_T^{max} and of the shape of the true ΣE_T distribution. The optimum E_T range depends on the available statistics ; $E_T^{min} = 0.5$ GeV and $E_T^{max} = 1.5$ GeV have been chosen for this analysis. The measurements from the modules recalibrated in December 1982 in a beam of known energy have been used to define the true ΣE_T distributions and the values of p_0. The accuracy of the energy flow method turns out to be limited by systematic

effects rather than by statistics. A relative comparison of two measurements, one from the beginning of the 1983 $\bar{p}p$ run and the other one from the end, is shown in Fig. 18. The systematic uncertainties on δ, mainly due to instabilities of the electronics (pedestals) and errors in the selection of minimum-bias $\bar{p}p$ events, are estimated to be less than 2% with module-to-module rms spreads of 1.5, 2.0 and 3.0% for the electromagnetic, first and second hadronic compartments, respectively. Within these uncertainties the results from the energy flow measurements agree with the drop of the calorimeter response observed with the modules recalibrated in the beam.

There are many possible sources for the observed deterioration. Electronics effects can be excluded to the level of < 0.3% by the charge injection system (PPG, Section 4.4). The HV of the PMs has been controlled by checking the HV dropping resistors and by adjusting the HV provided by the bulk supplies to < 0.2 V. The PM gain variations due to the supply HV changes are thus limited to < 0.2%. It is difficult to determine separately the time dependence of the various factors contributing to the overall calorimeter calibration : scintillator response and its light attenuation, wave length shifter (BBQ) behaviour including absorption, emission and light attenuation, losses in the light guides, PM photocathode response and gain, and all the optical couplings between these components. Two contributions have been evaluated, which however are not sufficient to explain the whole effect. From the information collected with the light flash system, where the light from flash box 1 probes mainly the PM response (see Fig. 10), one can conclude that the XP 2012 PMs used for the electromagnetic claorimeters have been stable to within ±2% per year whereas the XP 2008 PMs used in the hadronic calorimeters have shown a gain drift of $-4.7 \pm 2\%$ per year.

The light attenuation in the scintillator of the electromagnetic compartments has been measured in a few cells by varying the impact point of the beam particles over the front face (see following Section). The measured decrease with time of the effective absorption length can only account for a drop of $2 \pm 1\%$ per year.

The acrylic scintillator for the hadronic compartments has been supplied by two manufacturers (see Section 2.2). Different ageing properties have been observed : the response of the hadronic calorimeters

containing scintillator (a) has been measured by the energy flow method to drop on average 15% per year whereas modules equipped with scintillator (b) age at a slower rate (8% drop per year on average). The same behaviour has been observed in beam recalibrations where module number 1 of Fig. 16 is equipped with scintillator (a) and the others with (b).

From the recalibration measurements one can evaluate the performance of the different components of the calibration system, choose an optimal procedure to correct for the drifts in the calorimeter response, and determine its parameters. We note first that the vacuum photodiodes, which are part of the light stability monitors, do not exhibit the desired long-term stability. In fact drifts (or even sudden jumps in some cases) as large as 10% per year have been observed in the ratios of the signals from the three diodes which monitor the same flash light generator. The diodes are only used for relative normalizations over short periods (within one flash run). The second light stability monitor, the J-counter, with its own calibration through Co^{60} and Sr^{90} source current measurements, shows an intrinsic instability of $< 1\%$ per year. However its response to the different modules shows fluctuations around this value which build up to a rms of 2.5% per year. The result is worse if the layout of the fibers or their connections are changed. The corrections using flash box 2, which sends the light to scintillator plates of the electromagnetic compartment, overestimate the drop in the calorimeter response by about a factor of two. This could be due to a deterioration of the light coupling of the fibers to the scintillator. Even though the results from flash box 2 cannot be used over long time periods they most conveniently correct for short-term fluctuations in the electromagnetic calorimeters. The systematic error from the use of flash box 2 over a period of two months is $\leqslant 1\%$. The most satisfactory results in reproducing the calibration changes have been obtained with the Co^{60} source current measurements in the electromagnetic compartments. This method reproduces the energy measurements for 10 GeV electrons to better than 1% per year with a channel-to-channel rms of 1%. Finally, the information from the energy flow method is of particular interest for the hadronic compartments where no source current measurement is available.

We have therefore adopted the following procedure to correct for the time evolution of the calibration.

For the electromagnetic channels :

i) an average correction modulated by small adjustments from the energy flow measurements is applied for the time interval between the initial beam calibration and the first Co^{60} source current measurement ;

ii) Co^{60} source current measurements are performed at least once before and after each $\bar{p}p$ Collider period and their results are used to follow the calibration evolution ;

iii) between these measurements flash runs are made, typically once a day during data taking periods, to correct for short-term fluctuations ; the J-counters are used as relative flash light monitors ;

iv) samples of minimum-bias $\bar{p}p$ events are recorded during the entire $\bar{p}p$ Collider periods and used to survey the calibration with the energy flow method.

For the hadronic calorimeters we use for the absolute normalization averaged over each module the results of the energy flow method. The results of the flash light system (flash box 1) are taken into account to correct for individual channel-to-channel fluctuations within each module in a relative way.

The result of this correction procedure, covering a time interval of about two years, is shown in Fig. 19 for the electromagnetic calorimeters (before applying the energy flow corrections). Shown is the ratio R_{em}^{corr} of the corrected response for 10 GeV electrons in the last recalibration to that in the initial beam calibration. The average value per module is displayed in Fig. 19a and the distribution for the individual channels is given in Fig. 19b. One of the four modules used in test beams is excluded here because its initial Co^{60} source current measurement was made much later than for the others. We find in Fig. 19 a mean value $< R_{em}^{corr} > -1 = -1.9 \pm 0.3\%$ with a channel-to-channel rms spread of 2.2%.

The initial and the last recalibrations have been performed in different test beams. We have measured for both beams the absolute momentum setting with a beam spectrometer using the same reference magnet with a known bending power. The systematic uncertainty of R_{em}^{corr} from the absolute beam momentum is estimated to be $\pm 0.8\%$. A further systematic error comes from the average correction applied for the time interval between the initial beam calibration and the first Co^{60} source current measurement. The value used in Fig. 19 was obtained from measurements of three modules in a beam during the first six months after the initial beam calibration. Their

systematic uncertainty contributes ±1.4% to R_{em}^{corr}. Adding the two contributions in quadrature, we estimate the systematic error on R_{em}^{corr} at this stage to be ±1.6%. Note however that due to the fact that all modules exhibit a statistically consistent result (Fig. 19a) we can use the latest recalibration measurements to set the normalization for the corrections from the energy flow measurements. Including these corrections we obtain $< R_{em}^{corr} > -1 = -0.3 \pm 1.0\%$ with a rms channel-to-channel spread of 2.8%. The systematic uncertainty on the absolute calibration of the electromagnetic calorimeters is then reduced to less than ±1.5% after two years of operation.

The results of the calibration corrections for the hadronic compartments are shown in Fig. 20 where R_{had}^{corr} is the ratio of the corrected response to 10 GeV muons in the last calibration to that in the initial calibration. The mean value for both compartments is $< R_{had}^{corr} > -1 = 1.5 \pm 1.1\%$ and the channel-to-channel rms spread is 8%. We use these recalibration measurements and the results from the energy flow method as an estimate of the systematic uncertainty on the absolute calibration of the hadronic calorimeters. The systematic uncertainty is less than ±3.5%.

A further check on the calibration has been obtained from the energy deposition of non-interacting minimum ionizing particles produced in $\bar{p}p$ collisions (Fig. 21). The most probable energy loss in each electromagnetic cell type has been determined to within ±2.5%. After applying the calibration corrections it agrees well with the values chosen in the initial beam calibration.

The results from the calibration stability measurements can be summarized as follows. After more than two years of operation the systematic uncertainties in the absolute energy scale are less than ±1.5% for the electromagnetic and less than ±3.5% for the hadronic calorimeters, with channel-to-channel rms spreads of 3% and 8%, respectively. The main uncertainties of the calibration are due to the drifts which have occured during the time between the initial calibration in the beam and the first Co^{60} source current measurements (electromagnetic compartments) and the first energy flow measurements (hadronic compartments). The complete calibration procedure, when applied after a full recalibration of all calorimeter modules in a beam, would improve the above values to ±1% (±2%) for the absolute energy scale of the electromagnetic (hadronic) calorimeters with channel-to-channel rms spreads of 2% and 3%, respectively.

6 - PERFORMANCE OF THE ELECTROMAGNETIC CALORIMETER

6.1 - Introduction.

A detailed knowledge of the behaviour of individual cells of the electromagnetic calorimeter is essential, if the performance criteria discussed in Section 1 are to be achieved for the study of intermediate vector bosons and jets.

As an example, the effective resolution for very high-energy electrons is determined not by the intrinsic resolution $\sigma/E \sim 0.14/\sqrt{E}$ (E in GeV), but by systematic effects such as :

i) an accurate knowledge of the dependence of light response on the position and angle of track impact in a given cell,

ii) a knowledge of the response linearity with respect to electron energy,

iii) the reproducibility of response in different cells of the calorimeter.

As described in Section 2, the 240 cells of the electromagnetic calorimeter are divided into 5 cell shapes. In each cell type, light is collected from trapezoidal scintillator plates as shown in Fig. 22. The angle α in Fig. 22 varies from 5.3° for the smallest cell to 0.7° for the largest one ; this implies different light-collection properties for each cell type.

The response with respect to beam impact position, beam incidence angle and beam energy, has been studied at the CERN PS and SPS using electron beams of momenta between 1 and 70 GeV/c ($\Delta p/p \sim \pm 1\%$). In these measurements, up to 5 examples of each cell type were used, to estimate cell-to-cell variations of the calorimeter response.

In the following subsections, BBQ_s and BBQ_ℓ are used to represent the light collected by respectively the smaller and larger BBQ-doped light-guides. As shown in Fig. 22, x (mm) and ϕ (degrees) are used to define the position of beam impact at the front face of the calorimeter. In all measurements, the beam configuration and data-collection electronics were as described in Section 5.2. The signal given by the scintillator behind the tungsten converter was required to exceed 4 equivalent minimum ionising particles to minimise the incident hadron background.

6.2 - Dependence of light response and resolution on energy.

Measurements of the light response and of its resolution were made in several examples of each cell type, using electrons passing through the centre of each cell.

Figure 23 shows the deviation of the response from linearity. The associated error-bars represent the rms spread of individual measurements, for all cell types. The corrected energy

$$E_{corr} = 1.024\ E_{meas} / [1 + 0.01\ \ell n(E_{meas} + 1)] \quad (E \text{ in GeV})$$

can be measured to better than ±1% on average.

Figure 24 shows the energy resolution for electrons passing through the centre of each cell for different positions of the tungsten converter. A resolution $\sigma/E \sim 0.14/\sqrt{E}$ (E in GeV) approximately describes these measurements. The beam resolution ($\Delta p/p \sim \pm 1\%$) has not been unfolded.

6.3 - Impact dependence of the response to electrons.

The response of the electromagnetic calorimeter depends on the impact position of electrons on the calorimeter, because of a number of factors :

i) As a result of the trapezoidal shape (Fig. 22) of scintillator plates, more light is collected by the large light-guide than by the smaller one. Light reflecting from non-parallel edges has its effective internal reflection angle changed by $(+2\ n\alpha)^{o}$ or $(-2\ n\alpha)^{o}$ for respectively the large and small light guides (n being the number of reflections from non-parallel edges). All non-absorbed light reflecting from the scintillator edge of the small light guide will eventually enter the large light guide.

ii) As noted in Section 2.3, the attenuation length of the scintillator has a strong wavelength dependence. As a result the light attenuation curve ($< \lambda_{eff} > \sim 25$ cm) is non-exponential, light of shorter wavelengths being absorbed closer to the point of electron impact.

iii) Close to a cell edge, some shower energy escapes into adjacent cells and along inter-cell gaps. By including the neighbouring cell energy most energy is recoverable, but for impacts close to a cell edge ($\lesssim$ 5 mm) special corrections must be applied (see Section 6.6).

In this Section, we describe the results from spatial scans of several cells of each type using normal-incidence electrons.

In all spatial scans on different cells of the same type, measurements were reproducible with an rms spread of < ±1%. Nevertheless significant variations of the uncorrected light response exist as a function of the beam impact position in a cell. For example, Figs. 25a to 25c show typical measurements in cell type 3 (intermediate size) ; the light response is shown for the small light-guide (BBQ_s), the large light guide (BBQ_ℓ), and $BBQ_{s\ell} = \sqrt{BBQ_s \cdot BBQ_\ell}$.

Light response variations have been corrected in each cell type by a parametrisation

$$BBQ\ (corrected) = BBQ(raw) \cdot \exp\left[f(x, |\phi|)\right]$$

where $f(x, |\phi|)$ is a polynomial of 3rd degree in x and of 2nd degree in $|\phi|$. Polynomial coefficients have been evaluated in each cell type, for each of BBQ_s and BBQ_ℓ. The corrected energy response, for 10 GeV electrons normally incident on cell type 3, is shown in Fig. 26. The rms spread of corrected energy response is always < ±1.7% for a given cell type ; in only 2 cases is the spread > ±1%.

If a single particle enters the calorimeter cell, the variation of light response allows an accurate measurement of the impact position along a contour of constant $R = BBQ_s/BBQ_\ell$. If in addition either ϕ or x of the incoming particle is measured (in the case of the UA2 experiment either by the central tracking detector, or by the preshower chamber following the tungsten converter), the impact point is accurately determined, and the response $BBQ_{s\ell}$ can be evaluated to better than $\sim$ ±1%. The rms spread of the evaluated impact position, with respect to that externally measured, is shown in Fig. 27. If no external track measurement is provided, the accuracy of energy measurement is limited to the variation of $BBQ_{s\ell}$ along a contour of constant R.

In Fig. 28 the energy resolution is shown for the $\phi = 0$ plane. The resolution is unaffected by the beam impact position, except within $\sim$ 5 mm of the cell edge. The typical resolution, $\sigma/E = 0.16/\sqrt{E}$, is larger than the value previously quoted because energy leakage of the electromagnetic shower into the hadron compartments has not been taken into account in this Figure.

6.4 - Longitudinal shower development.

The longitudinal shower development has been studied using electrons of between 6 and 70 GeV. For 10 GeV electrons of normal incidence at the cell centre, a typical distribution of energy deposited in the hadron calorimeter is shown in Fig. 29. The tail of large energy deposition in the hadron calorimeter results in part from a small π^- beam contamination. Relevant to calorimeter operation in the UA2 environment is the fraction of true electrons depositing less than a given energy in the hadron calorimeter. Results are shown in Fig. 30 ; at 70 GeV electron energy, 95% of all electrons deposit less than 11% of their energy in the hadron calorimeter. At all electron energies, the deposition of energy in the second hadron compartment is negligible.

For normal-incidence electron impacts of more than 10 mm from a cell edge, the leakage of shower energy into the hadron calorimeter is little changed from the above results, as shown in Fig. 31. The leakage remains small for distances of more than 5 mm from the cell edge, and can be parametrised.

6.5 - Lateral shower development.

Because of the small lateral extension of electromagnetic showers, electrons of normal incidence at the centre of a cell lose less than 1.5% of their energy into surrounding cells. However, from a measurement of the energy deposited in adjacent cells when electrons enter the cell near an edge, it is possible to estimate the mean lateral shower extension. Figure 32 shows the fractional energy escape for 2 electron scans across a cell interface :

i) a 10 GeV-electron scan, laterally (x) across the light guides,

ii) a 40 GeV-electron scan, vertically (ϕ) between two cells of the same type.

In each case, a good agreement with the data is obtained from a parametrisation

$$f = 0.5(1.0 + e^{-\xi/R_1})^{-1} + 0.5(1.0 + e^{-\xi/R_2})^{-1},$$

where $R_1 = 2.11 \pm .08$ mm,

$R_2 = 8.64 \pm .24$ mm,

and ξ (mm) is measured with respect to the centre of the intercell gap.

This parametrisation can be used in actual $\bar{p}p$ operation of the UA2 experiment to compare the measured energy distribution in a cluster of electromagnetic cells (see Section 8) with that expected from a single electron or photon. From the knowledge of the track impact position in the calorimeter we predict the energy fractions deposited in the hit cell and the surrounding ones and compare them with the actual measurements by defining a quality factor :

$$q = \sqrt{\Sigma \left[E_i \text{ (predicted)} - E_i \text{ (measured)}\right]^2} / \Sigma E_j \text{ (measured)},$$

where i extends over all cells of the energy deposition with non-zero measured or predicted energy, and j extends over those cells with measured energy. Figure 33 shows a typical q distribution for normal incidence electrons of 10 GeV. Figure 34 shows the value of q exceeded by 5% (10%) of the 10 GeV electrons (the limits shown decrease slightly with increasing electron energy).

6.6 - Light response near a cell interface.

To study the light response near a cell interface (a 4.6 mm gap housing the light guides), a scan was made between cell types 3 and 4, using a 2×2 mm^2 beam of normal incidence 10 GeV electrons. Electromagnetic showers created near the gap deposit some energy in the gap, with subsequent changes of light response, resolution, and energy leakage into the hadron compartments.

After applying the corrections of Section 6.3, and accepting events having a light response within $\pm 3\sigma$ of the peak response, Fig. 35a shows the accepted event fraction (no correction has been made for the effect of the 2 mm beam size). The remaining events have a peak response and resolution shown in Fig. 35b and 35c.

The increase of longitudinal energy leakage near the cell interface, for all events, is shown in Fig. 31.

The separation between cells in the azimuthal direction is smaller than that just discussed : it amounts to 2 mm, with the space filled

by a pair of 0.5 mm steel plates. The effects on light response and longitudinal leakage are much smaller in this case.

6.7 - Light response for oblique incidence.

The data described so far concern normal incidence of the electron on a calorimeter cell. In the $\bar{p}p$ environment, however, tracks deviate from normal incidence by typically 5 to 10^{o} due to the finite length of the collision region.

Data were collected using 10 GeV electrons with angles of incidence simulating $\bar{p}p$ vertex offsets of ±20, ±50, ±100 and ±200 mm. The data were analysed as for the previous Sections, except that x was corrected for the incidence angle.

The corrected data of Fig. 36 show that the effect of intercell gaps on the measured light response decreases rapidly with increasing vertex offset ; for effective vertex positions of > ±20 mm, the change in light response is small. Similarly, the effect on the resolution of light response and on the variation in longitudinal leakage is negligible.

In the same way that the lateral energy escape was predicted, and compared with data (Section 6.5), the quantity q can be extended to take account of oblique track incidence. As a function of the fraction R of energy deposited in the highest energy cell we find

$$< q > \sim 0.205 - 0.2\ R, \qquad q_{90\%} \sim 0.412 - 0.4\ R.$$

7 - PERFORMANCE OF THE HADRON CALORIMETER

7.1 - Introduction.

In the energy domain of the $\bar{p}p$ Collider the hadron calorimeter serves essentially two purposes : to contribute to electron identification by discriminating against much more copious hadrons and to provide accurate measurements of the energy and direction of hadron jets [6].

The second of these tasks imposes severe constraints on the energy

response to single hadrons. Hadron jets consist of several collimated hadrons, mostly neutral and charged pions, with energies distributed approximately like E^{-1}. The UA2 detector cannot resolve individual jet fragments because this would require a segmentation of $\simeq$ 1 msr. As a result, individual impact points, energies, and identities (π^0, $\pi^{\pm}$, etc...) of each jet fragment are not separately measured. To achieve a good energy resolution it is therefore important that the response to single hadrons be as little dependent as possible on these parameters. In particular the linearity of the energy response should extend down to the GeV range and effects related to the crossing of cell boundaries must be kept as small as possible.

These considerations are also relevant to the sharpness of the threshold of a trigger on total transverse energy.

7.2 - Measurements with incident π^-'s.

The response of the hadron calorimeter to single pions was studied in a series of measurements performed with momentum analysed ($\Delta p/p \simeq 1\%$) π^- beams at the PS and SPS. Beam momenta of 1, 2, 4, 6, 10, 20, 40 and 70 GeV/c were used. Most measurements were performed with three modules arranged as a 45° azimuthal wedge of the actual calorimeter set-up. These modules were installed on a remotely controlled support which could be moved to let the beam impinge at any desired location of any cell of the middle module and to vary its angle of incidence within limits corresponding to the longitudinal extension of the $\bar{p}p$ collision region. The upper and lower modules were used to collect lateral shower escapes. In part of the high energy measurements an additional iron-scintillator calorimeter located behind the three modules was used to estimate longitudinal shower leakage.

The beam configuration and data collection electronics were the same as described in Section 5.2. The signal given by the scintillator behind the tungsten converter was required not to exceed 2 minimum ionising particle equivalent in order to veto against a small residual electron contamination.

7.3 - Relative contributions of the three compartments.

In general a hadron shower of energy E deposits energies E_i in each of the three calorimeter compartments. These individual energy depositions are in proportions which undergo large fluctuations. The signals S_i recorded in the associated phototubes are related to E_i via relations $E_i \simeq \lambda_i(E)\ S_i$, where the $\lambda_i(E)$ coefficients are averaged over different shower configurations and locations within the impact cell. An energy independent approximation to the λ_i coefficients, $\bar{\lambda}_i$, can be obtained from a measurement of the response to high energy muons (constant energy loss along their path) and, for i = 1, from the response to electrons. These approximations are however only indicative and the direct way to evaluate $\lambda_i(E)$ is to vary them until the width of the distribution $E = \sum_i \lambda_i(E) S_i$ is minimum. This procedure allows the definition of the $\lambda_i(E)$ coefficients up to a factor which is obtained by requiring that, on the average $< E >$ is equal to the incident beam energy. For example, in the energy range $1 < E < 10$ GeV, it yields the following result :

(I) $\lambda_1/\bar{\lambda}_1 = 1.27,\ \lambda_2/\bar{\lambda}_2 = 1.01,\ \lambda_3/\bar{\lambda}_3 = 0.93$

and, in the energy range $10 < E < 70$ GeV,

(II) $\lambda_1/\bar{\lambda}_1 = 1.18,\ \lambda_2/\bar{\lambda}_2 = 1.00,\ \lambda_3/\bar{\lambda}_3 = 1.06,$

with typical uncertainties of the order of 1%.

When dealing with hadron jets, since the detailed energy sharing among their fragments is unknown, one is forced to use energy-averaged values of the λ coefficients, with the result that their energy dependence implies a deterioration of the resolution achieved. Similarly, the exact π^0 content being unknown, the deviation from 1 of $\lambda_1(E)/\bar{\lambda}_1$ contributes an additional deterioration.

With these remarks in mind we adopt set (II) as a standard, energy independent, set of λ coefficients in the subsequent analysis and we always define the measured energy as

$$E_{meas} = 1.18\ \bar{\lambda}_1\ S_1 + \bar{\lambda}_2\ S_2 + 1.06\ \bar{\lambda}_3\ S_3,$$

where S_i is the geometric mean in compartment i of the signals associated with each of its two wave-shifting light guides.

7.4 - Energy dependence of the response to π^-'s.

The data collected with incident π^- beams of 1 to 70 GeV/c have been used to evaluate the ratio r between E_{meas} and E, for each event, as a function of energy, impact point, and angle of incidence. When performing this evaluation the data were corrected for a small lateral escape (always less than 2%) out of the 3-module test set-up - in the actual Collider experiment this escape is collected in the adjacent modules - but no correction was applied for longitudinal leakage beyond the second hadronic compartment.

No significant correlation between the dependences upon energy and impact point has been observed. In all cases a Gaussian distribution was found to give a fair description of the data (see Fig. 37), which allows for a summary of the results in terms of two parameters : the mean value of r, $\bar{r}$, and its root mean square deviation from $\bar{r}$, rms (r).

The dependences on energy of $\bar{r}$ and rms(r) are shown in Fig. 38a,b. The increase of $\bar{r}$ in the 1 to 10 GeV range reflects the fact that the adopted set of λ coefficients is not the most appropriate in this energy region. The effect of longitudinal leakage becomes significant at higher energies. The measured resolution (Fig. 38b) improves towards higher energies : $rms(r)/\bar{r}$ decreases from $\simeq$ 30% at 1 GeV to $\simeq$ 13% at 70 GeV. This decrease is slower than the naive $E^{-\frac{1}{2}}$ law which would result from purely statistical fluctuations and is closer to a $E^{-\frac{1}{4}}$ law. Better resolutions are obtained when the data are restricted to a single impact configuration : for example $rms(r)/\bar{r}$ is only 11% for 70 GeV π^-'s impinging normally on a cell centre. The values displayed in Fig. 38b include, in addition to the intrinsic instrumental resolution, that resulting from the adoption of a unique set of energy independent λ coefficients and from averaging over different configurations of impact point and incidence angle. They are however the relevant figures of merit when dealing with hadron jets.

7.5 - Impact dependence of the response to π^-'s.

The gross features of the dependence of $\bar{r}$ upon impact point are illustrated in Fig. 39 for normal incidence π^-'s. They include

i) a modulation of ≃ ±3% amplitude depending upon the relative distances of the impact point to the light guides of the impact cell,

ii) a modulation of ≃ ±5% amplitude depending upon the relative distances of the impact point to the steel walls separating the impact calorimeter module from its neighbours,

iii) a dependence upon cell type resulting in a ≃ 7% decrease when going from central to edge cells.

Correlations between these effects are measured to be small and are ignored : a good description (to within ≃ ±1%) of the dependence of $\bar{r}$ upon impact point is obtained with a parametrisation having the simple form $\bar{r} = r_0 + r_1 x^2 + r_2 \phi^2 + r_3 D^2$, where x and ϕ were defined in Fig. 22 and D is the distance of the impact point to the symmetry plane separating the two central cells of the calorimeter module (Fig. 39).

The dependence of the resolution upon impact is dominated by the relative distances of the impact point to the wave shifting light guides of the impact cell : it is optimum near cell centre and deteriorates near cell edges. The associated modulation of rms(r) has an energy dependent amplitude with $\Delta \{ \text{rms}(r) \} / \text{rms}(r)$ increasing from ≃ ±6% at 10 GeV to ≃ ±14% at 40 GeV.

Both $\bar{r}$ and rms(r) are observed to be very insensitive to the incidence angle within the limits corresponding to the event vertex distribution in $\bar{p}p$ collisions. In particular the effect on $\bar{r}$ does not exceed 1%.

Most of the features described above are of a global nature and result from various effects such as light attenuation in the scintillator plates, light collection efficiency, and shower absorption in the inter-module walls. They do not however account for local discontinuities at inter-cell boundaries. To study these effects, measurements were performed with fine scans accross such boundaries.

Particles travelling through the ≃ 8 mrad intercell gap where the light guides are inserted do not usually undergo nuclear interactions. But, while they give no signal in the light guides located at the other side of the cell, they produce Cerenkov light in the guides which they traverse : typically a relativistic π^- impinging in an intercell gap produces the same signal as a ∿ 4 GeV π^- impinging on the cell centre. The net result is an effective loss of acceptance which amounts to ≃ 5% for particles coming from the exact centre of the calorimeter. The effect

washes out rapidly for off-centre vertices. For particles impinging in the vicinity of the intercell gap the contribution of shower secondaries travelling through the gap is negligible : neither $\bar{r}$ nor rms(r) are significantly affected.

7.6 - Longitudinal shower development.

The π^- data are also useful to study the longitudinal and transverse developments of hadron showers in the calorimeter. For the longitudinal development studies we disregard hadrons which do not interact in the calorimeter : in any case, they cannot be distinguished simply from a small muon contamination in the incident beam ($\simeq$ 13% at 1 GeV, $\simeq$ 3% at 10 GeV). From the energy measurements in each compartment, $E_i = \lambda_i S_i$, we define two independent parameters describing the longitudinal development of the hadron shower :

$$X = E_1/(E_1 + E_2),$$
$$Y = E_3/(E_2 + E_3).$$

Longitudinally compact showers initiated near the front of the calorimeter feature large X and small Y values. Both X and Y span the range 0 to 1.

Distributions in X and Y as a function of incident energy are displayed in Fig. 40. While both parameters undergo large fluctuations, they exhibit a clear energy dependence which is consistent with the expected increase of the longitudinal shower extension with energy. The data have also been reduced to density tables in (X, Y) space at each energy, which can be used at the Collider to assign to each energy cluster a measure of the likelihood that it corresponds to a single charged hadron.

The behaviour of the X distribution in the vicinity of X = 1 is relevant to the evaluation of the rejection power against hadrons when searching for electrons. The probability for a 40 GeV π^- to deposit more than 90% of its energy in the electromagnetic compartment is 0.4%.

The increase of Y with energy is associated with an increased leakage beyond the second hadronic compartment. On the average we measure leakages of 2% at 20 GeV, 5% at 40 GeV and 7% at 60 GeV, which contribute to the curvature observed in the energy response curve towards higher energies (see Fig. 38). We have investigated the possibility to correct for this leakage on an event-by-event basis by using the measured value of Y and/or

the contribution of the last 3 scintillator plates as measured by the backtag phototube of the impact cell (see Section 2). We find that this procedure is not efficient at significantly improving the energy resolution. The reasons are that the leakage undergoes large fluctuations and does not contribute a dominant fraction of the global energy resolution. However the backtag signal can be used to eliminate leaking showers, for which its pulse height exceeds a threshold, thereby improving energy resolution at the expense of detection efficiency. For example, the resolution achieved with 40 GeV π^-'s is improved by 30% of its original value for showers having a backtag pulse height not exceeding that of a minimum ionising particle, but this selection retains only 60% of the original shower sample.

7.7 - Transverse shower development.

Transverse shower development in the calorimeter is studied from the dependence upon impact of the energy distribution among the cells involved. A convenient description of the transverse shower extension is provided by the fraction $1 - \rho(\alpha)$ of the shower energy deposited beyond a plane making an angle α with the trajectory of the incident hadron and containing the calorimeter centre (see Fig. 41). Measured values of $\rho(\alpha)$ are displayed in Fig. 41 for 10 GeV incident π^-'s. A fair description of the totality of the π^- data is obtained using a parametrisation of the form

$$\rho(\alpha) = \{ 1 + \exp(-\alpha/\bar{\alpha}) \}^{-1}$$

with

$$\bar{\alpha} = \alpha_0 + \alpha_1 \{ 1 - \exp-(\alpha/\alpha_2)^2 \} - \alpha_3 \ln(E/10\ \text{GeV}).$$

Note that $\rho(\alpha) + \rho(-\alpha) = 1$ as it should be. Best fit values are

$$\alpha_0 = (1.37 \pm 0.08)^0 \qquad \alpha_2 = (7 \pm 1)^0$$

$$\alpha_1 = (1.6 \pm 0.2)^0 \qquad \alpha_3 = (0.2 \pm 0.04)^0.$$

The data evidence a small but significant shrinking when energy increases : for $\alpha = 2^0$, $\bar{\alpha}$ decreases from $\sim 2.0^0$ at 1 GeV to $\sim 1.1^0$ at 70 GeV.

This parametrisation is useful at the Collider to evaluate the probability that the match between a track in the vertex detector and an energy cluster in the calorimeter is consistent with the hypothesis that they are both associated with the same charged hadron. For this purpose, as was done earlier in the case of electrons, we define a quantity q related to the difference between the observed and predicted energy

sharing among the cluster cells. The distribution of q for 10 GeV π^- data is shown in Fig. 42. Its dependence upon energy is weak and obeys the approximate relation $< q > \simeq 0.35\ E^{0.32}$ (E in GeV).

7.8 - Response to hadron jets.

The relevance in the Collider experiment of the calorimeter response to hadron jets was emphasized earlier. We now approach this question from two different points of view : one is to infer the response to hadron jets from the π^- data by using a simple model to simulate jet fragmentation ; the other is to analyse data collected at the SPS with a polyethylene target inserted on the incident beam path to produce multi-hadron jets impinging on the calorimeter.

The fragmentation model assumes, on the average, equal and uncorrelated π^0, π^+ and π^- populations. The longitudinal fragmentation function is chosen to be of the form $D(z) = \frac{(1-z)^2}{z}$ and the transverse momenta k_i of the fragments with respect to the jet axis have a distribution of the form $\frac{dN}{dk_i^2} \propto \exp(-\frac{\pi}{4} k_i^2/< k_i >^2)$ with $< k_i > = 450$ MeV/c.

The multihadron data are taken with incident π^- beams of 10, 20, 40 and 70 GeV/c. The target is a 10 cm thick polyethylene block ($\simeq 0.21$ radiation lengths, $\simeq 0.13$ absorption lengths) followed by a scintillator from which we require a pulse height exceeding 2 equivalent minimum ionising particles. It is located $\sim$ 40 cm away from the calorimeter front face.

The response to hadron jets depends critically on their relative content : the use of a unique, energy independent, set of λ coefficient result in an overestimate of the energy carried by π^0's (for which $\lambda_1 = 1$) and in an underestimate of that carried by soft $\pi^\pm$'s (for which $\lambda_1 = 1.27$ in the 1 to 10 GeV region). Also π^0's are measured with a better energy resolution (typically 14% $E^{-\frac{1}{2}}$) than $\pi^\pm$'s. The values obtained for $\bar{r}$ and rms(r) from the two independent approaches are displayed in Fig. 43 as a function of incident energy. These results indicate an improved resolution (despite the deterioration expected from the adoption of a unique set of λ coefficients) towards higher energies with respect to single hadrons. This is due in part to the lesser contribution of longitudinal escapes in the case of hadron jets. Distributions of X and Y

(Fig. 44) illustrate clearly their better containment.

Hadron jets are highly collimated and produce energy clusters extending over only a few calorimeter cells. In the Collider experiment the exact directions of the jet axes are unknown and are approximately obtained from the evaluation of the centre of energy of the calorimeter cluster. We find this approximation to be valid to within $\pm 3^{o}$ typically in the energy range 20 to 70 GeV. This result, together with the results of Fig. 43 on energy resolution, gives an estimate of the accuracy ΔM attached to the measurement of the invariant mass M of a typical two-jet system. We find $\Delta M \sim 8$ GeV/c^2 for M = 80 GeV/c^2.

8 - PATTERN RECOGNITION

Sections 6 and 7 discussed the calorimeter performance in a test beam environment. However, its performance at the $\bar{p}p$ Collider is complicated by event-by-event changes in the vertex position, and the fact that in a multiparticle environment clusters of energy deposition may overlap. In this Section we define the algorithm used to create clusters of energy deposition ; having created clusters, the previously discussed tools of

a) the distribution of longitudinal and lateral energy depositions,
b) the differing light response of individual tubes in a calorimeter cell,

can be used to distinguish between electrons, hadrons, and hadron jets.

Figures 45 and 46 show in θ-ϕ plots the electromagnetic and hadronic energy depositions in a typical 3-jet event [18] and, for the case of electrons, in a Z^{o} event [19]. Initially, all neighbour cells having a common edge and an energy $E_{cell} > E_{th}$ are associated to form a cluster. The cell energy of a single compartment, or a combination of compartments, may be considered. If, within a cluster, more than one energy maximum exists (separated by $\delta E > \delta E_{val}$) the cluster is separated, individual cells being associated to one or the other cluster. The created clusters are superimposed on Figs. 45 and 46.

The associated cluster energy is defined from the individual cell energies E_i , and a halo energy from neighbouring cells having energy $E_{cell} < E_{th}$, therefore not participating in the cluster, is added.

The resultant clusters of energy have :

a) a cluster energy $E_{cluster} = \sum_i E_i + E_{halo}$,

b) a direction and position defined by the event vertex, and the (energy-weighted) average cluster position defined below,

c) a cluster size in each of the θ and ϕ directions,

$$\sigma_\theta = \left[< \theta^2 > - < \theta >^2 \right]^{\frac{1}{2}}$$

$$\sigma_\phi = \left[< \phi^2 > - < \phi >^2 \right]^{\frac{1}{2}}$$

with $< K > = \Sigma_i K_i E_i / \Sigma_i E_i$, $\quad K_i = \theta_i$ or ϕ_i.

Typically, an electron or photon cluster in the electromagnetic compartment will extend over one or two calorimeter cells ; a hadron typically deposits significant energy in a cluster of 3 × 3 cells but with small σ_θ and σ_ϕ (that is, most of the energy is deposited in one or two cells). However, a hadron jet will typically result in a cluster of about 10 cells. In addition to the high-energy clusters reconstructed in a 2-jet event, typically 3 clusters of energy E > 1.0 GeV are reconstructed [18].

The values of E_{th} and E_{val} used depend on the type of physics analysis performed. For electron and photon identification, clusters are evaluated in each compartment, and subsequently linked according to their distance from a line defined by the reconstructed vertex and the electromagnetic cluster. In these studies, E_{th} = 0.5 GeV and δE_{val} = 1.0 GeV. For the creation of clusters used in jet analyses, the energy of each compartment is added before creating clusters ; in this case, E_{th} = 0.4 GeV and δE_{val} = 5.0 GeV. Because the energy of surrounding cells is added as a halo to the cluster energy, results are relatively insensitive to the value of E_{th} chosen.

ACKNOWLEDGMENTS

We deeply thank P. Bagnaia and J. Bürger for their important contributions to the analysis of the calibration data and we gratefully acknowledge H.M. Steiner and A.R. Weidberg for their help in calibration runs. We thank H.H. Williams for stimulating discussions on calibration problems.

We are indebted to H. Grote for his contribution to the data analysis and to J.A. Bogaerts, Ch. Eck and J.O. Petersen for their contributions to the on-line data acquisition system.

We would like to thank the R807 Collaboration and in particular W. Witzeling for helpful discussions and the loan of test apparatus.

We thank G. Muratori and his group for the design and construction of the motorised table used in the calibration runs.

We are grateful to R. Guerin and G. Reiss and to G. di Bisceglie, M. Blanc, L. Cheneval, R. Cipriani, P. Condevaux, P. Gourdin, W. Higonnet, J. Loulergue, J-P. Recour and J-L. Spiller for their contribution to the construction and assembly of the calorimeter. Finally, we deeply acknowledge M. Prost for her skillful work in assembling the scintillator plates for the calorimeter and for her help in editing this report.

TABLE 1

Photomultiplier characteristics

Photomultiplier	XP2008	XP2012
used in calorimeter type	hadronic	electro-magnetic
Dark current (gain 5×10^5, $20^{\circ}C$)	< 50 nA	
Photocathode efficiency (integrated over BBQ emission spectrum)	> 10% (plus > 60% of the mean efficiency of all PM)	
Linearity deviations ($<I_a>$ = 1 μA, gain 5×10^5, range 0 - 100 mA)	< 2%	
Stability (maximum variation of gain during 12 hours, $<I_a>$ 5 μA)	< 2%	
Rate stability (maximum variation of gain when $<I_a>$ changes from 0.5 μA to 5 μA)	< 6%	

REFERENCES

[1] C. Rubbia, P. Mc Intyre and D. Cline, Proc. Int. Neutrino Conference, Aachen, 1976 (Vieweg, Braunschweig, 1977), p. 683.
S. Van der Meer, CERN/SPS/423(1978) and CERN/PS/AA 78-3 (1978).

[2] The Staff of the CERN proton-antiproton project, Phys. Lett. 107B (1981) 306.

[3] S.L. Glashow, Nucl. Phys. 22 (1961) 579.
S. Weinberg, Phys. Rev. Lett. 19 (1967) 1264.
A. Salam, Proc. 8th Nobel Symposium, Aspenäsgården, 1968 (Almqvist and Wiksell, Stockholm), p. 367.

[4] L.B. Okun' and M.B. Voloshin, Nucl. Phys. B120 (1977) 459.
C. Quigg, Rev. Mod. Phys. 94 (1977) 297.
J. Kogut and J. Shigemitsu, Nucl. Phys. B129 (1977) 461.
R.F. Peierls, T. Trueman and L.L. Wang, Phys. Rev. D16 (1977) 1397.
F.E. Paige, BNL - 27066 (1979).
F. Rapuano, Lett. Nuovo Cim. 26 (1979) 219.
R. Horgan and M. Jacob, CERN 81-04, p. 65 (1981).

[5] M. Calvetti et al., The UA1 Central detector, CERN-EP/82-44, presented at the Int. Conf. on Instrumentation for Colliding Beam Physics, SLAC, 17-23 February 1982.

[6] M. Banner et al., Phys. Lett. 118B (1982) 203. See also Ref. 18.

[7] M. Banner et al., Phys. Lett. 122B (1983) 476. See also Ref. 19.

[8] The UA2 Collaboration, Status and First Results from the UA2 Experiment, Proceedings of the 2nd Intern. Conf. on Physics in Collisions (Stockholm, 2-4 June 1982), Plenum Press, New York (1983), p. 67.
The UA2 Collaboration, The UA2 Apparatus at the CERN $\bar{p}p$ Collider, presented by B. Mansoulié at the 28th Rencontre de Moriond, La Plagne, March 19-25 1983, to be published.

A.G. Clark, Proc. Int. Conf. on Instrumentation for Colliding Beam Physics, SLAC-250, 1982.

[9] R. Battiston et al., Phys. Lett. 117B (1982) 126.

[10] K. Alpgård et al., Phys. Lett. 107B (1981) 310.

[11] C.W. Fabjan and W. J. Willis, Proc. Calorimeter Workshop, Batavia, Ill. (1975), p. 1.

[12] C.W. Fabjan and T. Ludlam, Ann. Rev. Nucl. Part. Sci. 32 (1982) 335 and references therein.

[13] W.J. Willis and J. Radeka, Nucl. Instrum. Methods 120 (1974) 221.

[14] R.L. Garwin, Rev. Sci. Instrum. 31 (1960) 1010.
W.B. Atwood et al., SLAC-TM-76-7 (1976).

[15] V. Hungerbühler, CERN yellow report 81-07 (1981) p. 46.

[16] G. Schuler, CERN yellow report 82-09 (1982).

[17] A. Beer et al., NIM 160 (1979) 217.
F. Bourgeois, Modular Trigger Logic Techniques at the CERN Omega Spectrometer, Nuclear Science Symposium, San Fransisco, U.S.A. 17-19 October 1979.
T. Armstrong et al., NIM 175 (1980) 543.
A. Corre et al., NIM 179 (1981) 585.

[18] P. Bagnaia et al., Z. Phys. C 20 (1983) 117.

[19] P. Bagnaia et al., Phys. Lett. 129B (1983) 130.

FIGURE CAPTIONS.

1. The UA2 detector : schematic cross section in the vertical plane containing the beam.

2. The central calorimeter of the UA2 detector on its support platform in the underground assembly hall of the CERN $\bar{p}p$ Collider.

3. A photograph of the electromagnetic cell front faces during assembly (thirteen out of twenty four modules are in position).

4. A schematic comparison between spherical (left hand side) and cylindrical (right hand side) geometries.

5. Basic steel structure of a hadron calorimeter module during assembly. The converter plates of 5 out of 10 cells are assembled. The lower lid is in position but the upper lid is not yet installed. The light guide housing structures and the phototube support plates are visible in the back.

6. Perspective view of a calorimeter cell showing schematically the mode of light collection.

7. Close-up photograph of the electromagnetic cells of a calorimeter module. The wave-shifting light guides are not yet in position. Calibration light fibers are prepared for connection to the scintillator plates.

8. Photograph of a calorimeter module during assembly showing the light guides and the phototube support plates.

9. Spectral responses of various light-collection equipments
   a) emission spectrum of the scintillator plates used in the electromagnetic calorimeter,
   b) emission spectrum of the scintillator plates used in the hadronic calorimeter,

c) absorption spectrum of the wave-shifting light guides,
d) emission spectrum of the wave-shifting light guides,
e) transmission coefficient of the light guides bringing the wave-shifted light to the phototubes,
f,g) photocathode responses of the phototubes used to collect the light from the electromagnetic (f) and hadronic (g) compartments.

10. Examples of photomultiplier test results
a) a typical good test result,
b) an unsatisfactory test result showing failure of the stability tests and two discrete gain changes.

11. a) Schematical layout of the calibration system (see text). Only one calorimeter cell is shown.
b) Sketch of the implementation of the calibration system.

12. The electronics associated to a single electromagnetic cell.

13. Simplified block diagram of a ROLAND module.

14. Timing diagram of the W and Z triggers.

15. a) Average drift per module measured for the electromagnetic calorimeters. The first four modules have been operated previously in the UA2 detector (see text).
b) Distribution of R_{em}, defined as the observed ratio of the response to electrons in the last recalibration to that in the initial calibration, for all channels contributing to (a).

16. Average drift per module measured for the hadronic calorimeter. The values for the two compartments are shown separately.

17. Transverse energy E_T in the first hadronic compartments, summed over all non-edge cells of a given module, from non-biased $\bar{p}p$ collisions.

18. Ratios of the energy correction factors $f_{corr} = 1 + \delta$ obtained by the energy flow method for two different data samples (see text).

19. Results of the correction procedure for the electromagnetic calorimeter. Module 5 has been excluded (see text).
    a) Average values of R_{em}^{corr} per module, defined as the ratio of the corrected response to electrons in the last recalibration to that in the initial calibration.
    b) Distribution of R_{em}^{corr} for all channels.

20. Results of the correction procedure for the hadronic calorimeter. Average values of R_{had}^{corr} per module, defined as the ratio of the corrected response to muons (hadrons) in the last recalibration to that in the initial calibration. The results for the two compartments are shown separately.

21. An example of the energy deposition for non-interacting particles in the electromagnetic calorimeter (edge cells excluded). Data collected from $\bar{p}p$ interactions.

22. A typical cell (type 3) of the electromagnetic calorimeter. The position (x mm, ϕ degree) is defined with respect to the cell centre unless otherwise stated. BBQ_s, BBQ_ℓ represent the response of respectively the small and large BBQ-doped light guides. $BBQ_{s\ell} = \sqrt{BBQ_s \; BBQ_\ell}$

23. Deviation of the light response $BBQ_{s\ell}$ from linearity, as a function of the incident electron energy E_b (GeV). The superimposed curve is $\propto (1.0 + 0.01 \ln [E_b + 1.0])$.

24. The energy resolution as a function of the incident electron energy. The open points show data where the tungsten converter is positioned as for collider operation. Full points show data collected with the tungsten converter 90 cm from the front of the calorimeter.

25. Response(before correction for attenuation) of 10 GeV/c electrons normally incident on cell type 3 (intermediate cell size). Data are

shown for a) BBQ_s b) BBQ_ℓ c) $BBQ_{s\ell}$. The data are normalised to 1.0 at the centre of the cell (see Fig. 22) ; the vertical bars in each figure represent the cell edge.

26. The same data as that of Fig. 25, corrected for light collection variations. Data are shown for a) BBQ_s b) BBQ_ℓ c) $BBQ_{s\ell}$.

27. The resolution (rms in mm) of the evaluated track impact, as a function of the position in each of cell types 1 to 5, for electrons of 10 GeV/c and 40 GeV/c normally incident in the median plane of the cells ($\phi = 0^o$). The variable z is measured along the calorimeter front face with respect to the edge of cell type 1, in mm.

28. The value of the quantity $\sigma/\sqrt{E}$, where σ is the energy resolution, as a function of the position in cell types 1 to 5, for electrons of 10 GeV/c and 40 GeV/c, in the median plane ($\phi = 0^o$). The variable z is measured with respect to the edge of cell type 1. Shower leakage into the hadron calorimeter has not been included in the evaluation of the energy.

29. The distribution of longitudinal energy leakage into the hadron calorimeter, for 10 GeV electrons of normal incidence at the centre of cell type 3.

30. The fraction of events which (at a given incident electron energy) deposit less than a fraction α of the electron shower energy in the hadron calorimeter.

31. The mean longitudinal leakage, normalised to the centre-cell leakage, as a function of position in the calorimeter cell, for normal-incidence electrons in the median plane ($\phi = 0^o$).

32. The fractional lateral energy containment in a calorimeter cell, as a function of the track impact position in the cell. The variable ξ (mm) is defined with respect to the edge of the cell. The superimposed parametrisation is defined in the text.

33. Typical distribution of the quality factor q, defined in the text, for 10 GeV normal incidence electrons with impact point 12 mm from the cell edge.

34. 90% and 95% containment limits, for the quality factor q. Data are shown for 10 GeV normal incidence electrons in the median plane ($\phi = 0^{o}$).

35. a) Fraction of events with measured energy within $\pm 3\sigma$ of the peak energy as a function of the distance of track impact from the cell edge (10 GeV electrons in the median plane).
    b) Light response $BBQ_{s\ell}$ for accepted events.
    c) Resolution of response $BBQ_{s\ell}$ for accepted events.

36. Light response as a function of track impact position, for electrons having an incident angle equivalent to ±20, ±50, ±100 and ±200 mm vertex offsets Δv at the $\bar{p}p$ Collider. Open circles correspond to positive values of Δv, full circles to negative ones.

37. A typical r-distribution. The curve is the best Gaussian fit through the data.

38. The dependence on incident energy of $(\bar{r} - 1)$ and of $rms(r)/\bar{r}$ (see text). The curves are simple fits
$\bar{r} - 1 = A_0 + A_1 \ell n\ E + A_2 \ell n^2 E$ and $rms(r)/\bar{r} \propto E^{-\frac{1}{4}}$.

39. The dependence of $\bar{r}$ upon the coordinates of the impact point on the calorimeter front face. The data are for 10 GeV π^- at $\phi \simeq 0^{o}$ (black circles) and $\phi \simeq 6^{o}$ (open circles). Error bars are not shown (their sizes are illustrated by the point to point fluctuations).

40. Longitudinal shower development. X and Y distributions (see text) are shown for different π^- energies.

41. Fraction of the shower energy contained within the space limited by a plane making an angle α with the trajectory of the incident hadron (see text).

42. A typical q-distribution obtained for 10 GeV incident π^-s (see text).

43. The dependence of $\bar{r}$ and rms(r) on energy for multihadron data (black circles) and for Monte Carlo jets (crosses). The smooth line indicates the behaviour of single pions.

44. The X and Y distributions obtained for 40 GeV Monte Carlo jets (black circles). Error bars include the effects of reasonable changes in the fragmentation parameters. The dotted line corresponds to a change of the $\frac{\pi^0}{\pi^-}$ ratio from $\frac{1}{3}$ to $\frac{1}{2}$ and the dashed line from $\frac{1}{3}$ to $\frac{1}{5}$. The smooth line is for 40 GeV single pions.

45. Energy deposition in each cell (θ-ϕ view) of the central calorimeter for a 3-jet event. In each cell, the lower number represents the electromagnetic energy and the upper number shows the hadronic energy deposition. Also shown (darkened) are jet-clusters formed for this event. A threshold energy E_{th} = 0.4 GeV is used for cluster creation.

46. As Fig. 45 , for a typical $Z^o \rightarrow e^+e^-$ event. Electromagnetic clusters are shown as darkened outlines. Also shown in this figure are the positions of reconstructed track impacts on the calorimeter (•), indicative of good track-energy matching. A threshold energy E_{th} = 0.5 GeV is used for cluster creation.

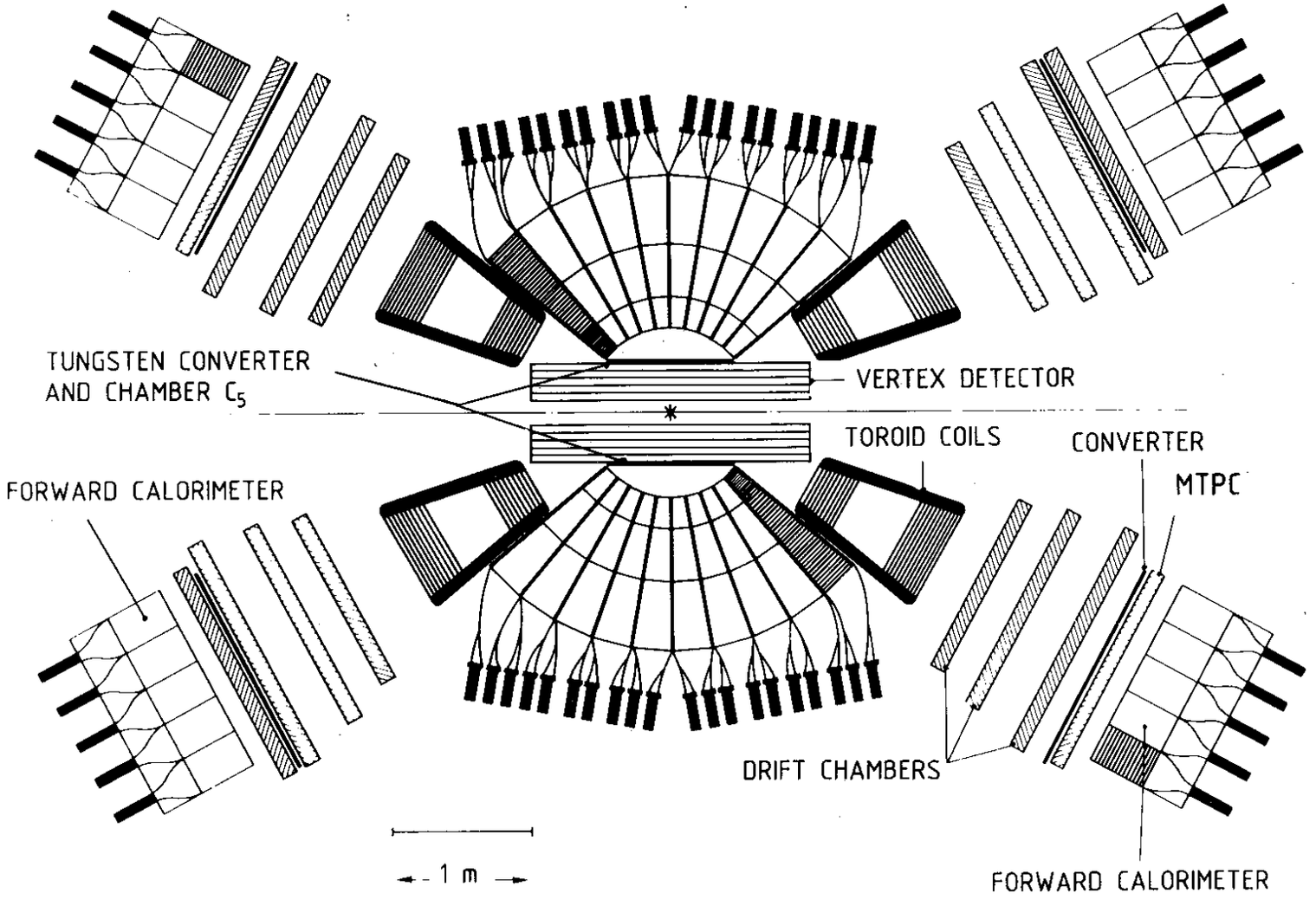
TUNGSTEN CONVERTER
AND CHAMBER C_5
VERTEX DETECTOR
TOROID COILS
CONVERTER
MTPC
FORWARD CALORIMETER
DRIFT CHAMBERS
1 m
FORWARD CALORIMETER

Fig. 1

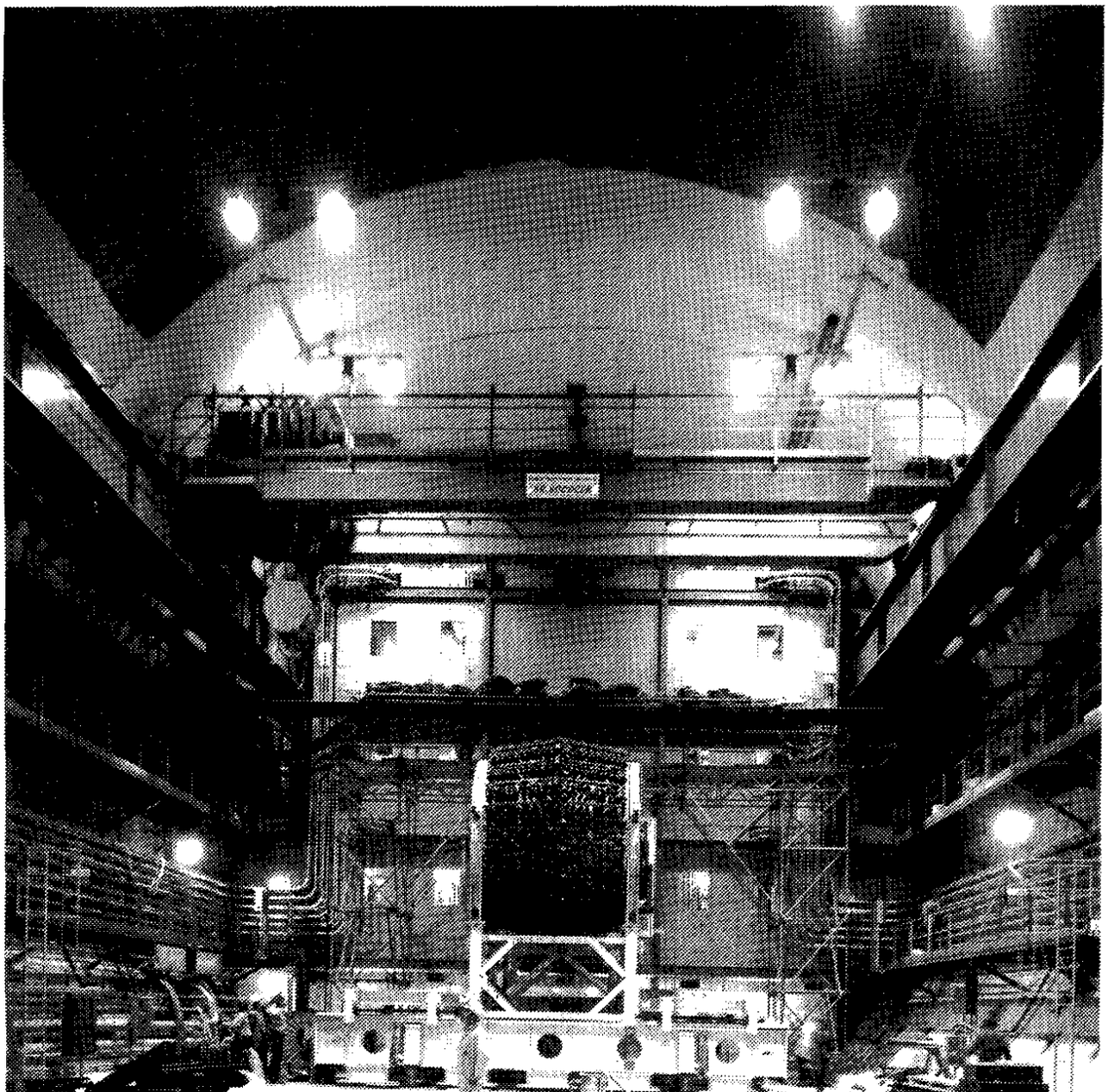

Fig. 2

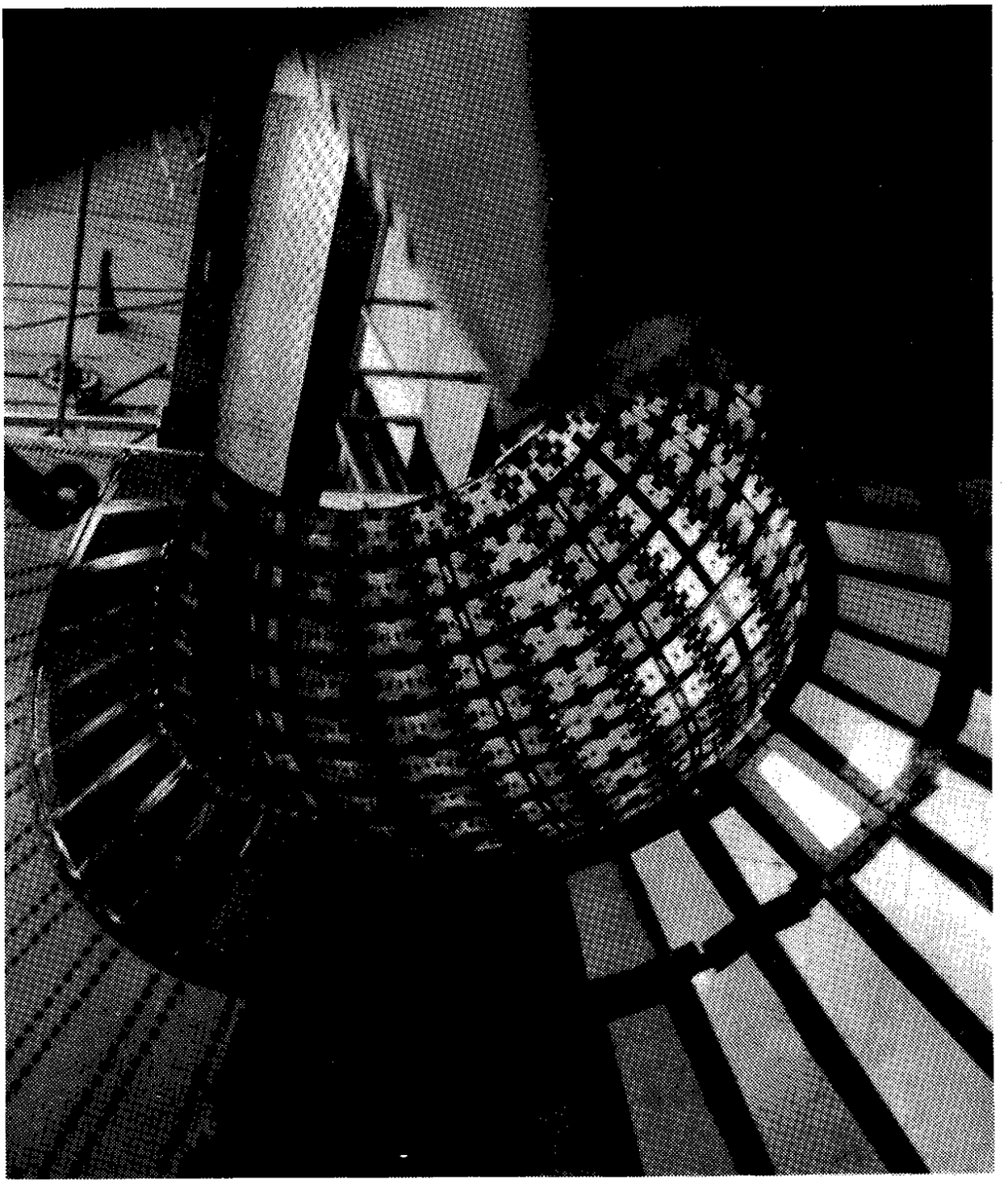

Fig. 3

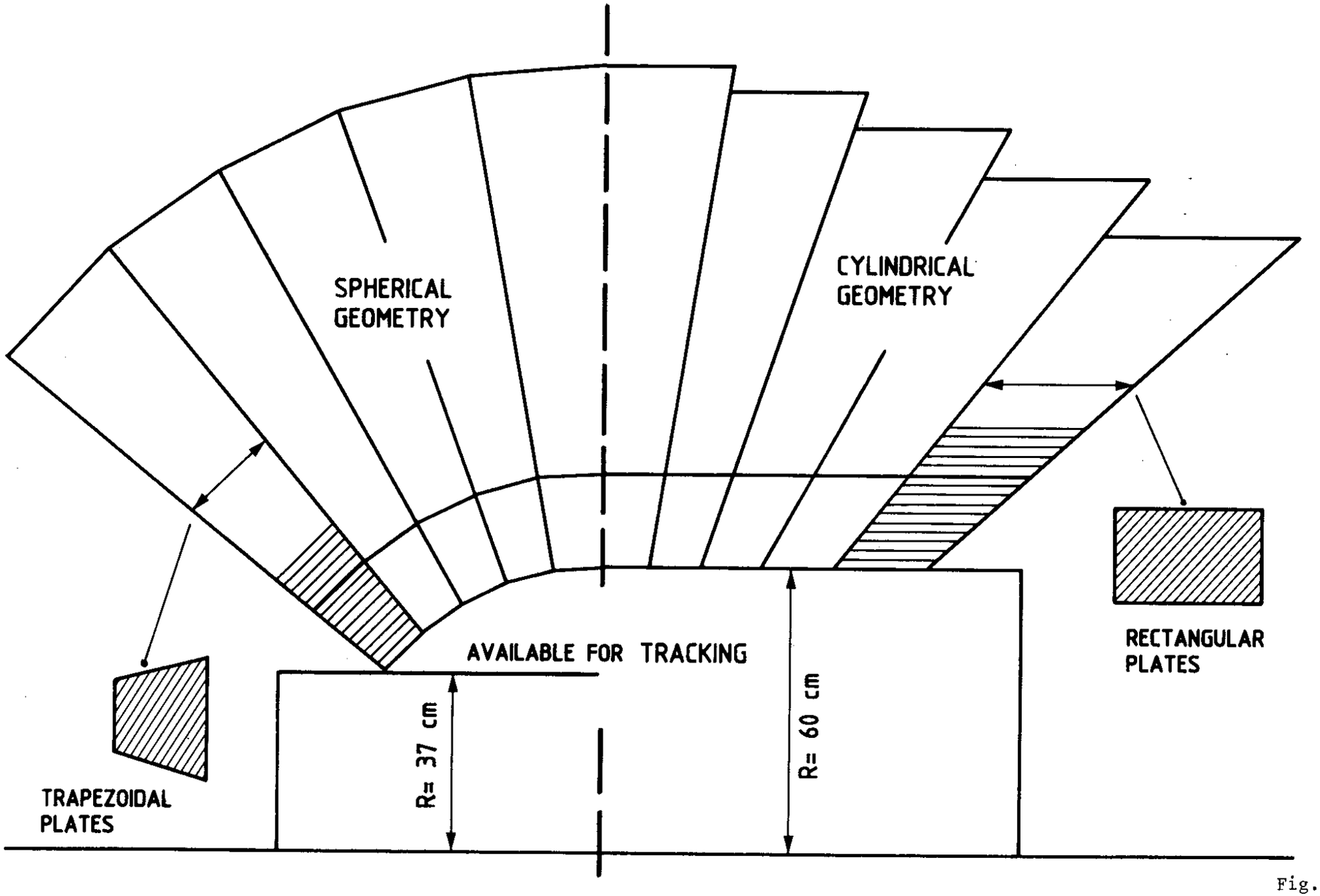
SPHERICAL
GEOMETRY
CYLINDRICAL
GEOMETRY
AVAILABLE FOR TRACKING
R= 37 cm
R= 60 cm
TRAPEZOIDAL
PLATES
RECTANGULAR
PLATES

Fig. 4

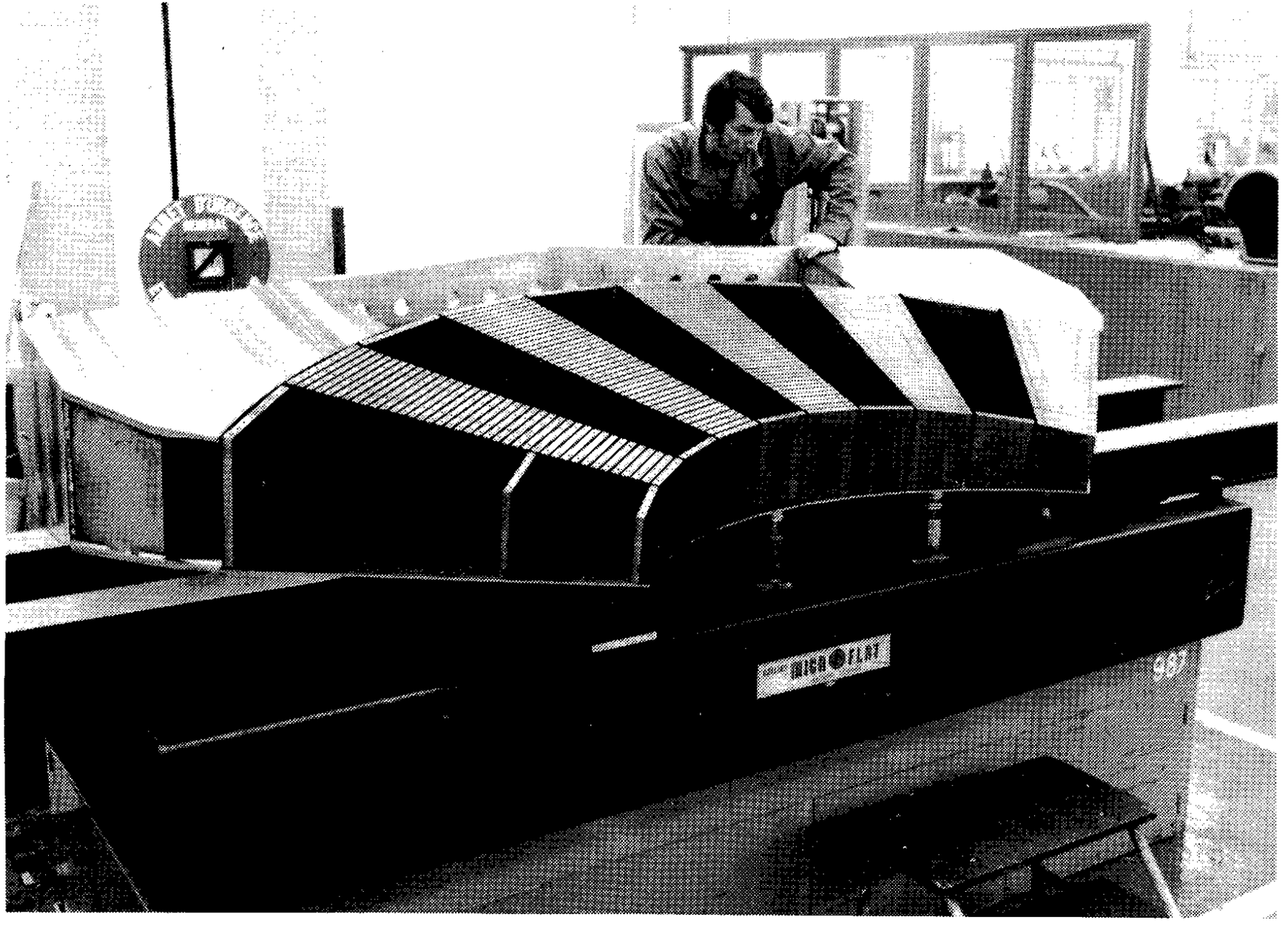

Fig. 5

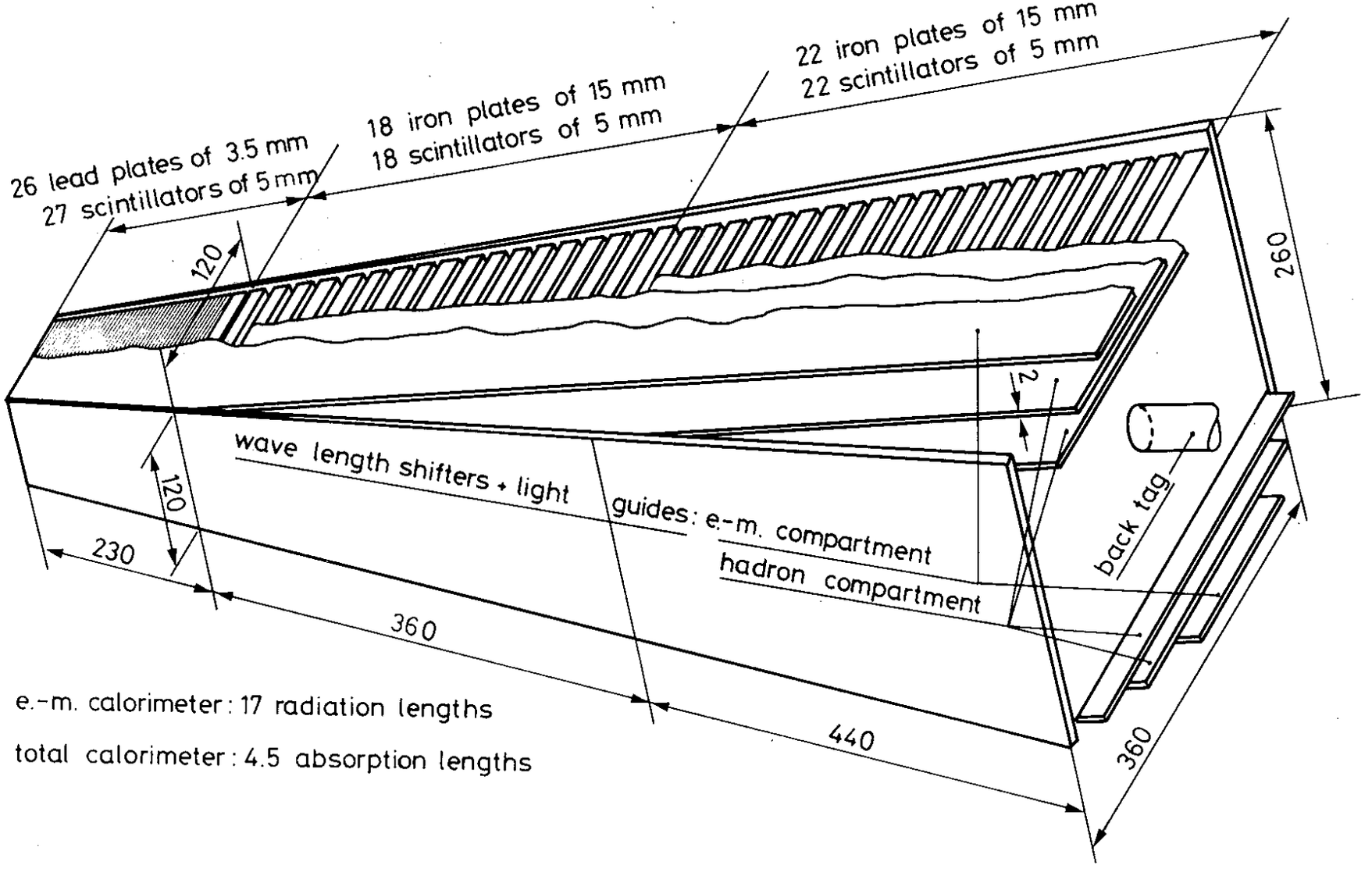
26 lead plates of 3.5 mm
27 scintillators of 5 mm
18 iron plates of 15 mm
18 scintillators of 5 mm
22 iron plates of 15 mm
22 scintillators of 5 mm
120
260
2
120
wave length shifters + light guides: e.-m. compartment
hadron compartment
back tag
230
360
440
360
e.-m. calorimeter: 17 radiation lengths
total calorimeter: 4.5 absorption lengths

Fig. 6

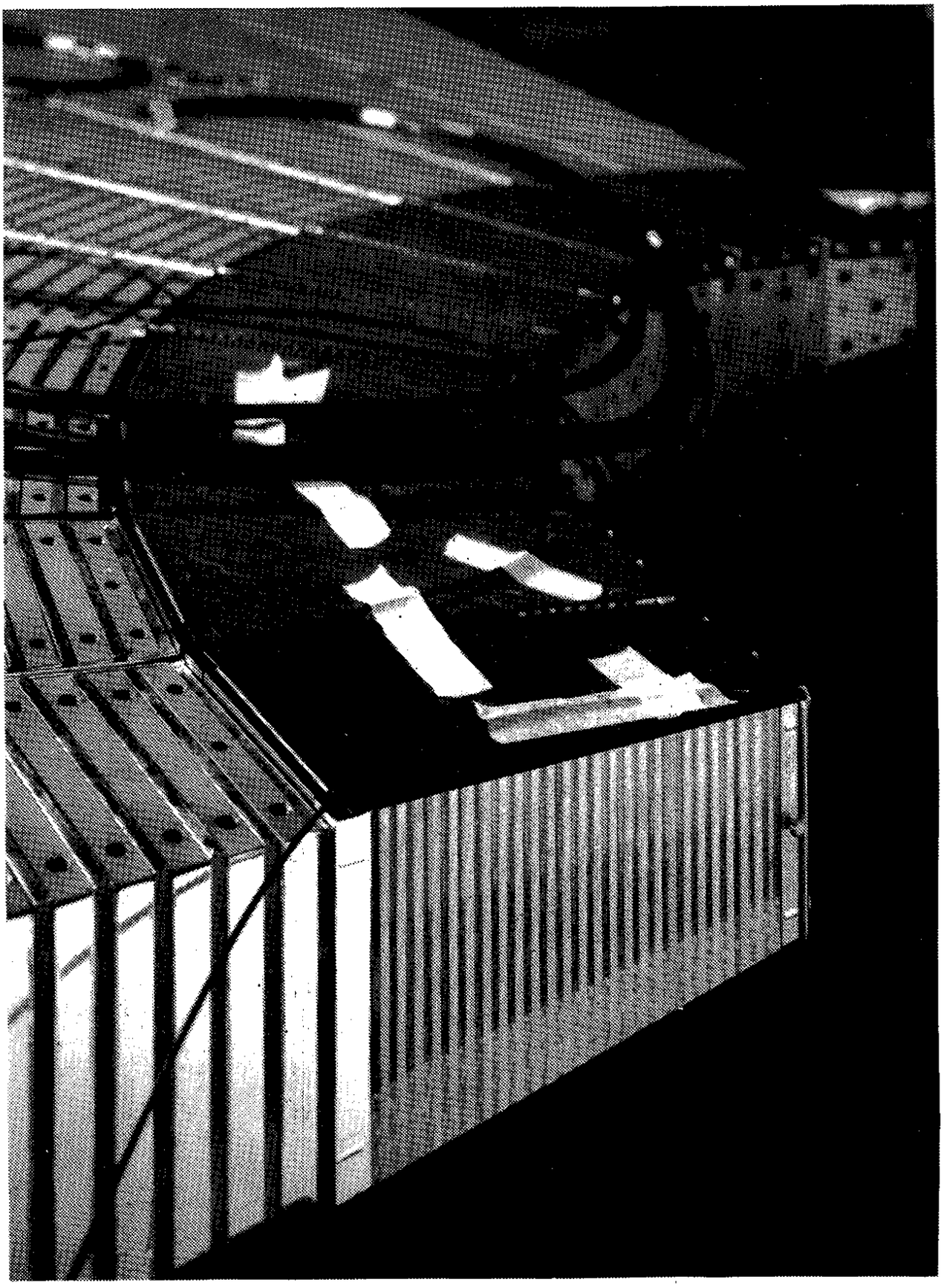

Fig. 7

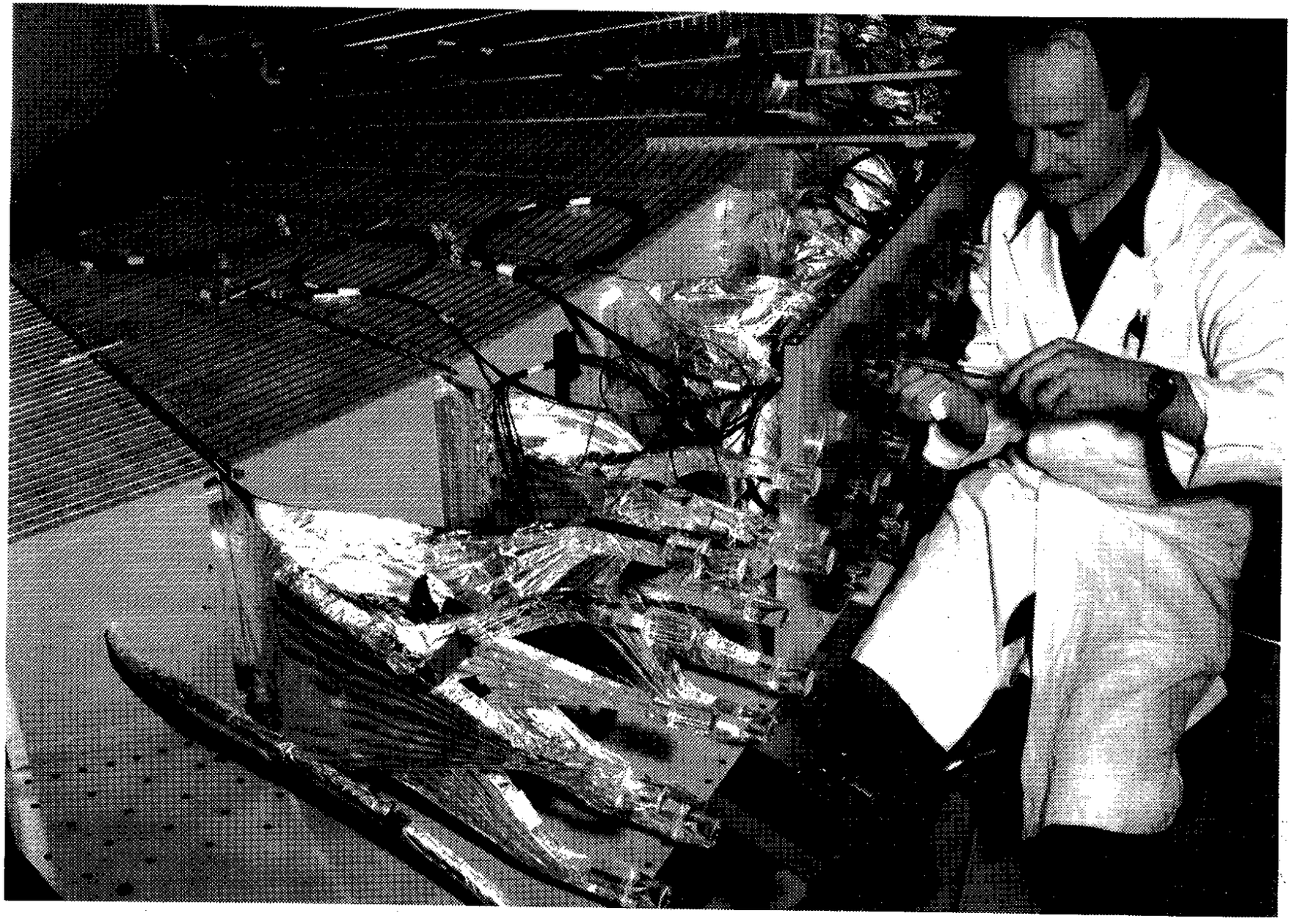

Fig. 8

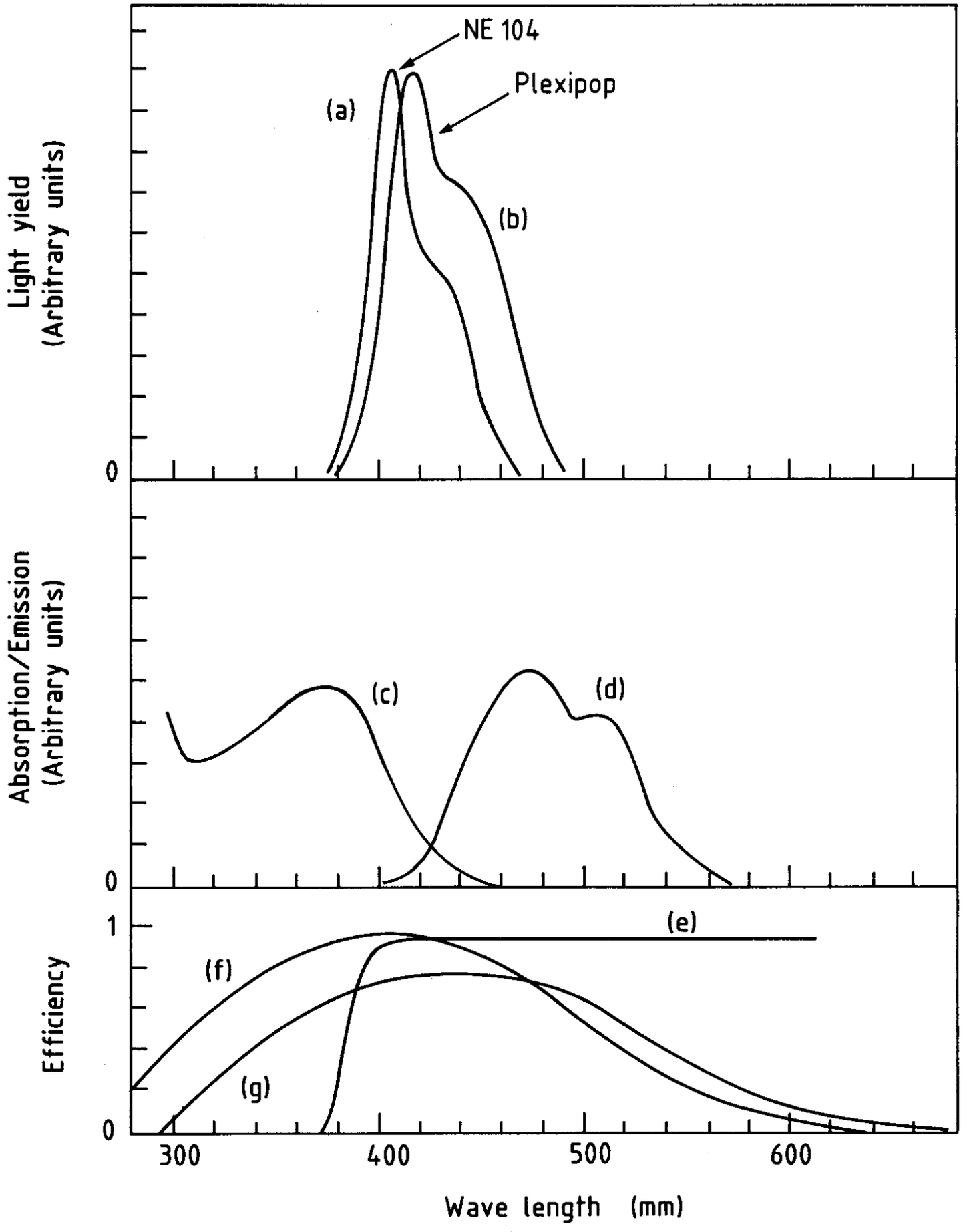
NE 104
Plexipop
(a)
(b)
Light yield
(Arbitrary units)
0
(c)
(d)
Absorption/Emission
(Arbitrary units)
0
1
(e)
(f)
(g)
Efficiency
0
300
400
500
600
Wave length (mm)

Fig. 9

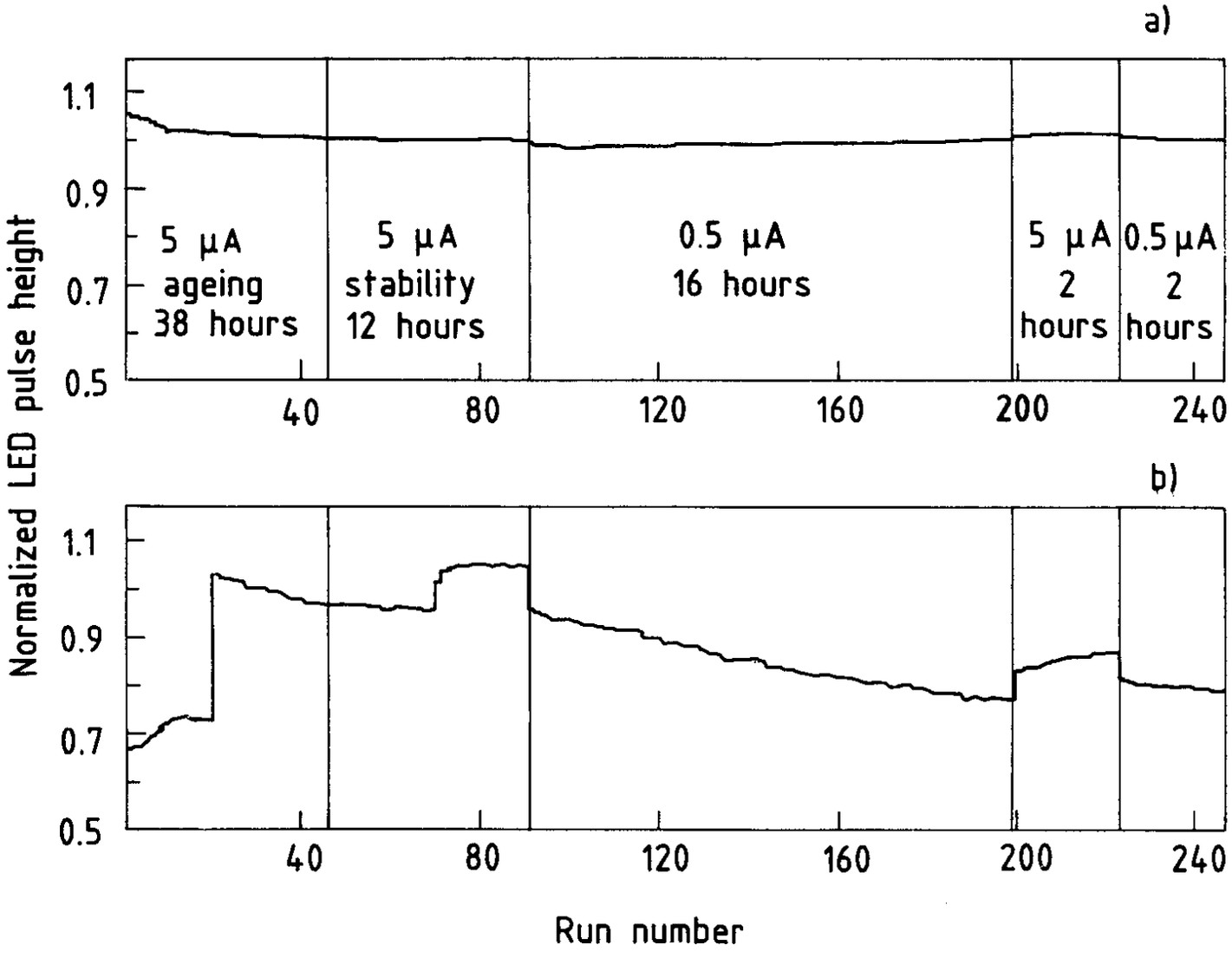
a)
b)
1.1
0.9
0.7
0.5
5 µA
ageing
38 hours
5 µA
stability
12 hours
0.5 µA
16 hours
5 µA
2
hours
0.5 µA
2
hours
40
80
120
160
200
240
Normalized LED pulse height
Run number

Fig. 10

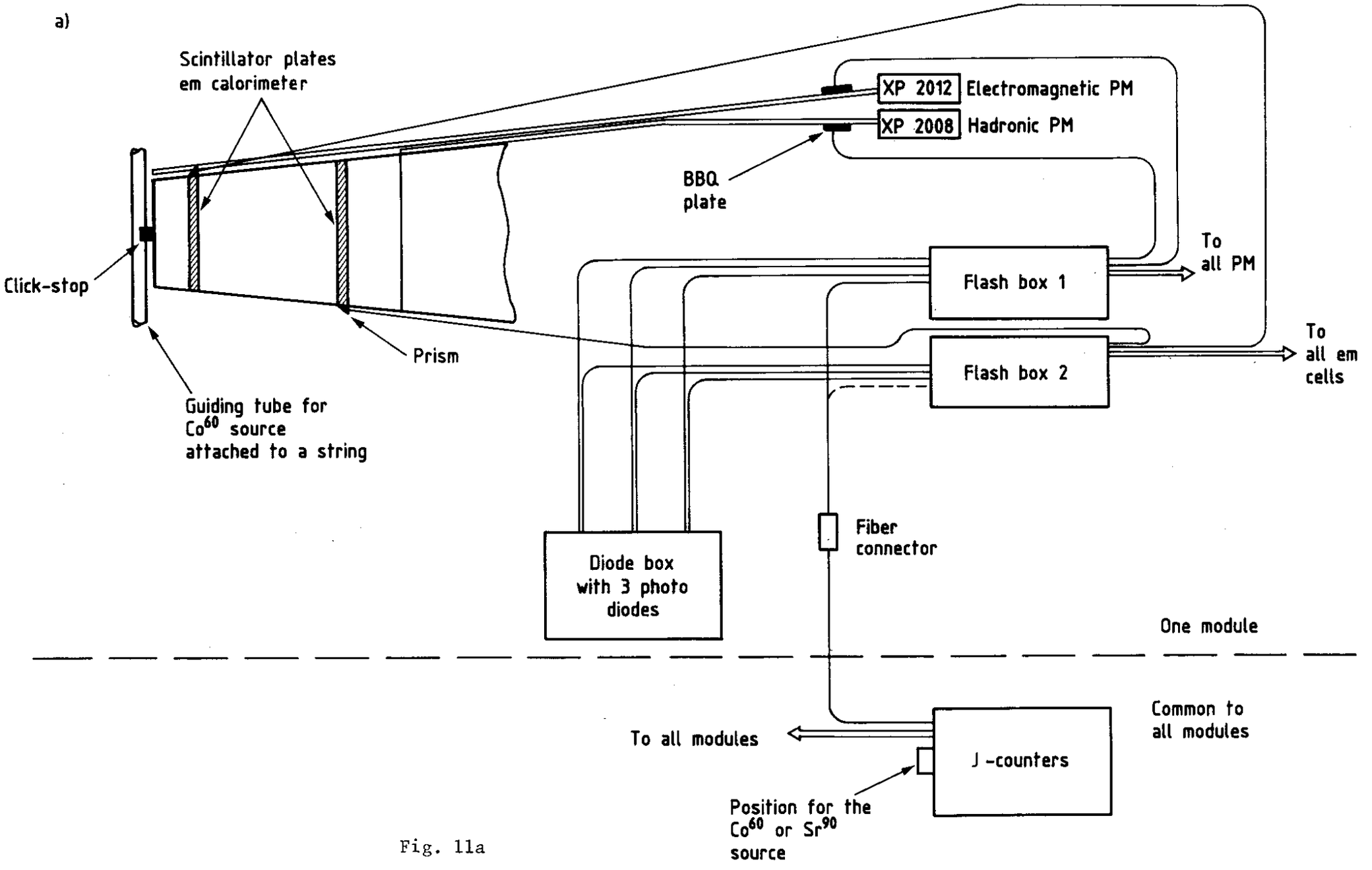
a)
Scintillator plates
em calorimeter
XP 2012 Electromagnetic PM
XP 2008 Hadronic PM
BBQ
plate
Click-stop
Prism
Guiding tube for
Co60 source
attached to a string
Flash box 1
To
all PM
Flash box 2
To
all em
cells
Diode box
with 3 photo
diodes
Fiber
connector
One module
To all modules
J -counters
Common to
all modules
Position for the
Co60 or Sr90
source

Fig. 11a

b)

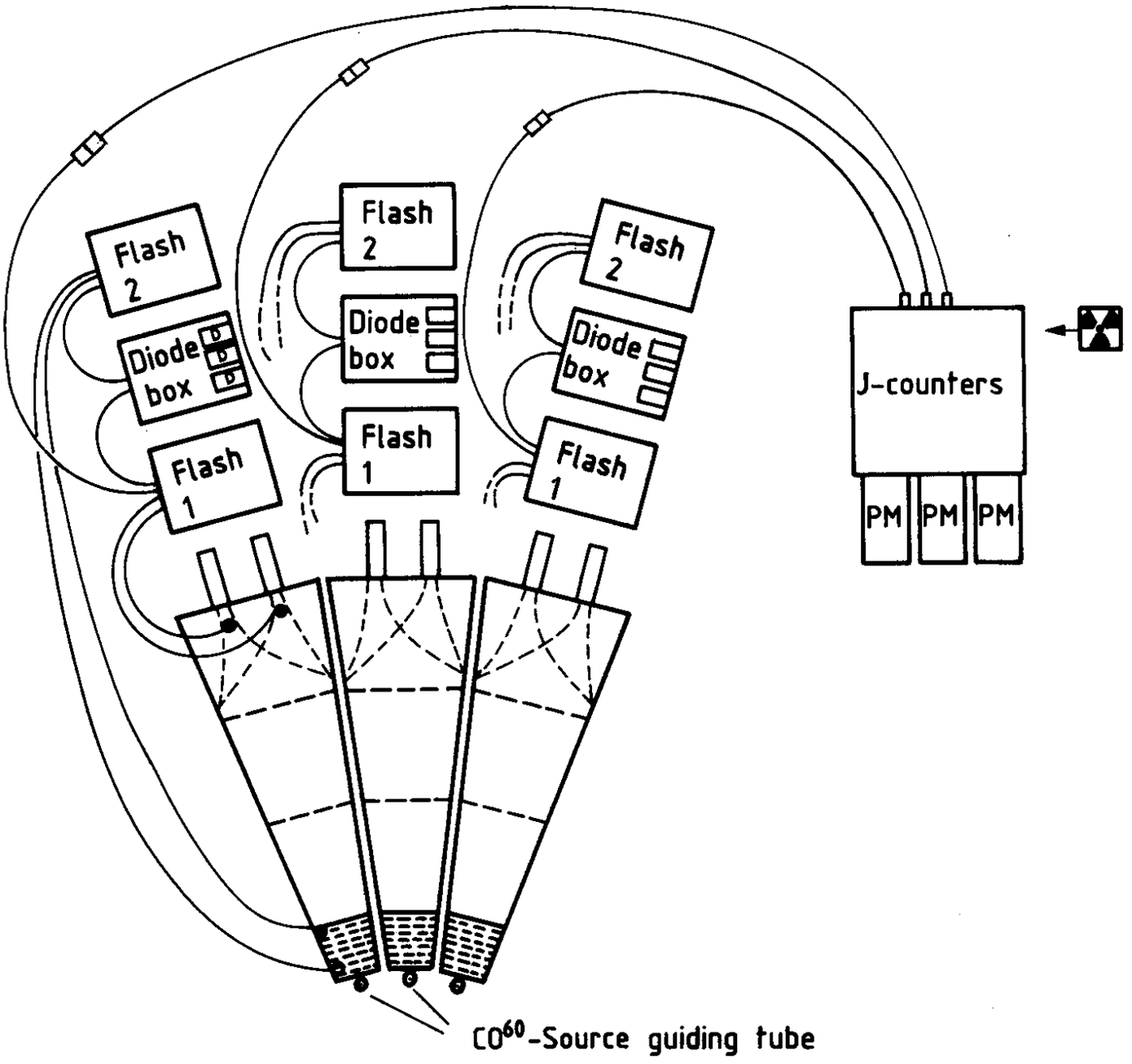
Flash 2
Diode box
Flash 1
Flash 2
Diode box
Flash 1
Flash 2
Diode box
Flash 1
J-counters
PM
PM
PM
CO^{60}-Source guiding tube

Fig. 11b

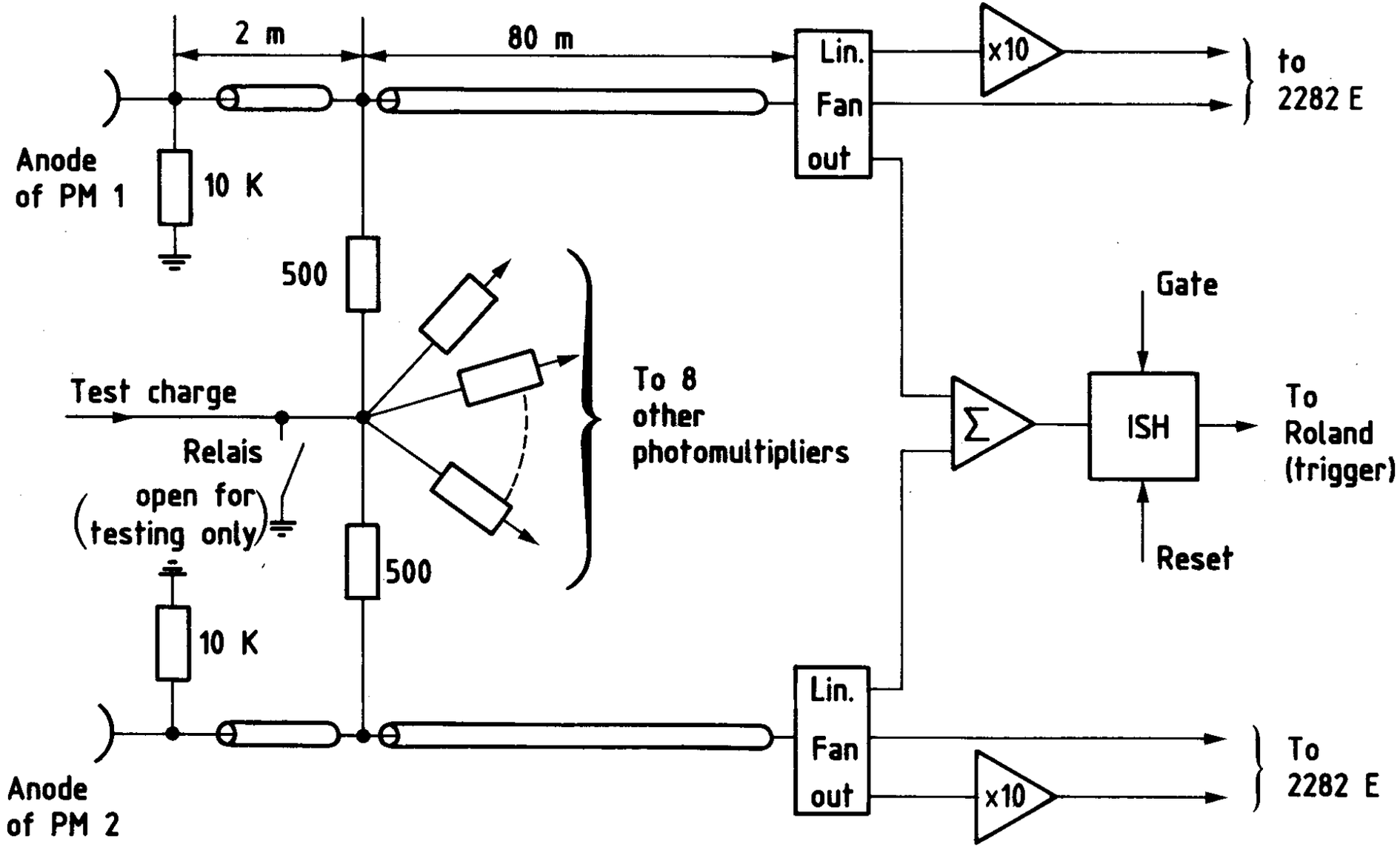
2 m
80 m
Lin.
Fan
out
x10
to
2282 E
Anode
of PM 1
10 K
500
Test charge
Relais
open for
testing only
500
To 8
other
photomultipliers
Gate
Σ
ISH
To
Roland
(trigger)
Reset
10 K
Lin.
Fan
out
x10
To
2282 E
Anode
of PM 2

Fig. 12

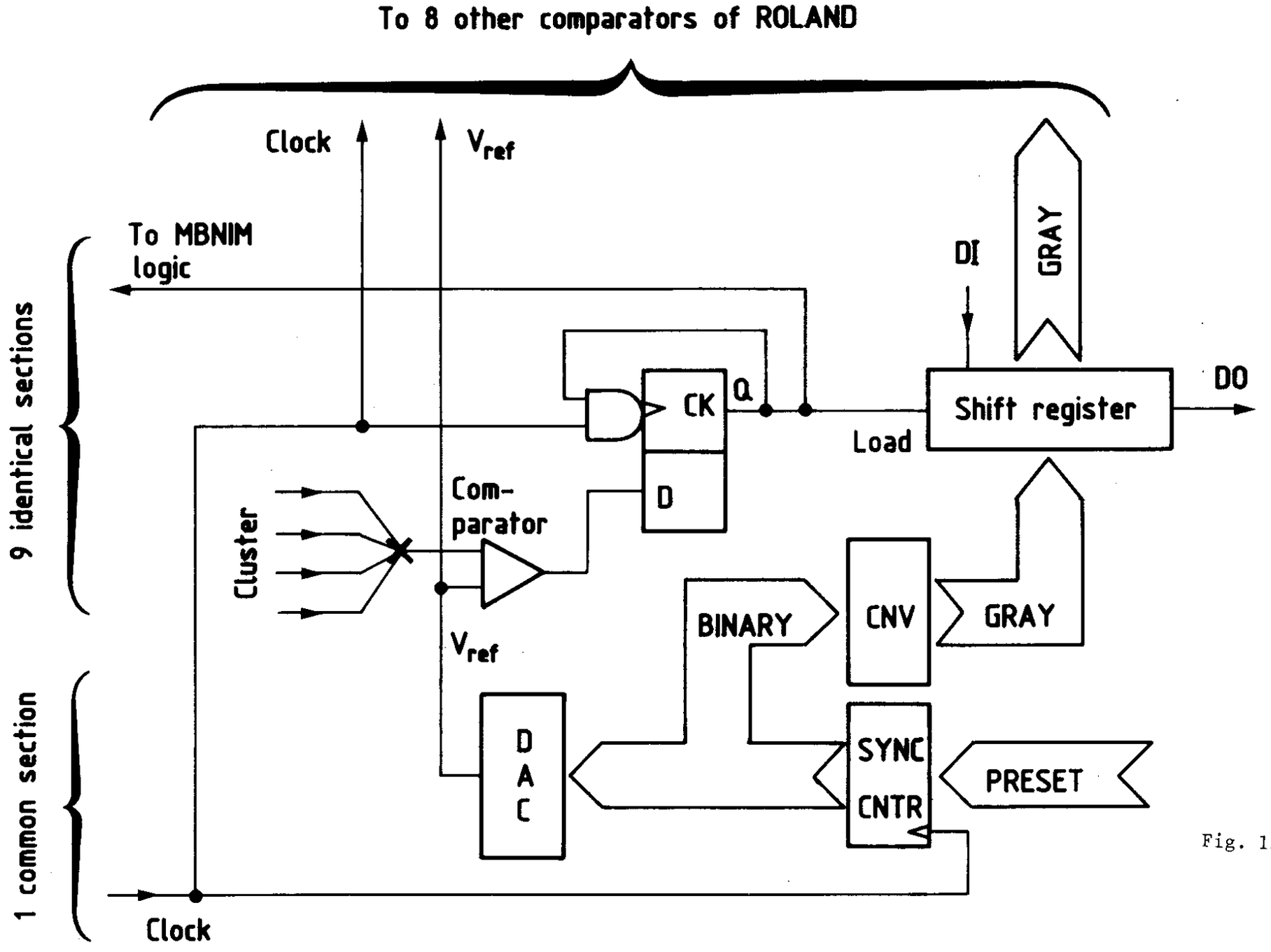
To 8 other comparators of ROLAND
Clock
V_{ref}
To MBNIM logic
DI
GRAY
DO
CK
Q
Shift register
Load
D
Com-parator
Cluster
9 identical sections
V_{ref}
BINARY
CNV
GRAY
D A C
SYNC CNTR
PRESET
1 common section
Clock

Fig. 13

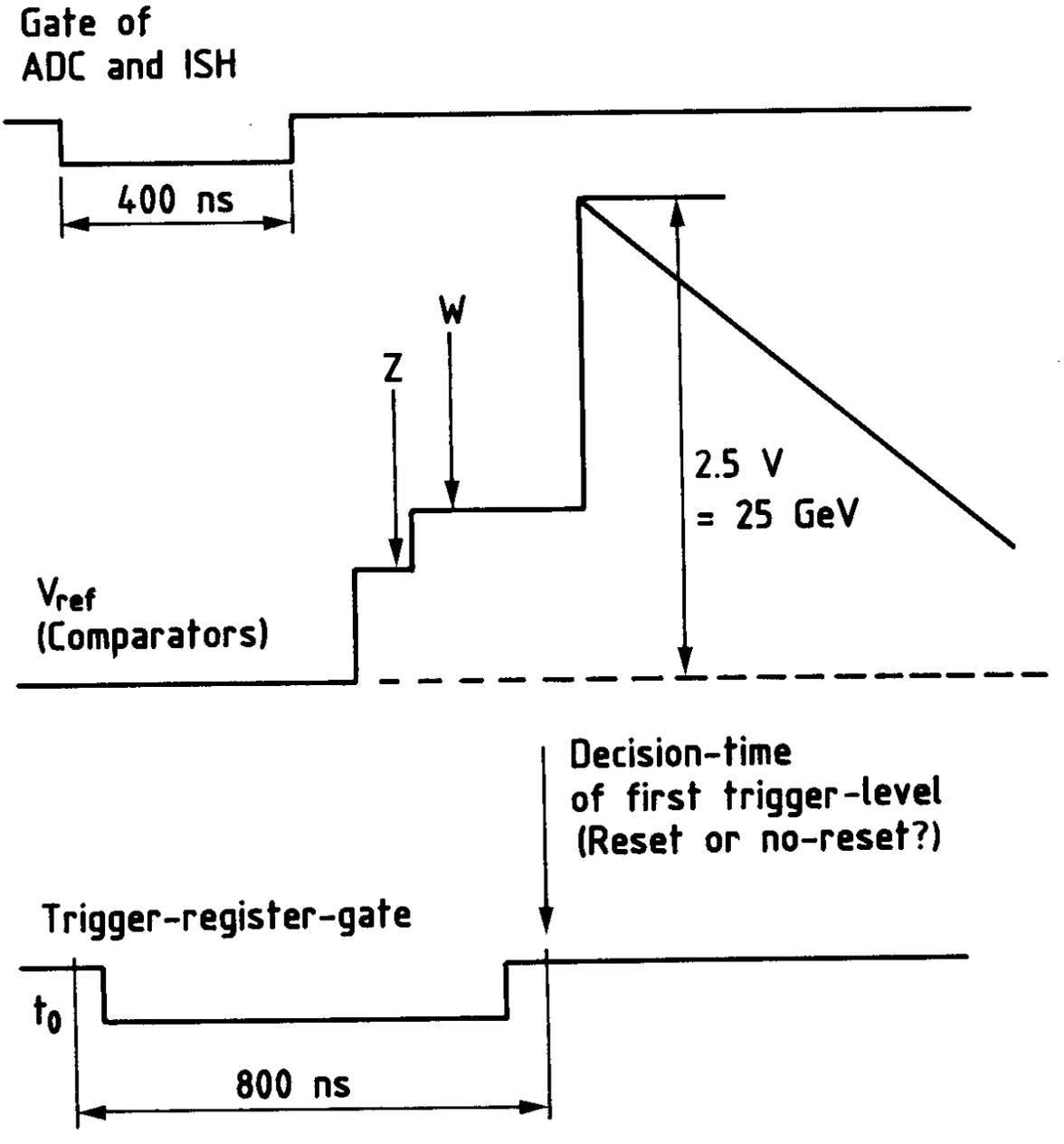
Gate of
ADC and ISH
400 ns
W
Z
2.5 V
= 25 GeV
Vref
(Comparators)
Decision-time
of first trigger-level
(Reset or no-reset?)
Trigger-register-gate
t0
800 ns

Fig. 14

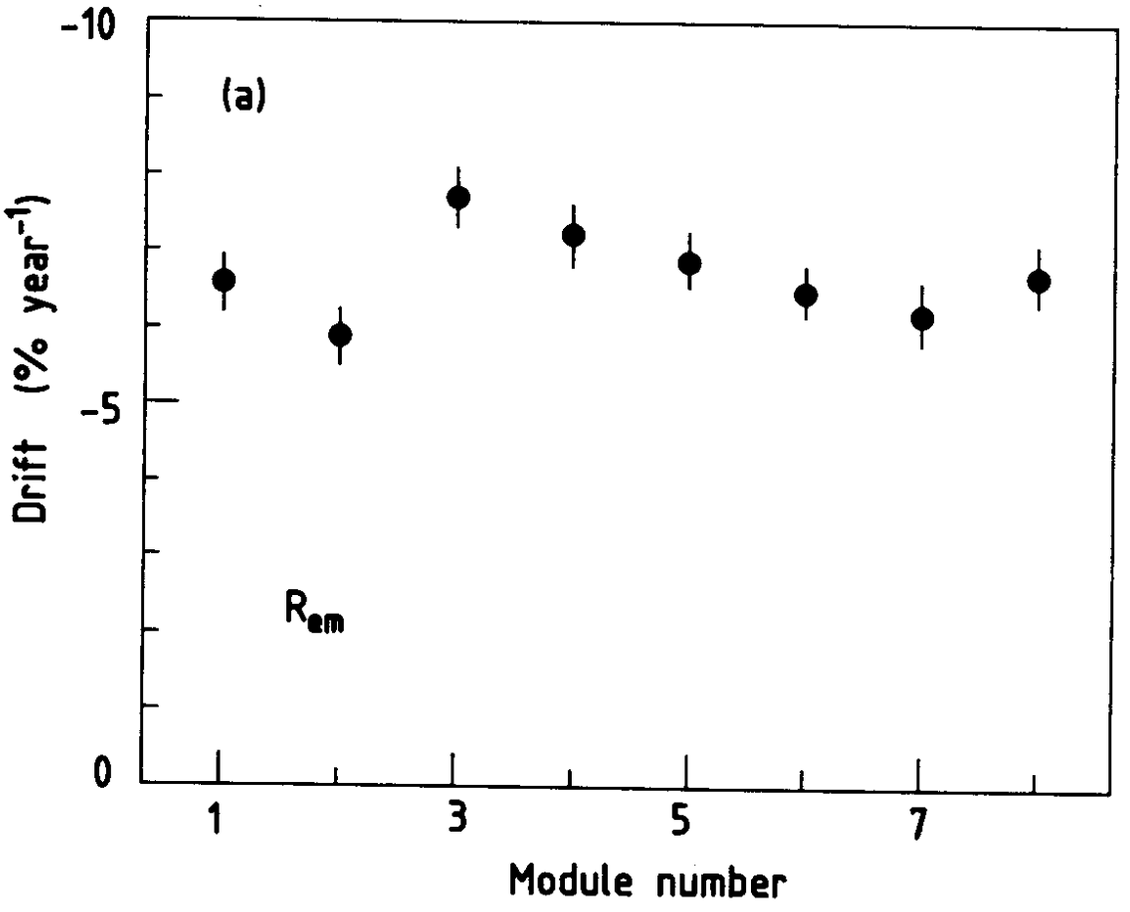

Fig. 15a

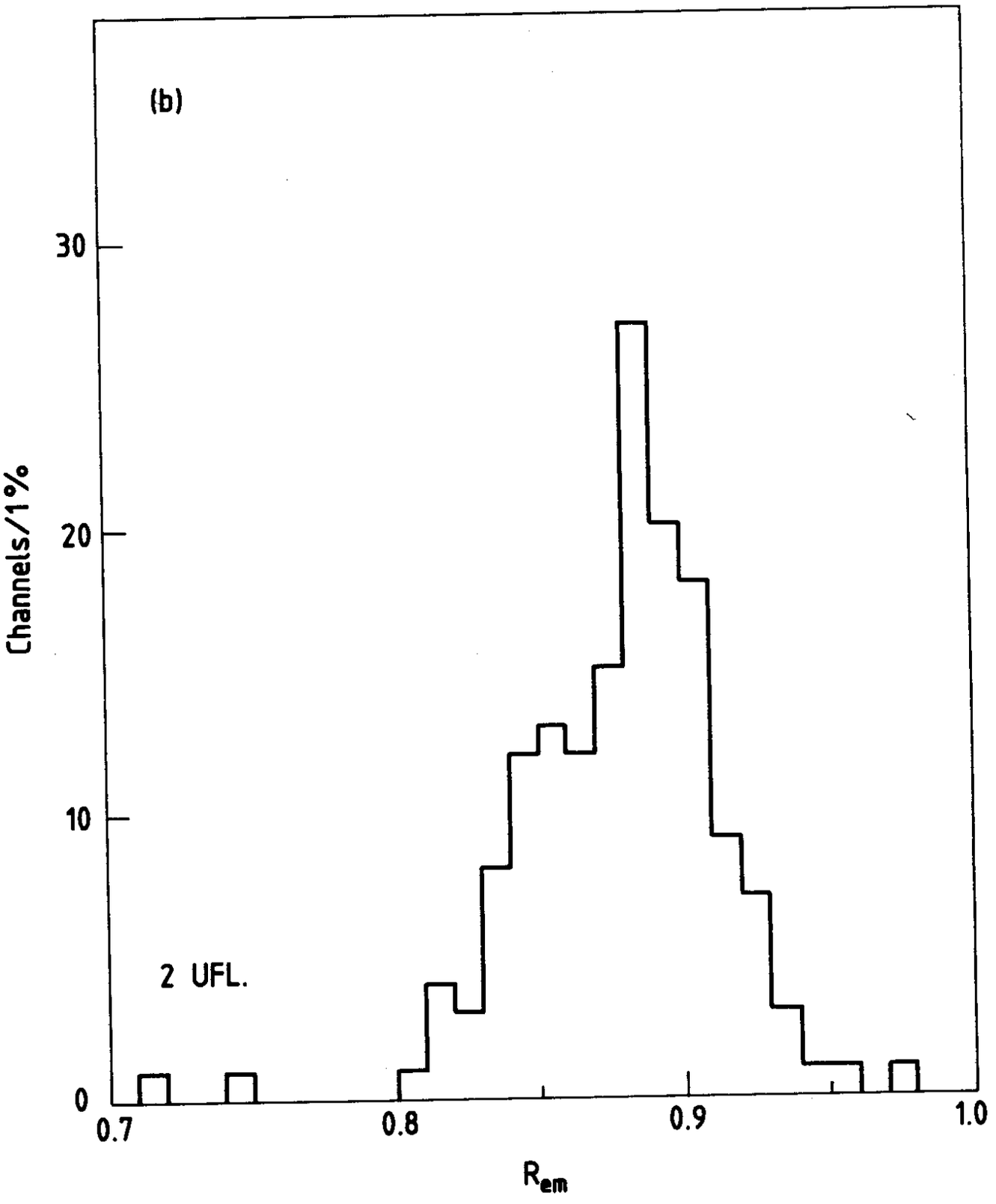

Fig. 15b

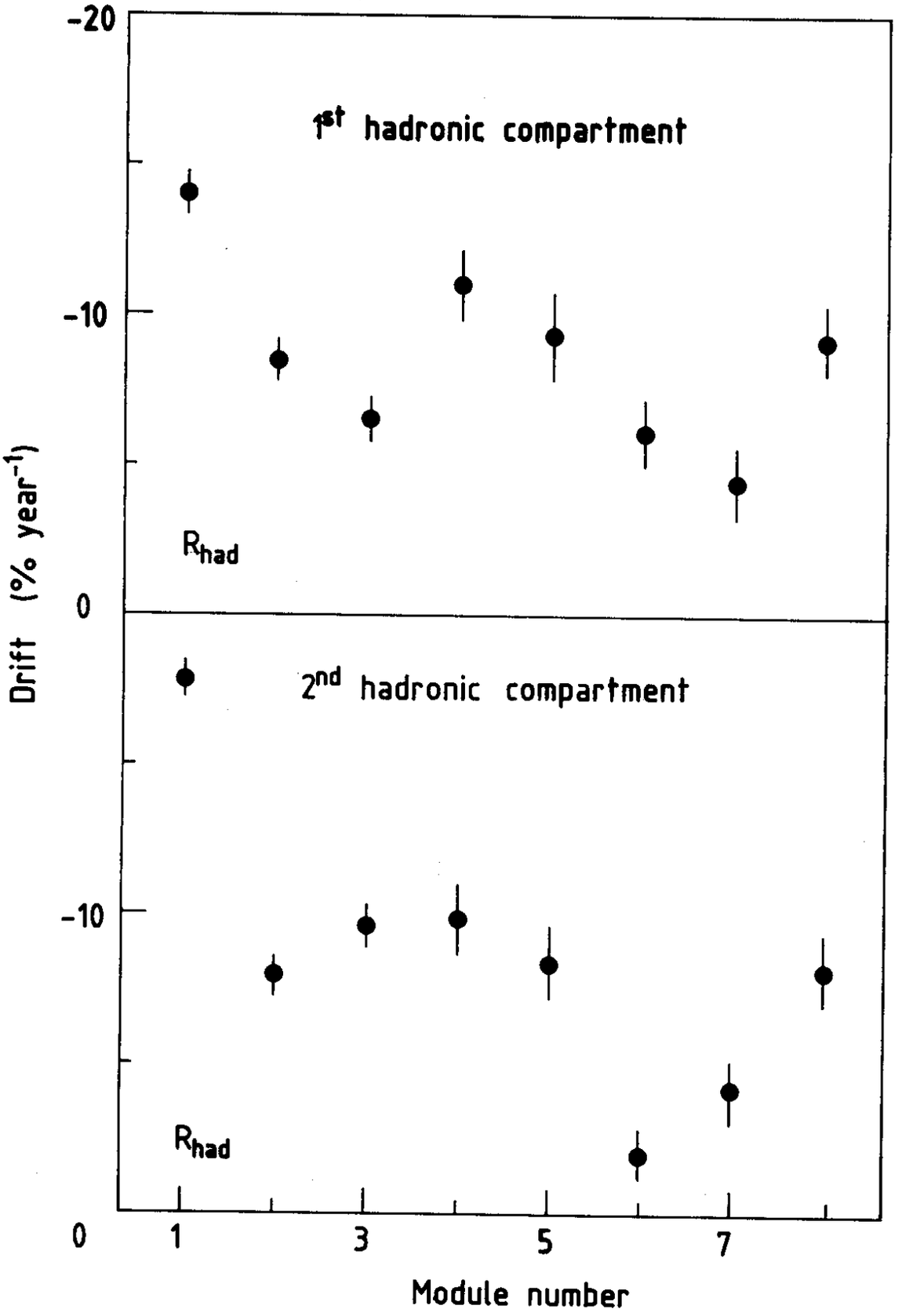
-20
-10
0
1st hadronic compartment
Rhad
Drift (% year-1)
2nd hadronic compartment
-10
Rhad
0
1
3
5
7
Module number

Fig. 16

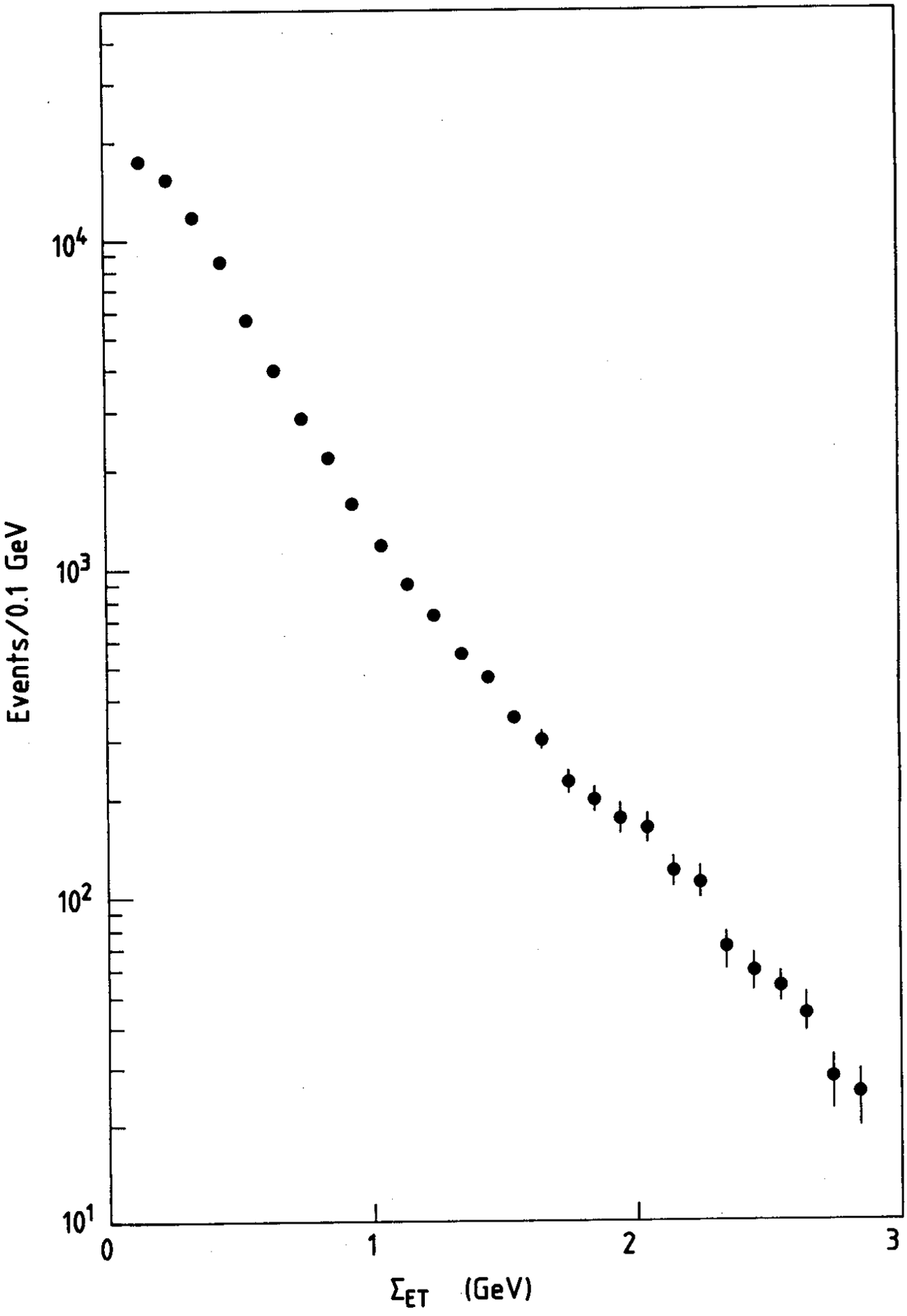

Fig. 17

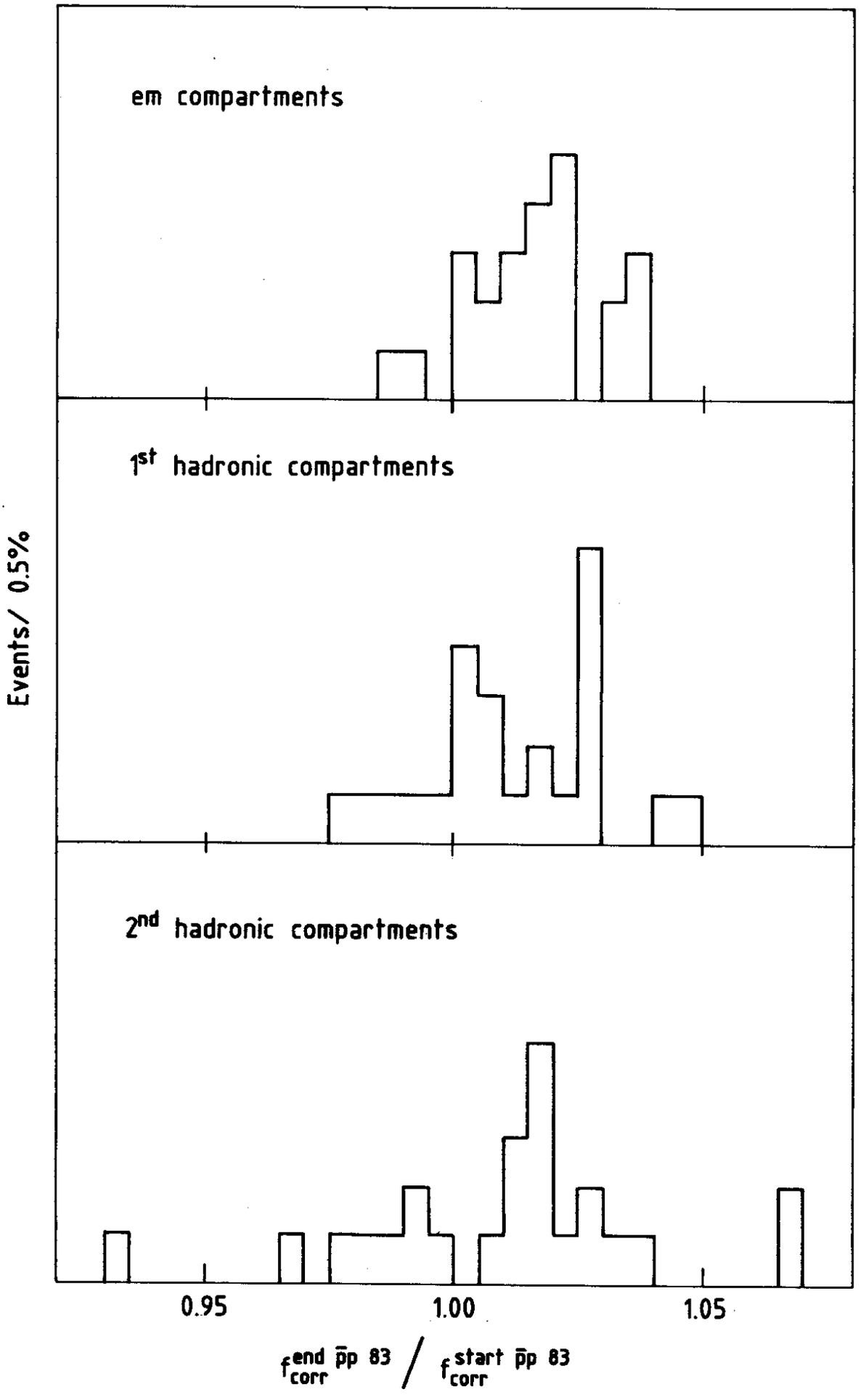
em compartments
1st hadronic compartments
2nd hadronic compartments
Events/ 0.5%
0.95
1.00
1.05
$f_{corr}^{end\ \bar{p}p\ 83} / f_{corr}^{start\ \bar{p}p\ 83}$

Fig. 18

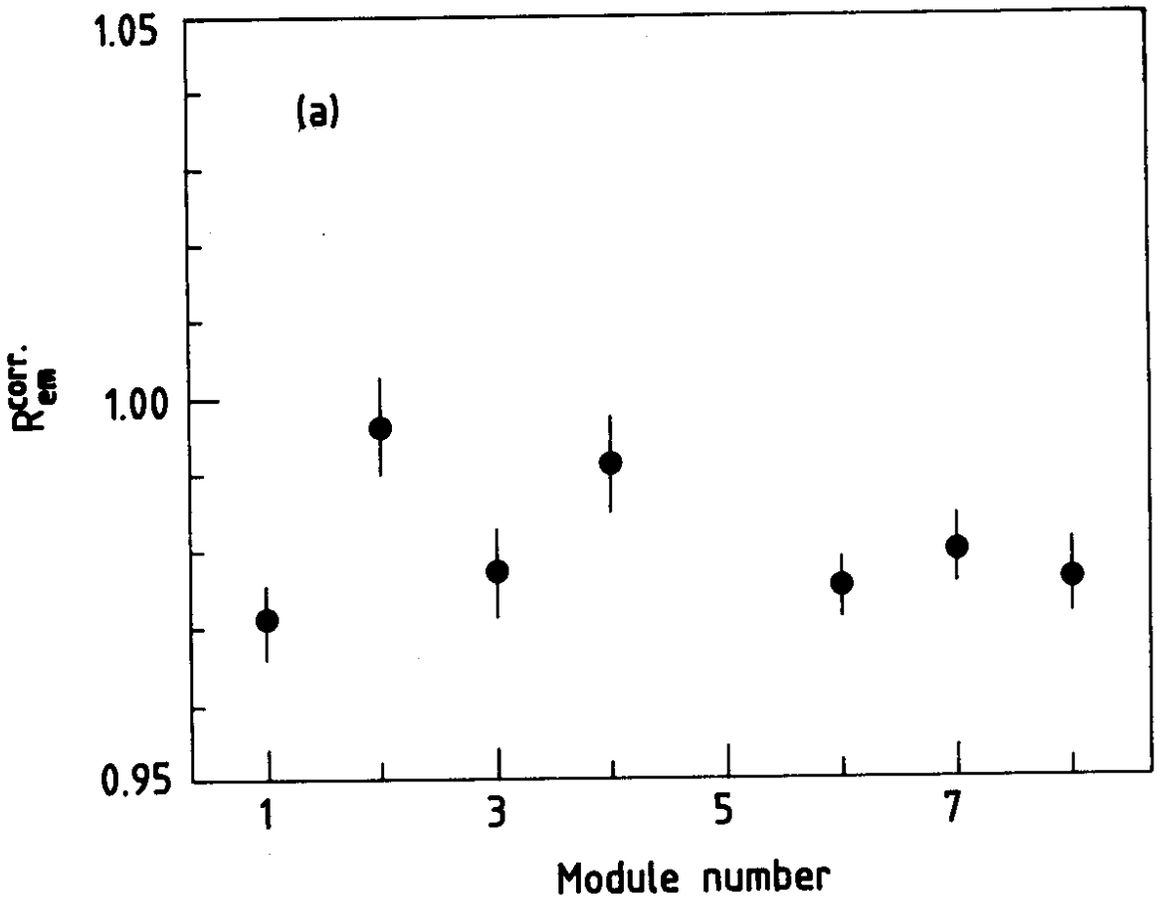

Fig. 19a

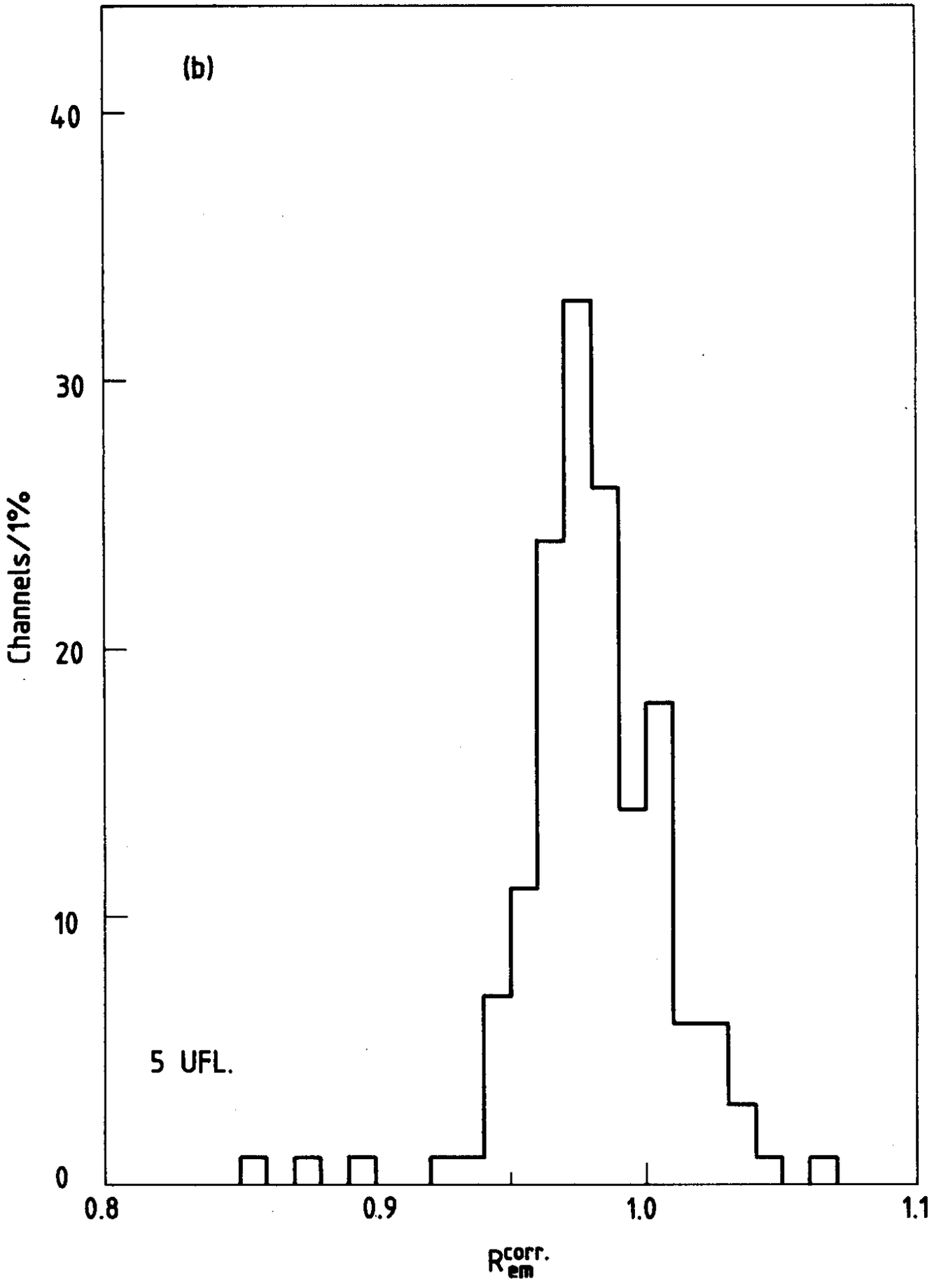

Fig. 19b

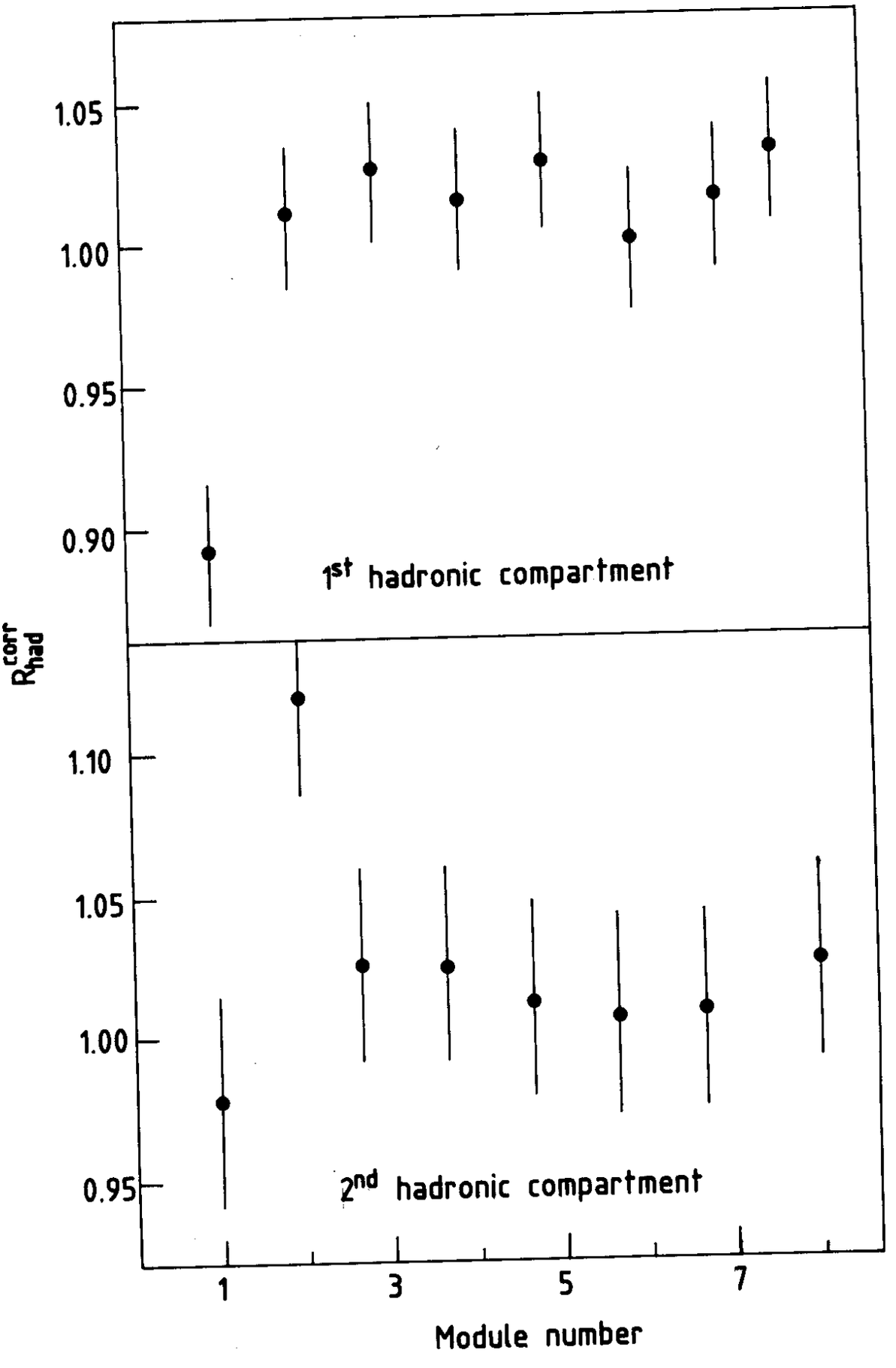
1.05
1.00
0.95
0.90
1st hadronic compartment
R_{had}^{corr}
1.10
1.05
1.00
0.95
2nd hadronic compartment
1
3
5
7
Module number

Fig. 20

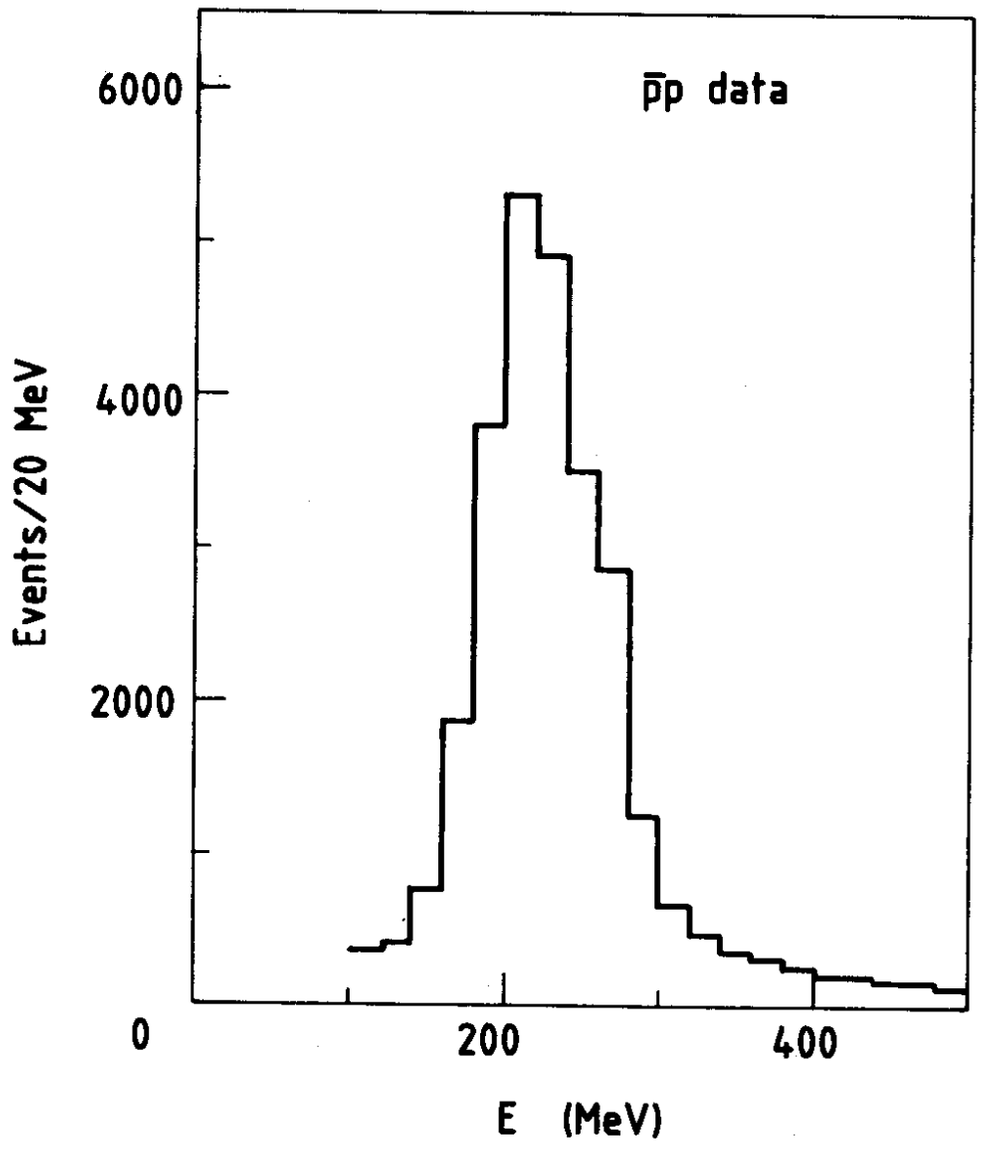

Fig. 21

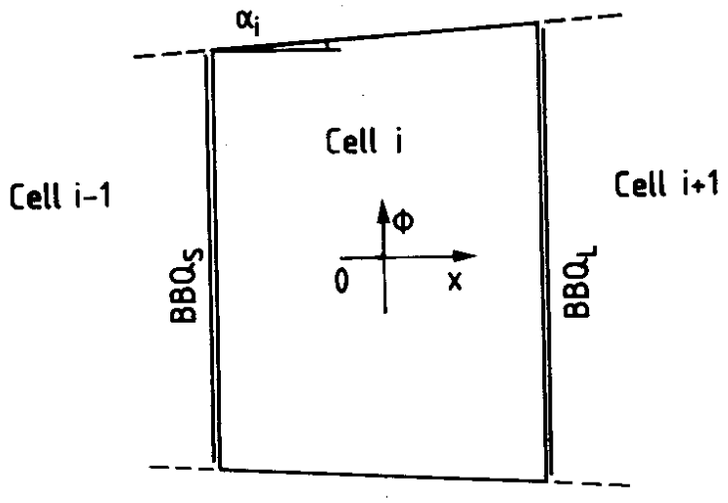

cell i	α_i
1, 10	5.32°
2, 9	4.32°
3, 8	3.18°
4, 7	1.95°
5, 6	0.66°

Fig. 22

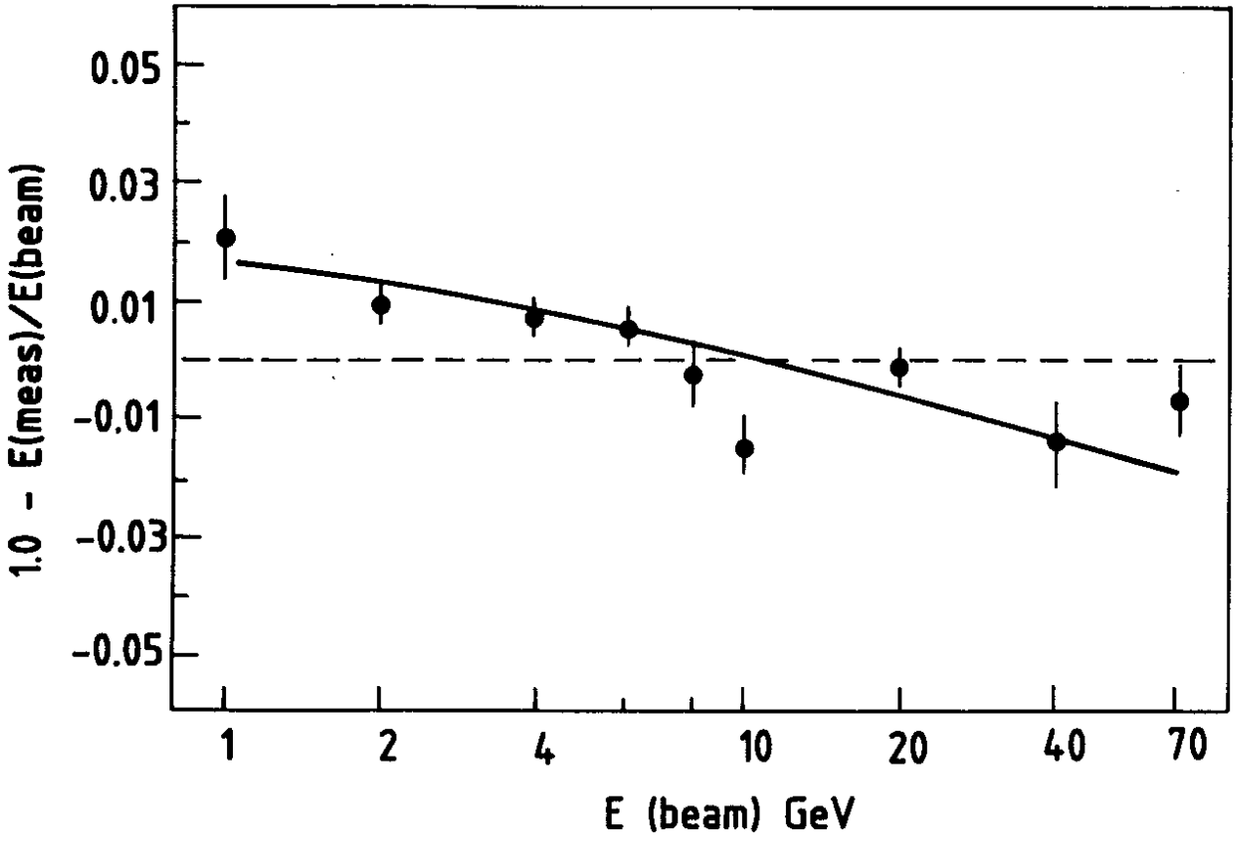

Fig. 23

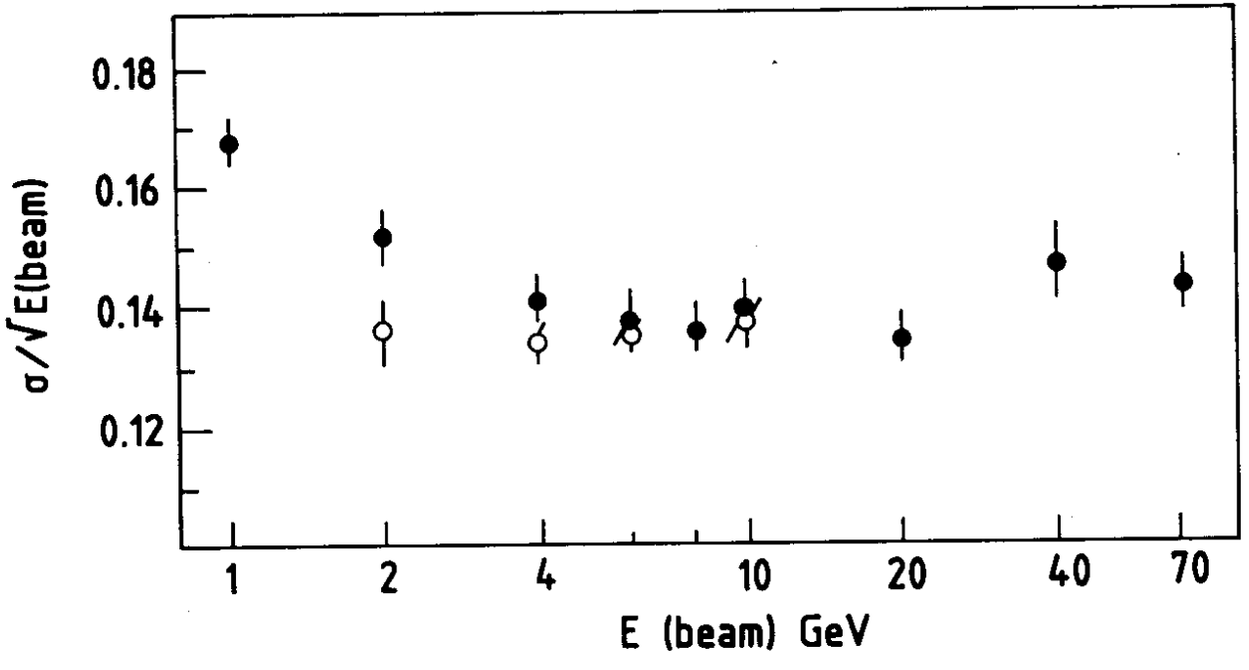

Fig. 24

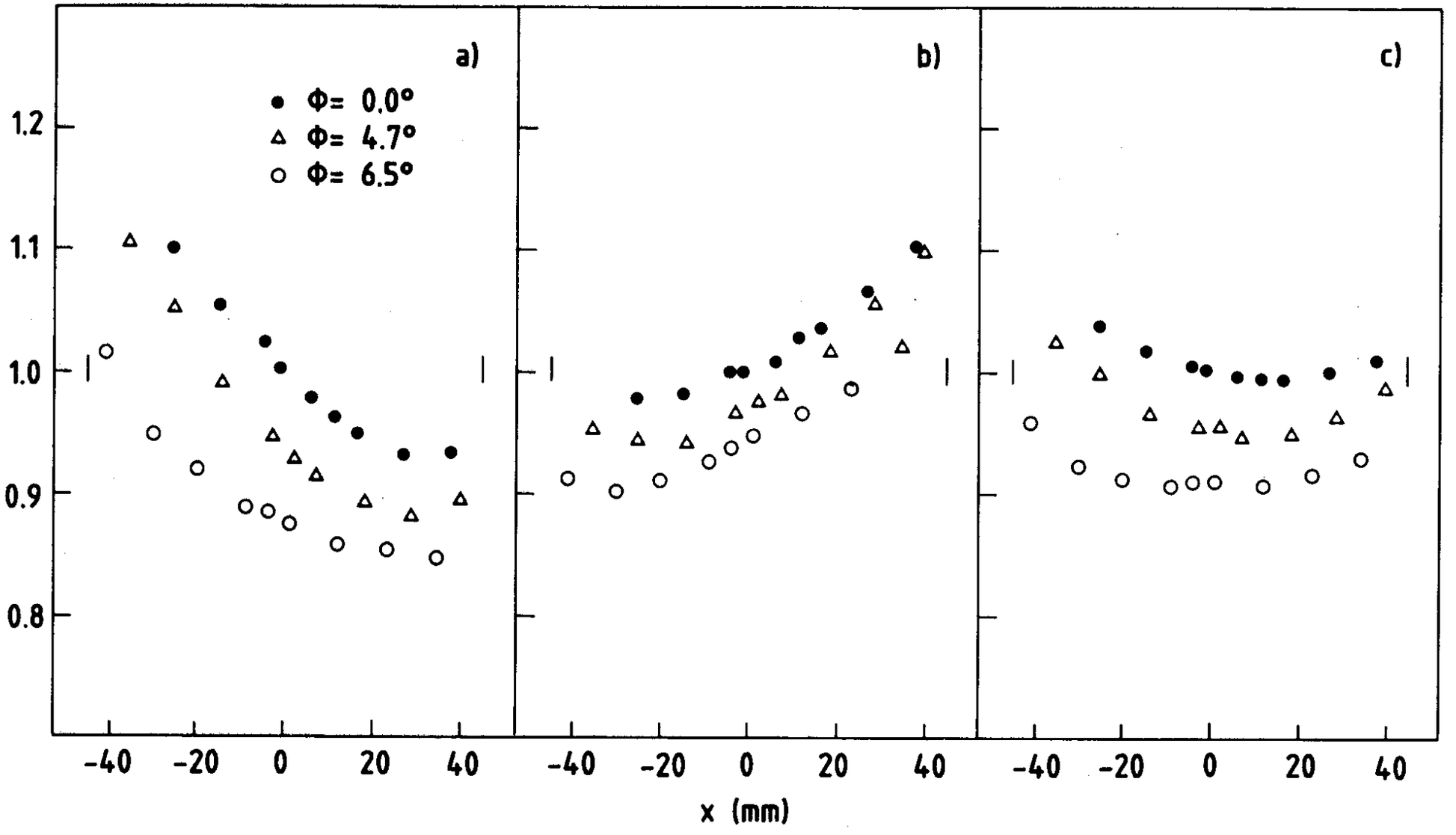

Fig. 25

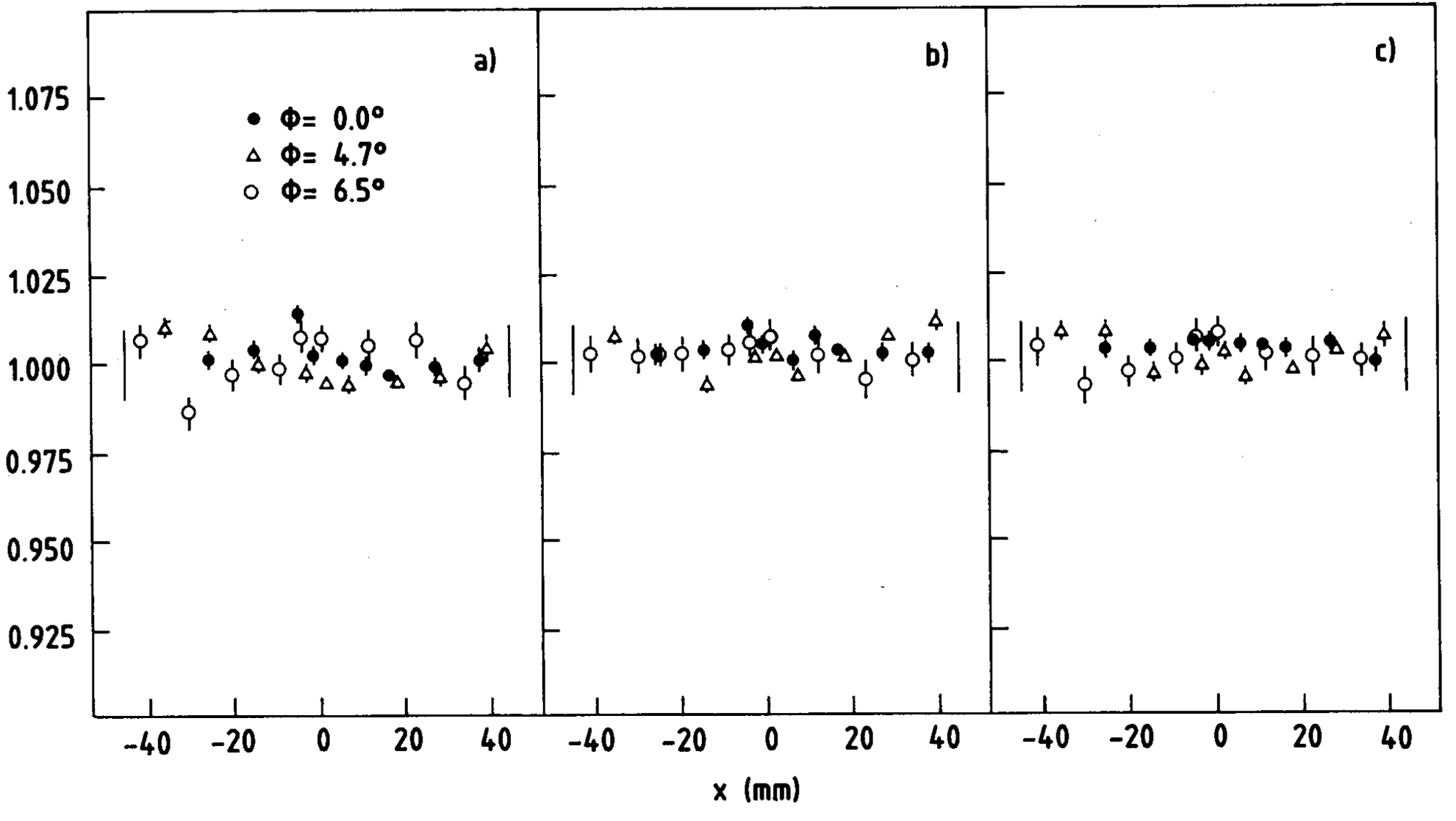
a)
b)
c)
● Φ= 0.0°
△ Φ= 4.7°
○ Φ= 6.5°
1.075
1.050
1.025
1.000
0.975
0.950
0.925
-40
-20
0
20
40
x (mm)

Fig. 26

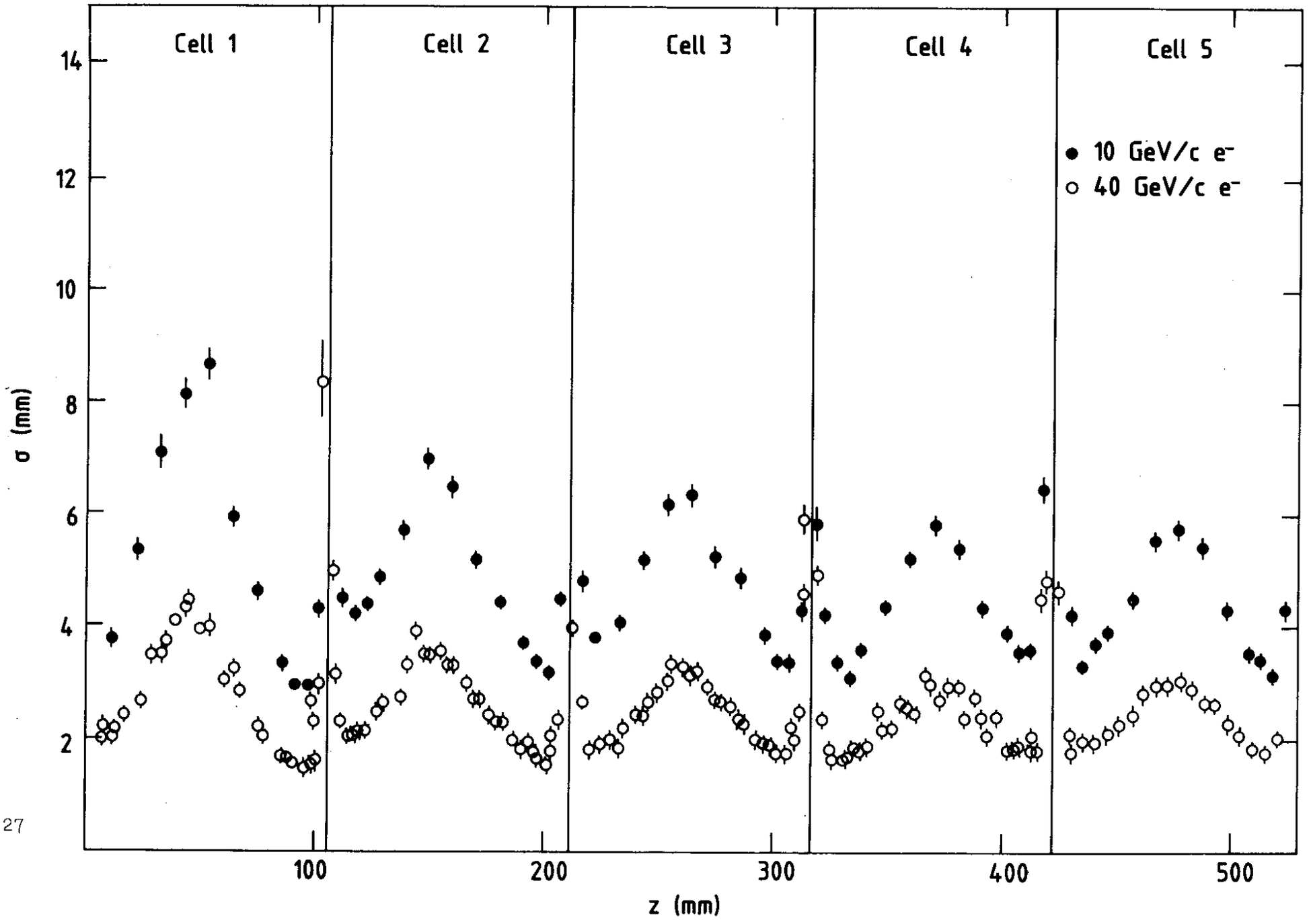
Cell 1
Cell 2
Cell 3
Cell 4
Cell 5
● 10 GeV/c e⁻
○ 40 GeV/c e⁻
σ (mm)
z (mm)
2
4
6
8
10
12
14
100
200
300
400
500

Fig.27

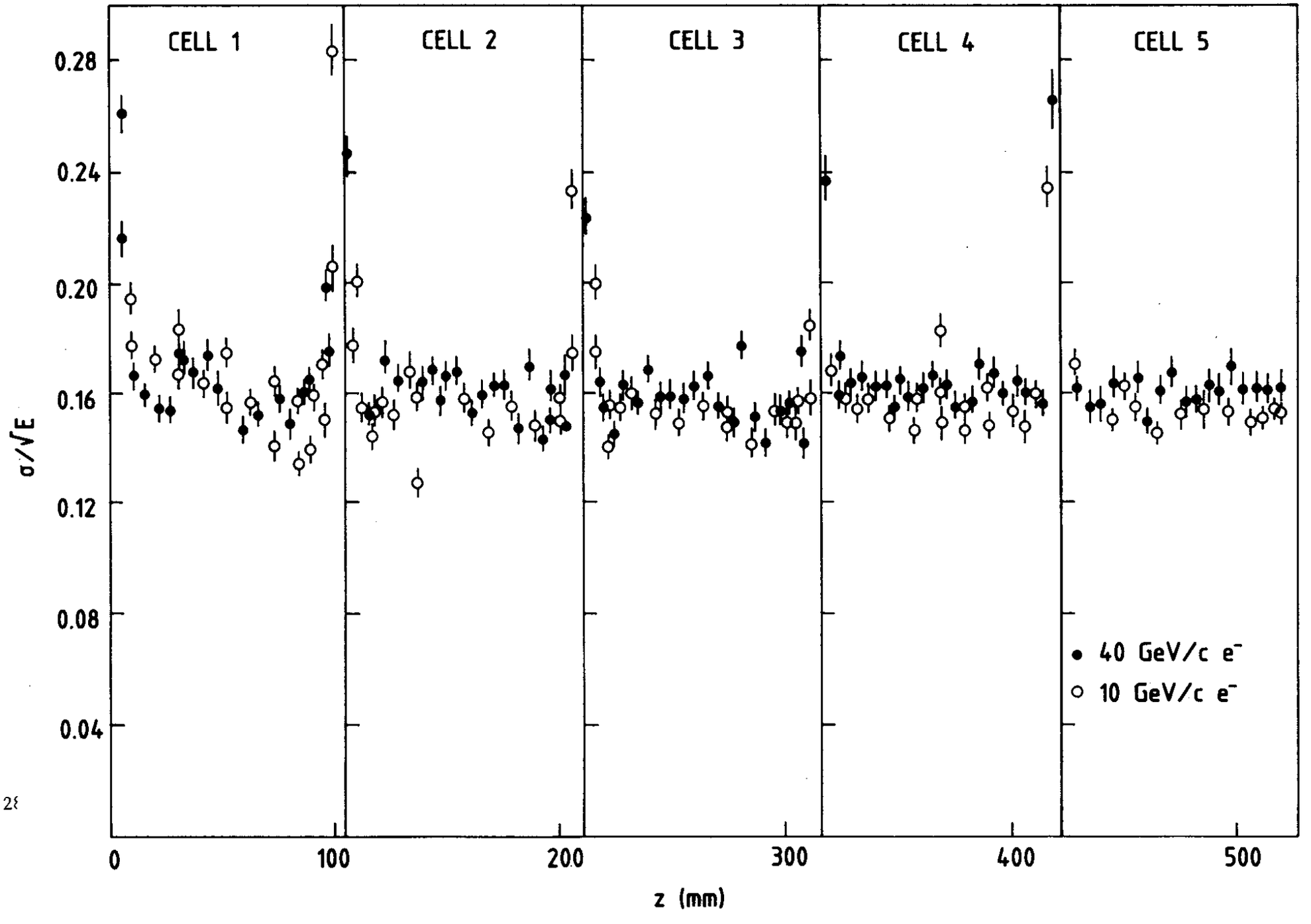
CELL 1
CELL 2
CELL 3
CELL 4
CELL 5
0.28
0.24
0.20
0.16
0.12
0.08
0.04
σ/√E
0
100
200
300
400
500
z (mm)
● 40 GeV/c e⁻
○ 10 GeV/c e⁻

Fig. 2

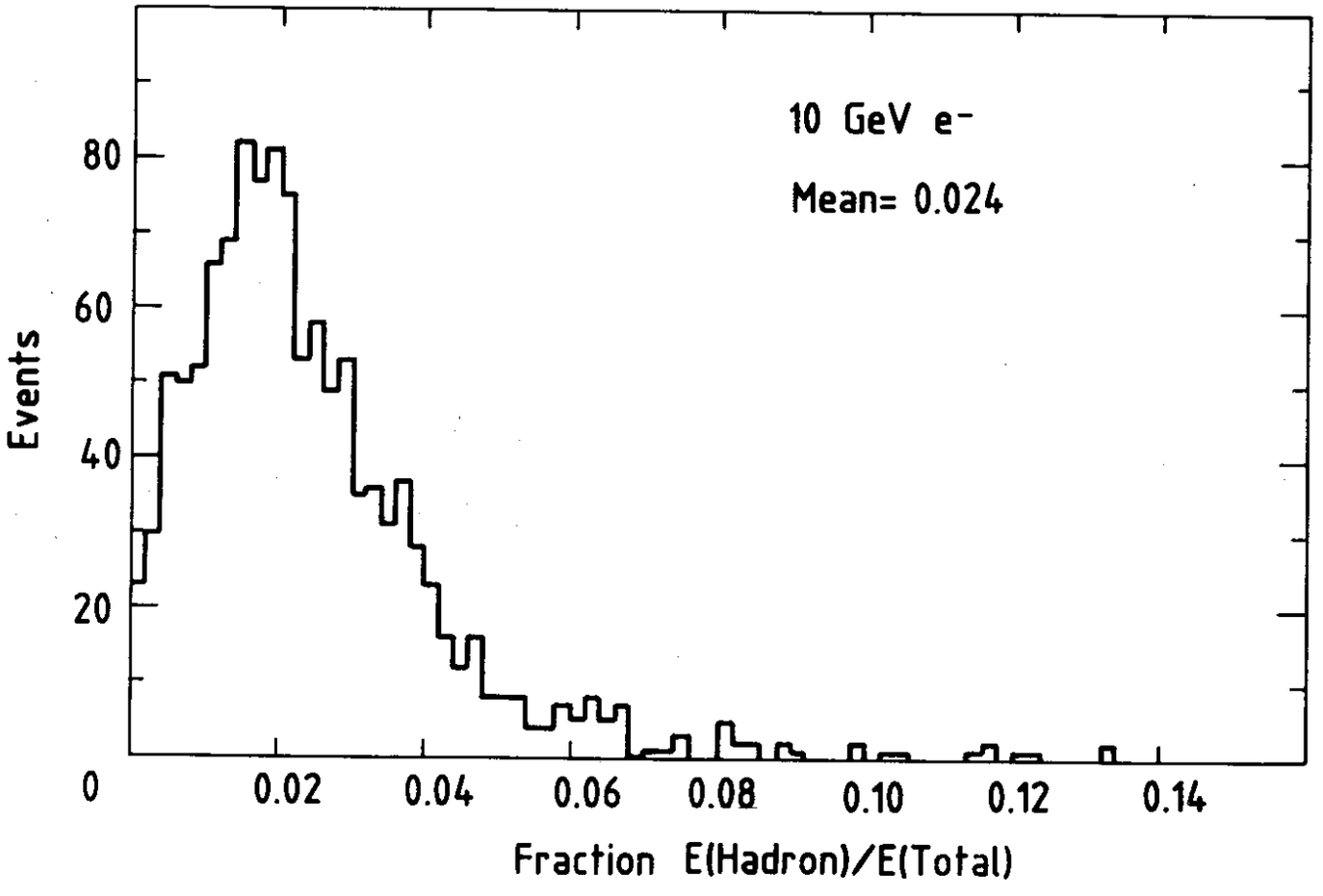
10 GeV e⁻
Mean= 0.024
Events
80
60
40
20
0
0.02
0.04
0.06
0.08
0.10
0.12
0.14
Fraction E(Hadron)/E(Total)

Fig. 29

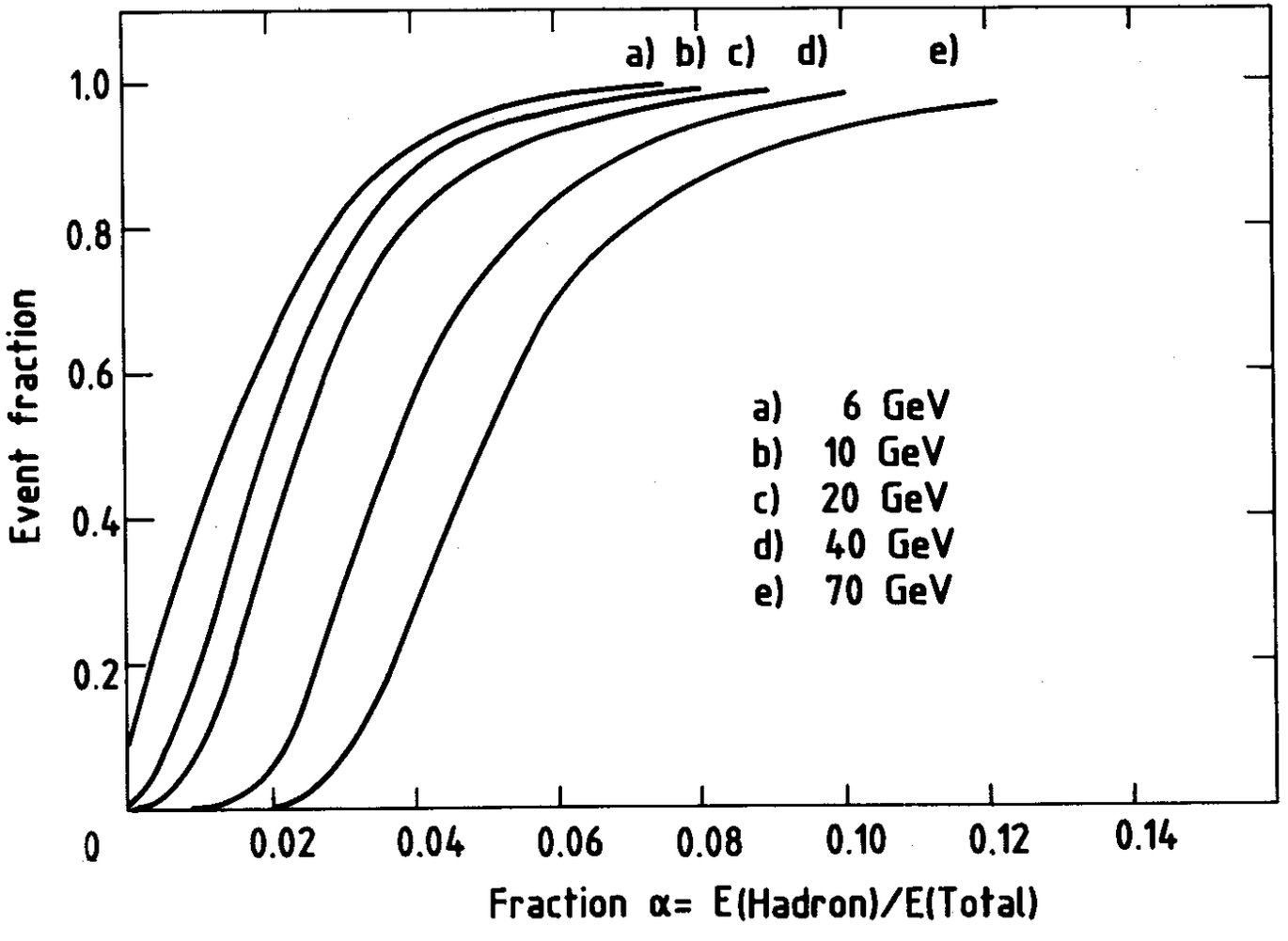
a) b) c) d) e)
1.0
0.8
0.6
0.4
0.2
0
Event fraction
a) 6 GeV
b) 10 GeV
c) 20 GeV
d) 40 GeV
e) 70 GeV
0.02
0.04
0.06
0.08
0.10
0.12
0.14
Fraction α= E(Hadron)/E(Total)

Fig. 30

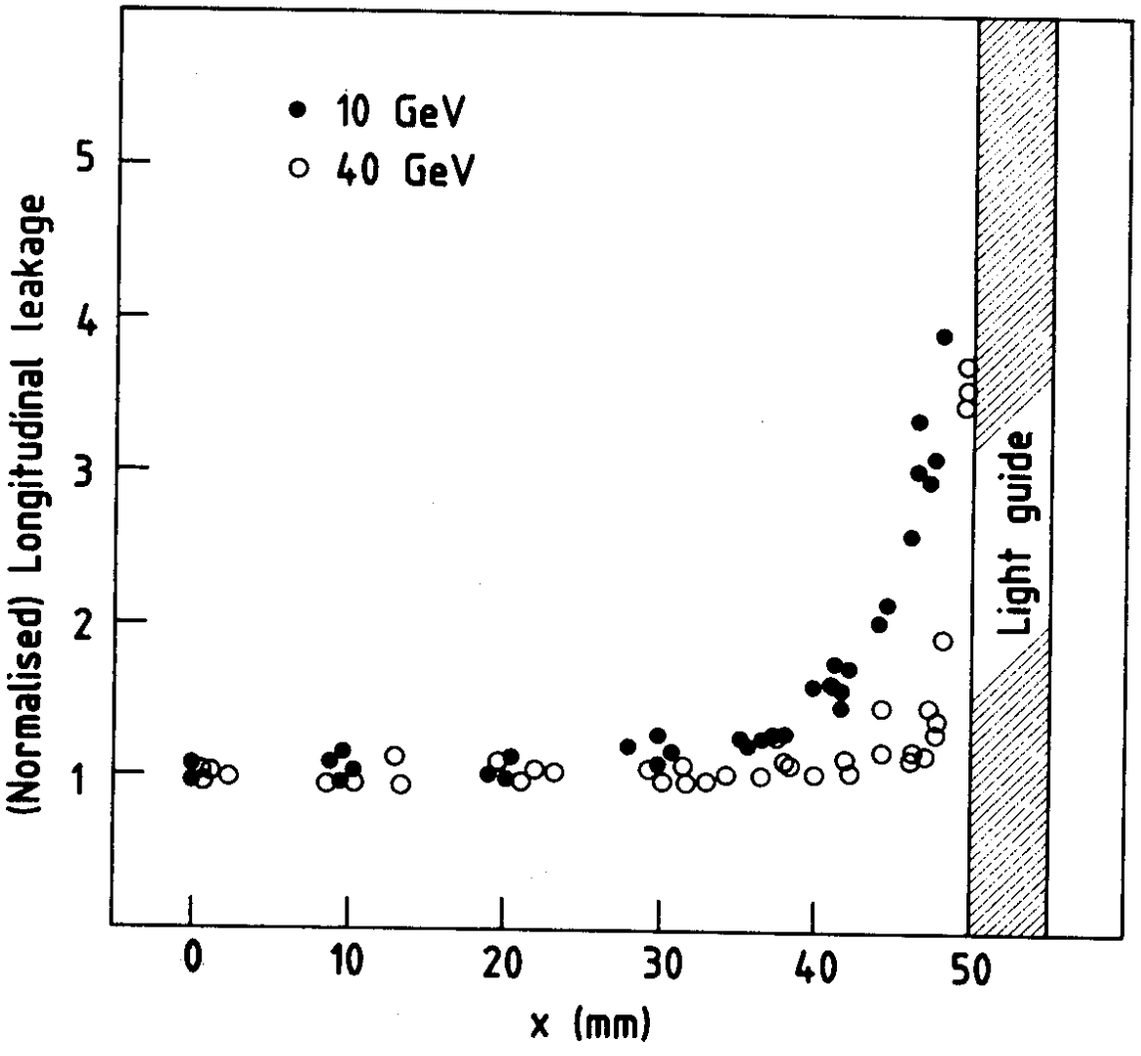
• 10 GeV
○ 40 GeV
(Normalised) Longitudinal leakage
1
2
3
4
5
0
10
20
30
40
50
x (mm)
Light guide

Fig. 31

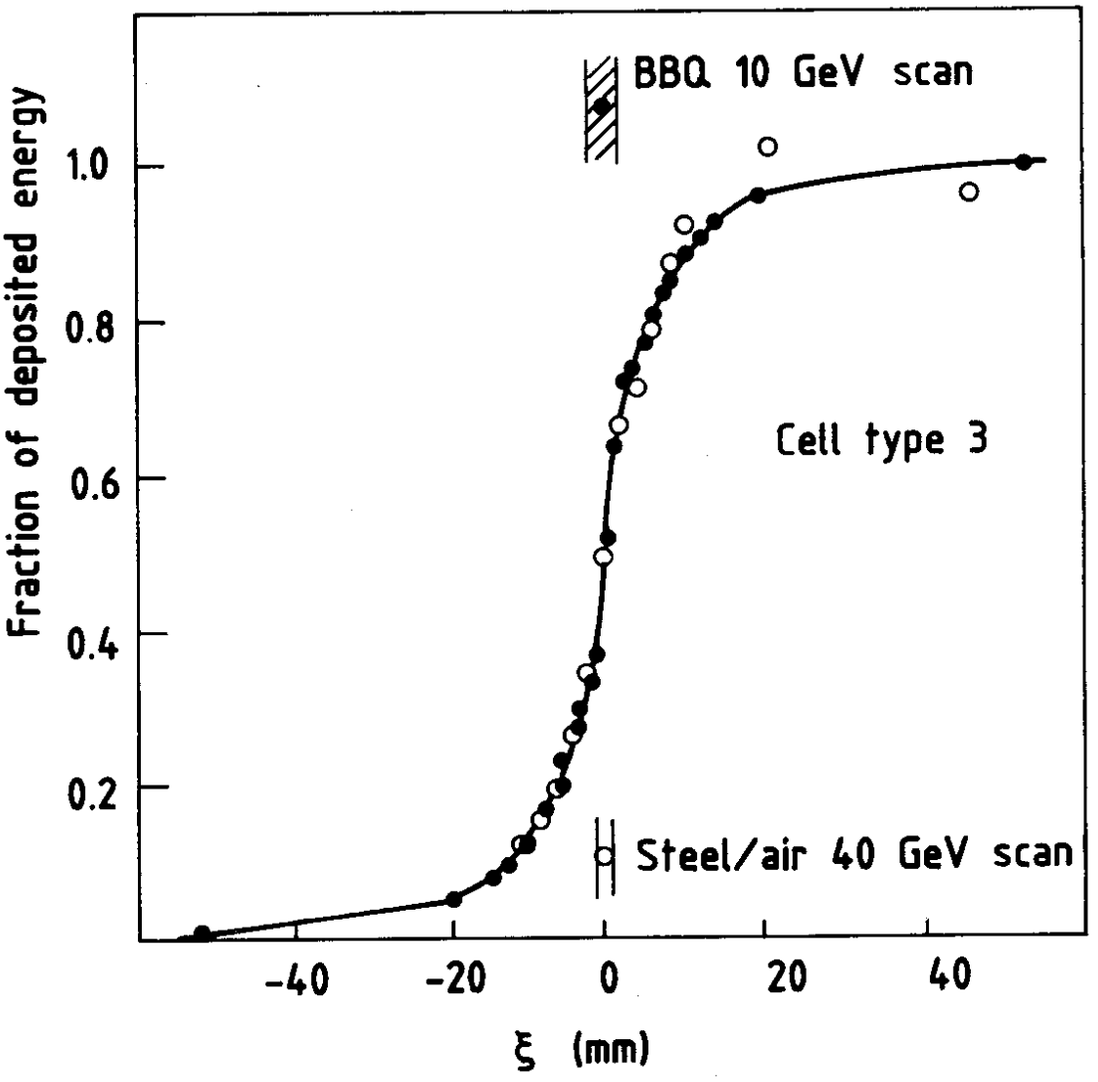
BBQ 10 GeV scan
Cell type 3
Steel/air 40 GeV scan
Fraction of deposited energy
1.0
0.8
0.6
0.4
0.2
-40
-20
0
20
40
ξ (mm)

Fig. 32

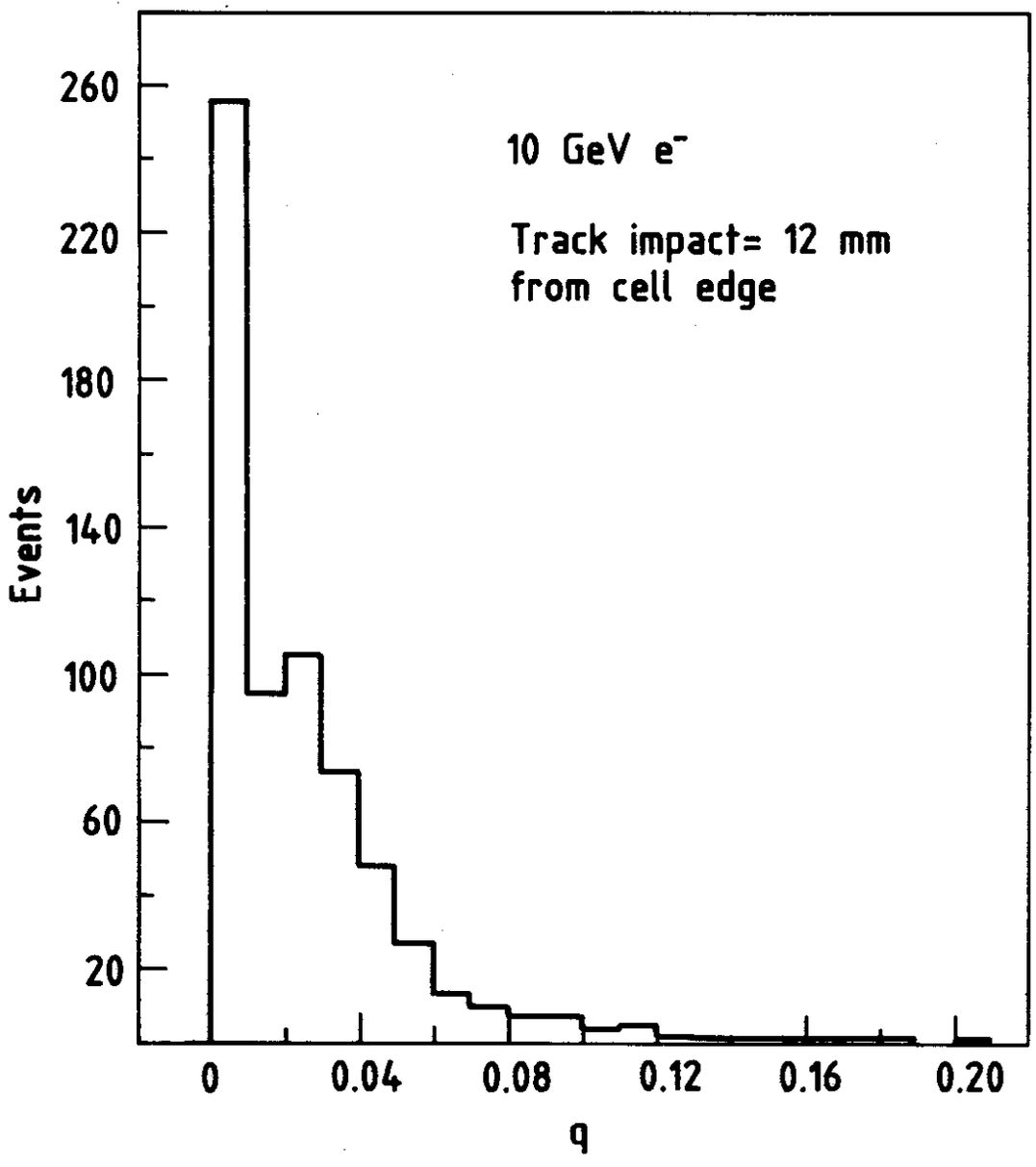
260
220
180
140
100
60
20
Events
10 GeV e⁻
Track impact= 12 mm
from cell edge
0
0.04
0.08
0.12
0.16
0.20
q

Fig. 33

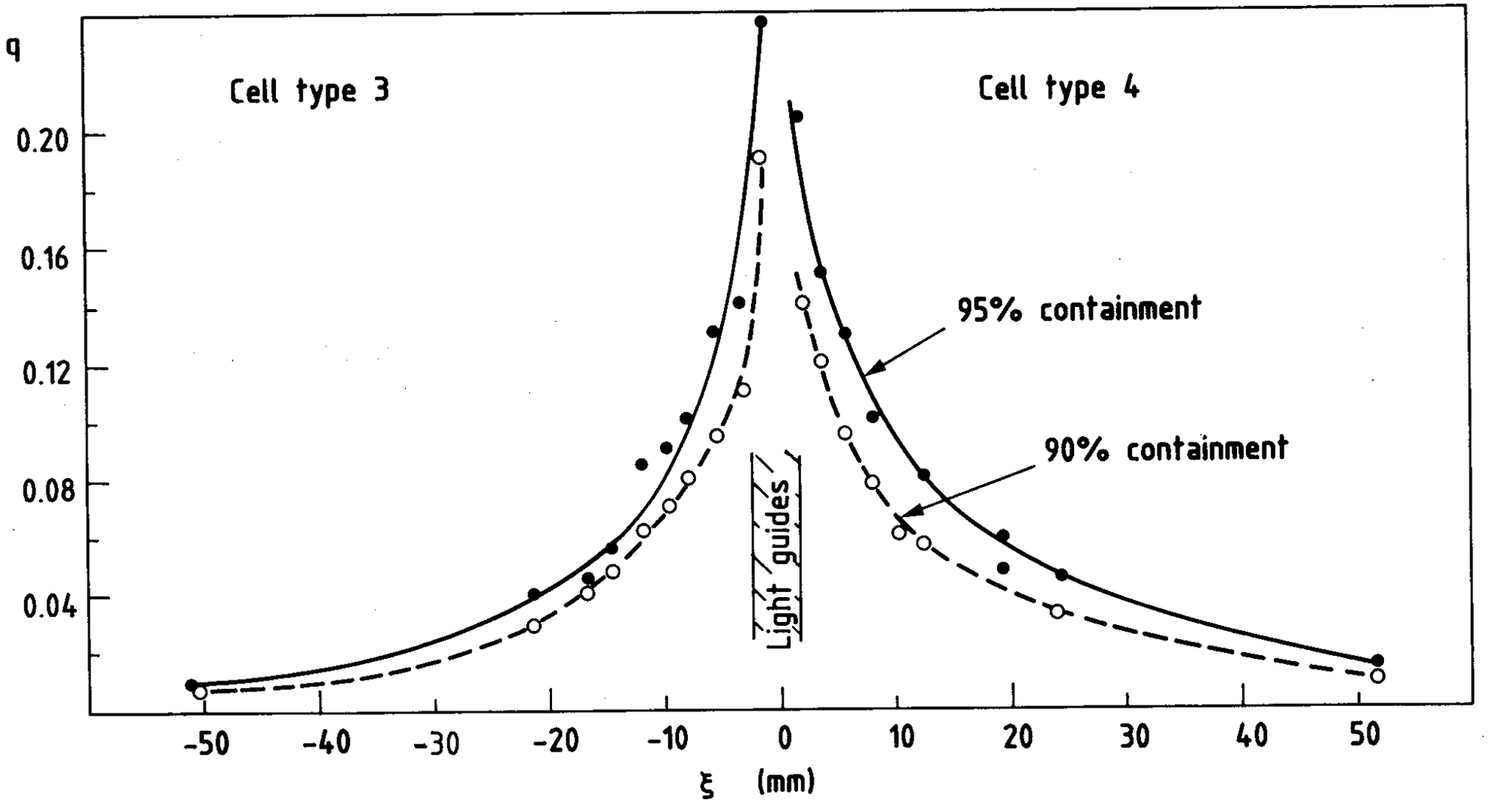
q
Cell type 3
Cell type 4
0.20
0.16
0.12
0.08
0.04
95% containment
90% containment
Light guides
-50
-40
-30
-20
-10
0
10
20
30
40
50
ξ (mm)

Fig. 34

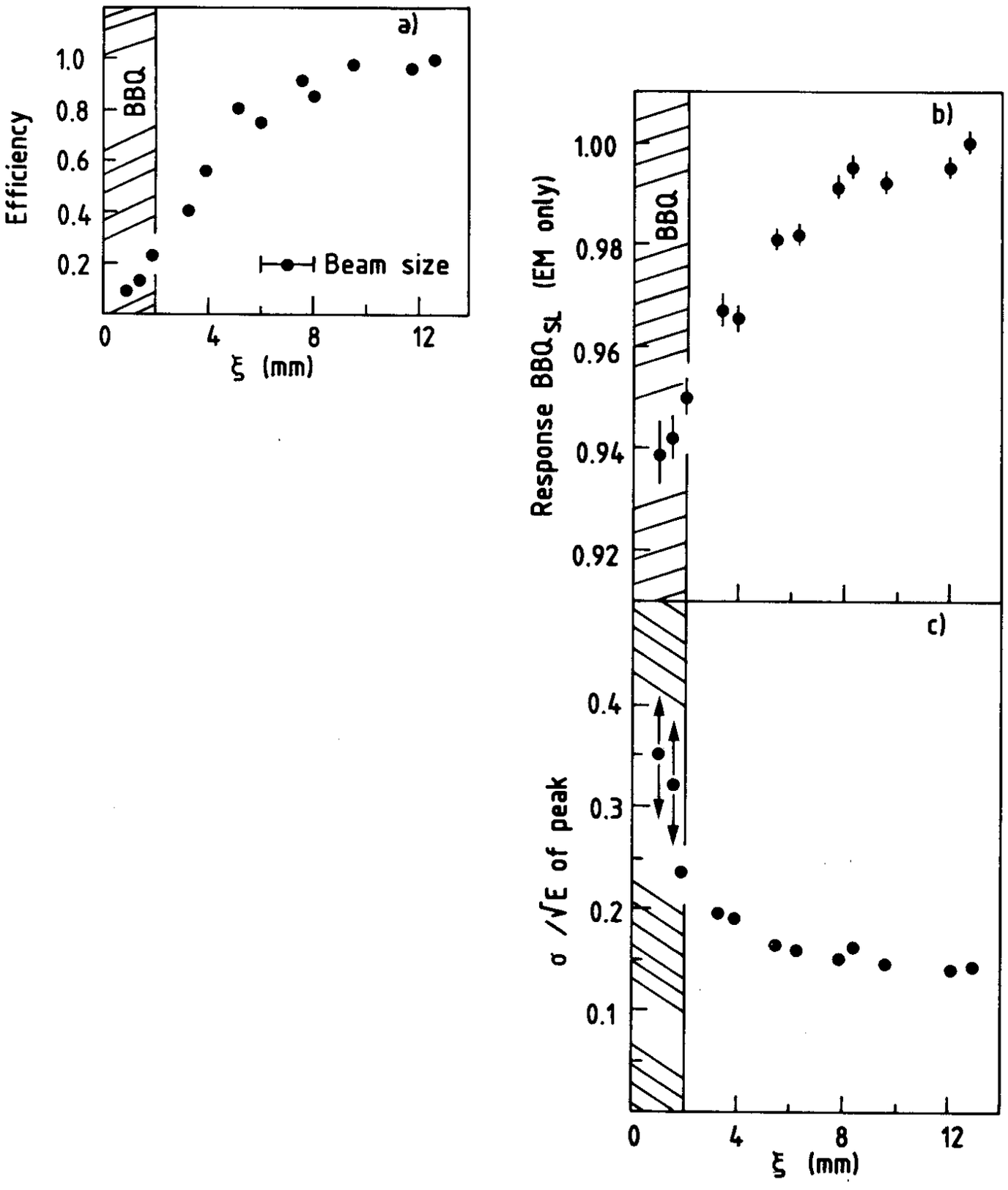
a)
Efficiency
1.0
0.8
0.6
0.4
0.2
BBQ
Beam size
0
4
8
12
ξ (mm)
b)
Response BBQ$_{SL}$ (EM only)
1.00
0.98
0.96
0.94
0.92
BBQ
c)
σ /√E of peak
0.4
0.3
0.2
0.1
0
4
8
12
ξ (mm)

Fig. 35

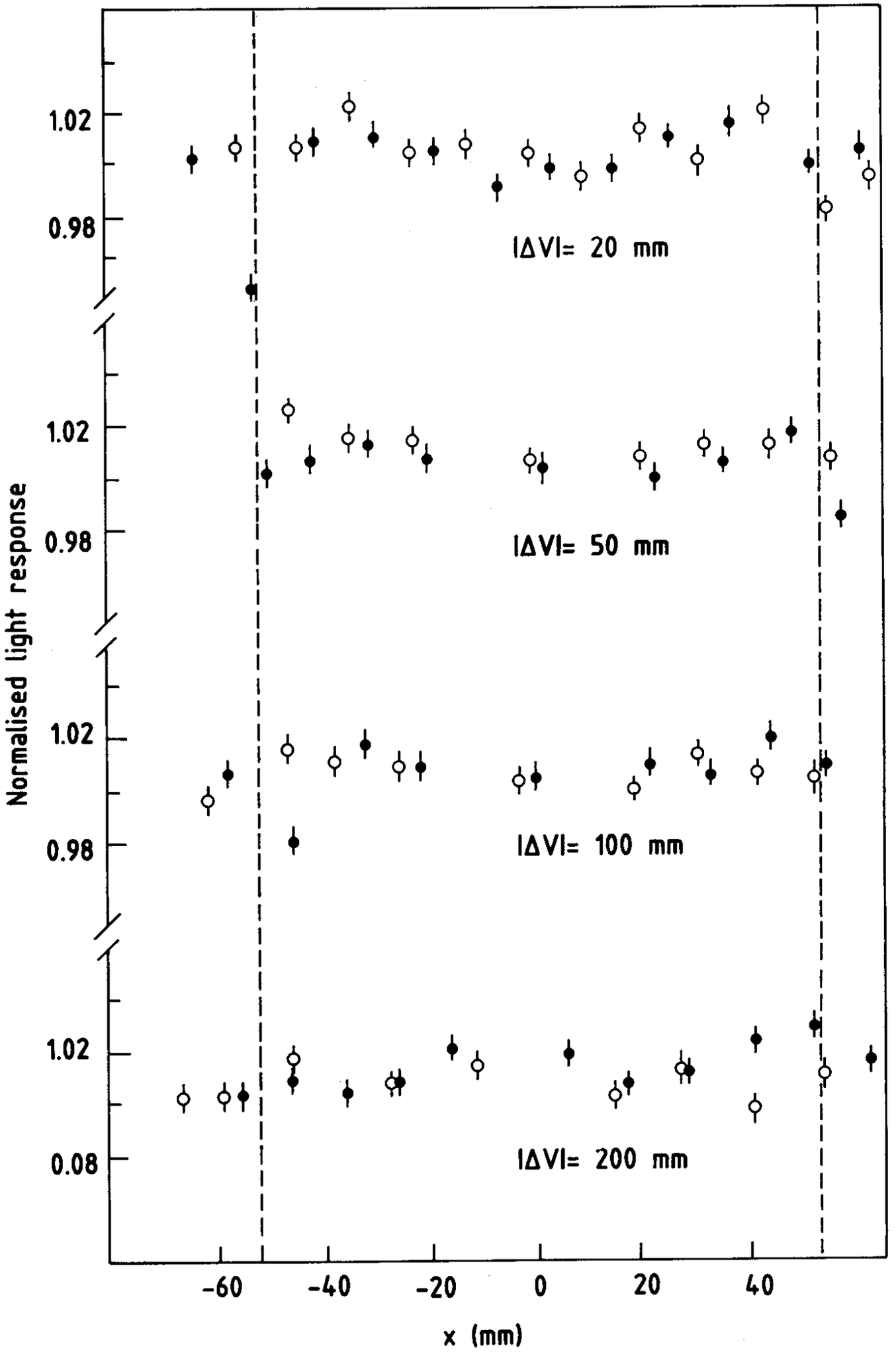
Normalised light response
1.02
0.98
|ΔV|= 20 mm
1.02
0.98
|ΔV|= 50 mm
1.02
0.98
|ΔV|= 100 mm
1.02
0.08
|ΔV|= 200 mm
-60
-40
-20
0
20
40
x (mm)

Fig. 36

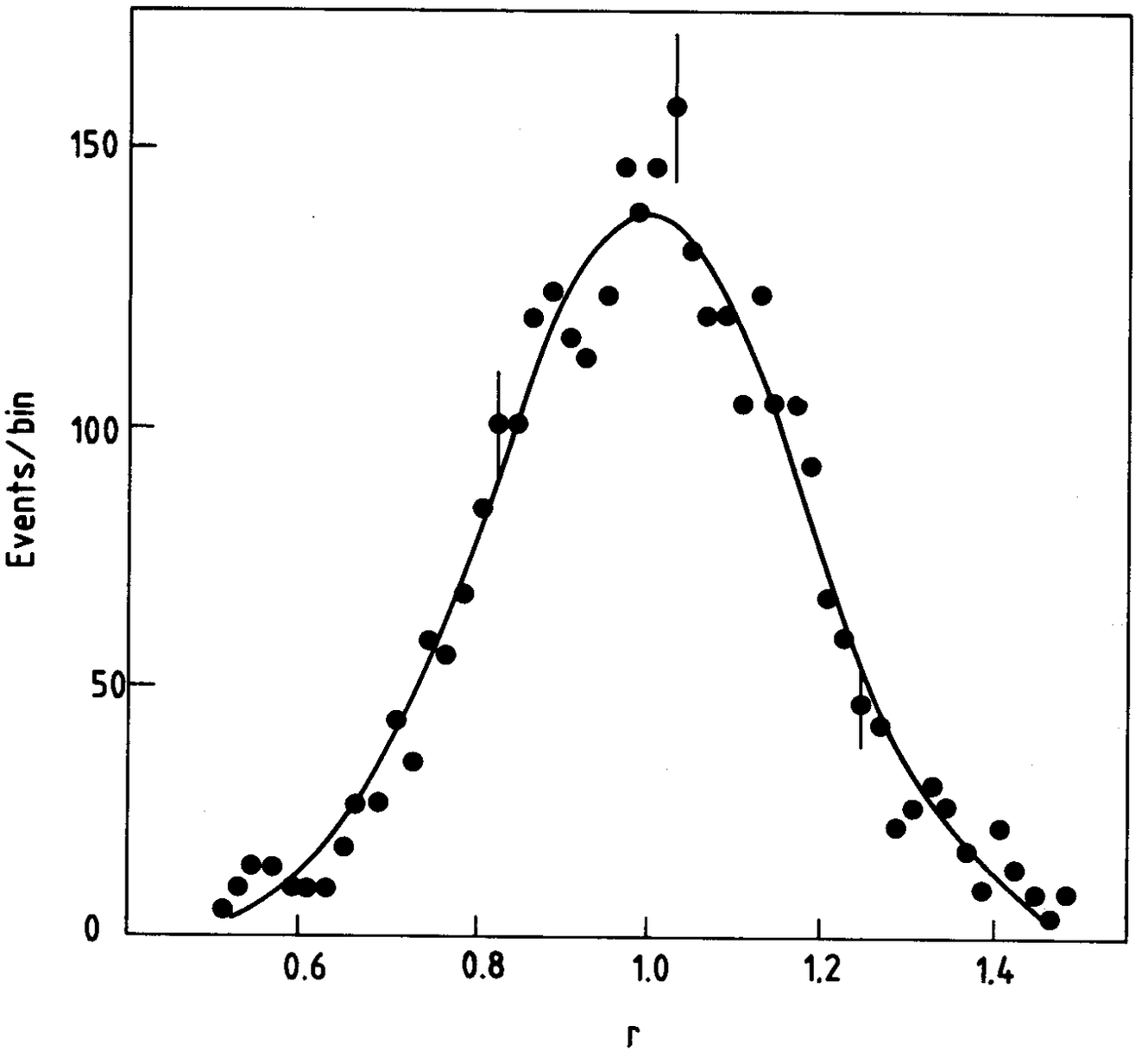

Fig. 37

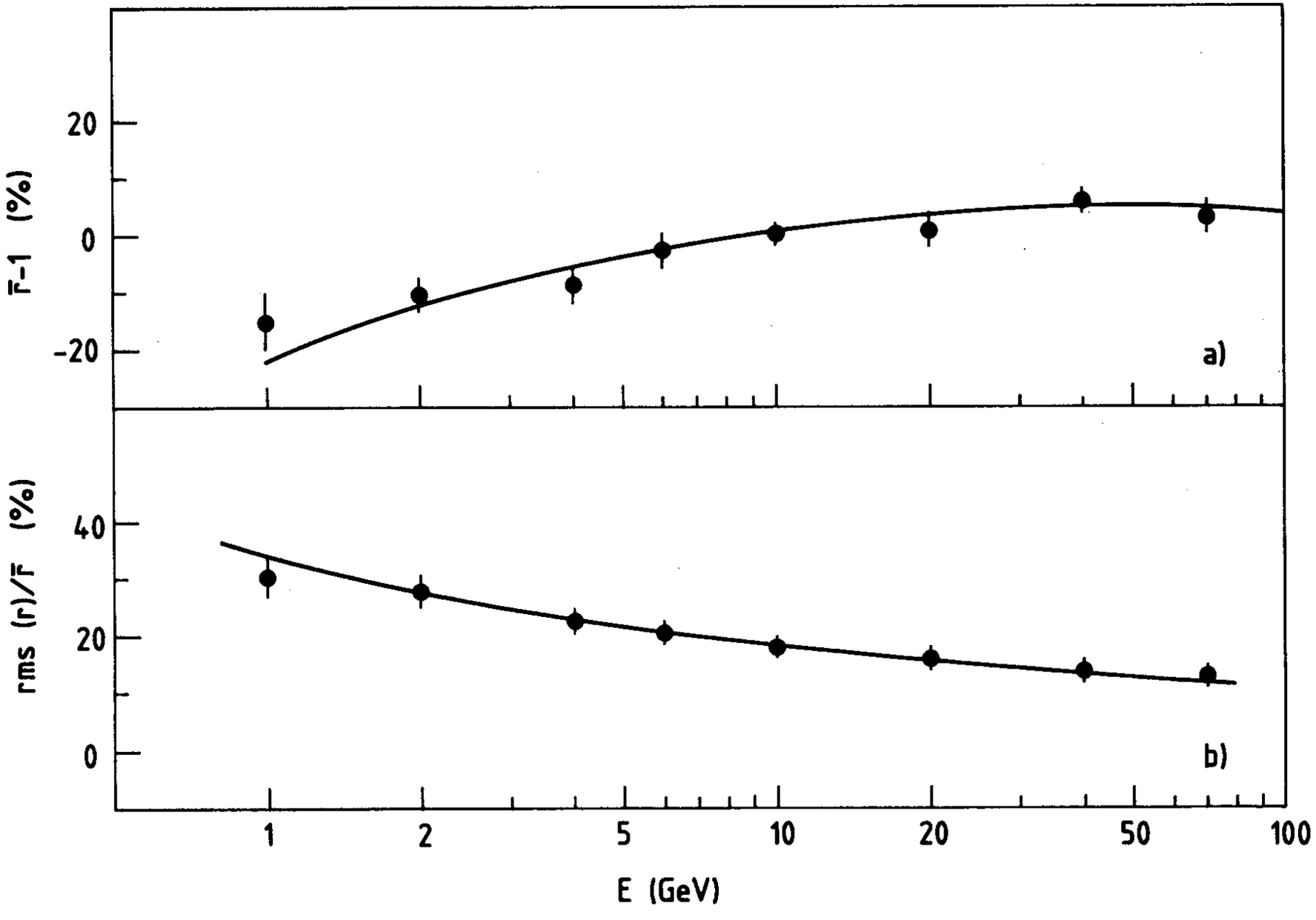

Fig. 38

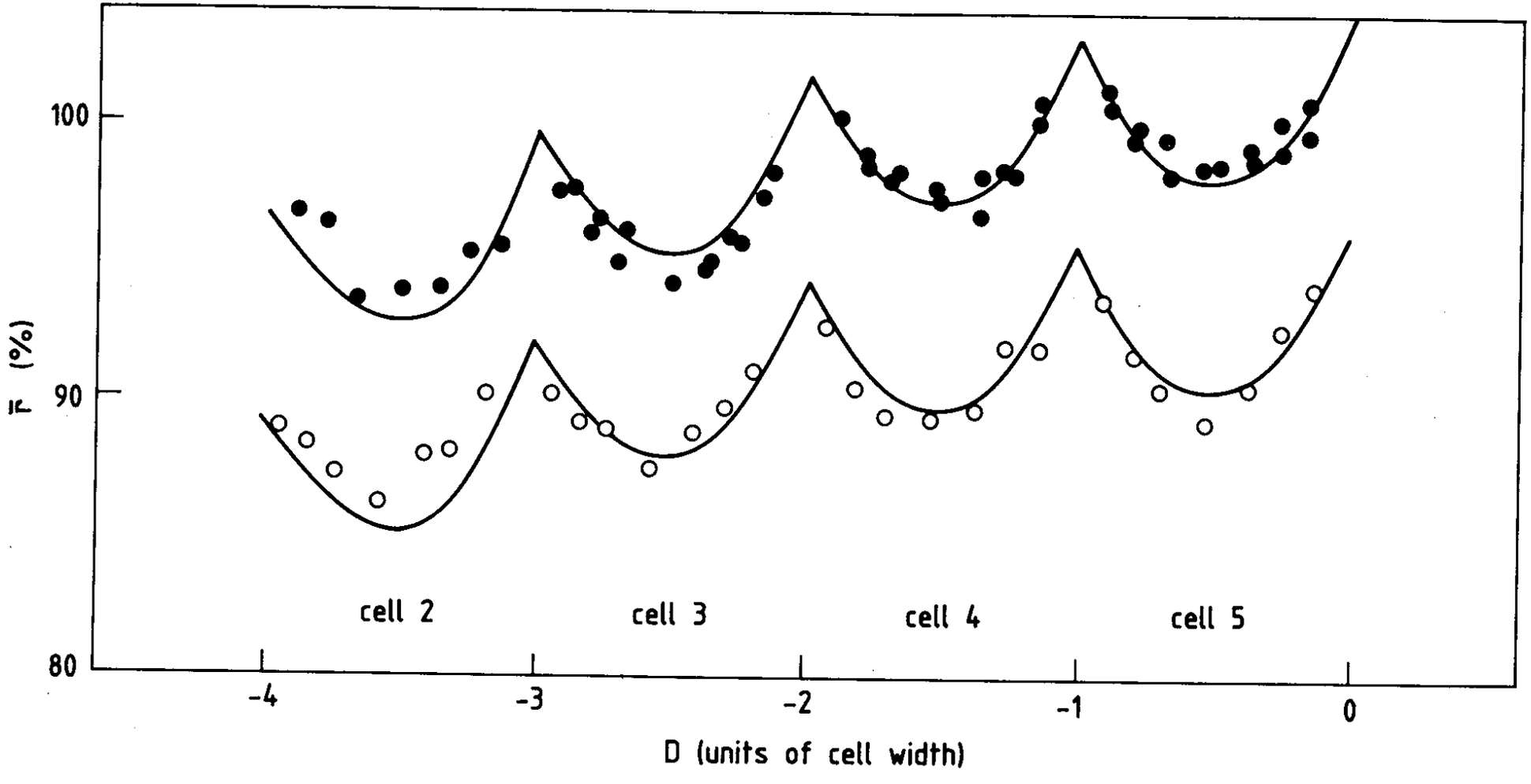
100
90
80
F (%)
cell 2
cell 3
cell 4
cell 5
-4
-3
-2
-1
0
D (units of cell width)

Fig. 39

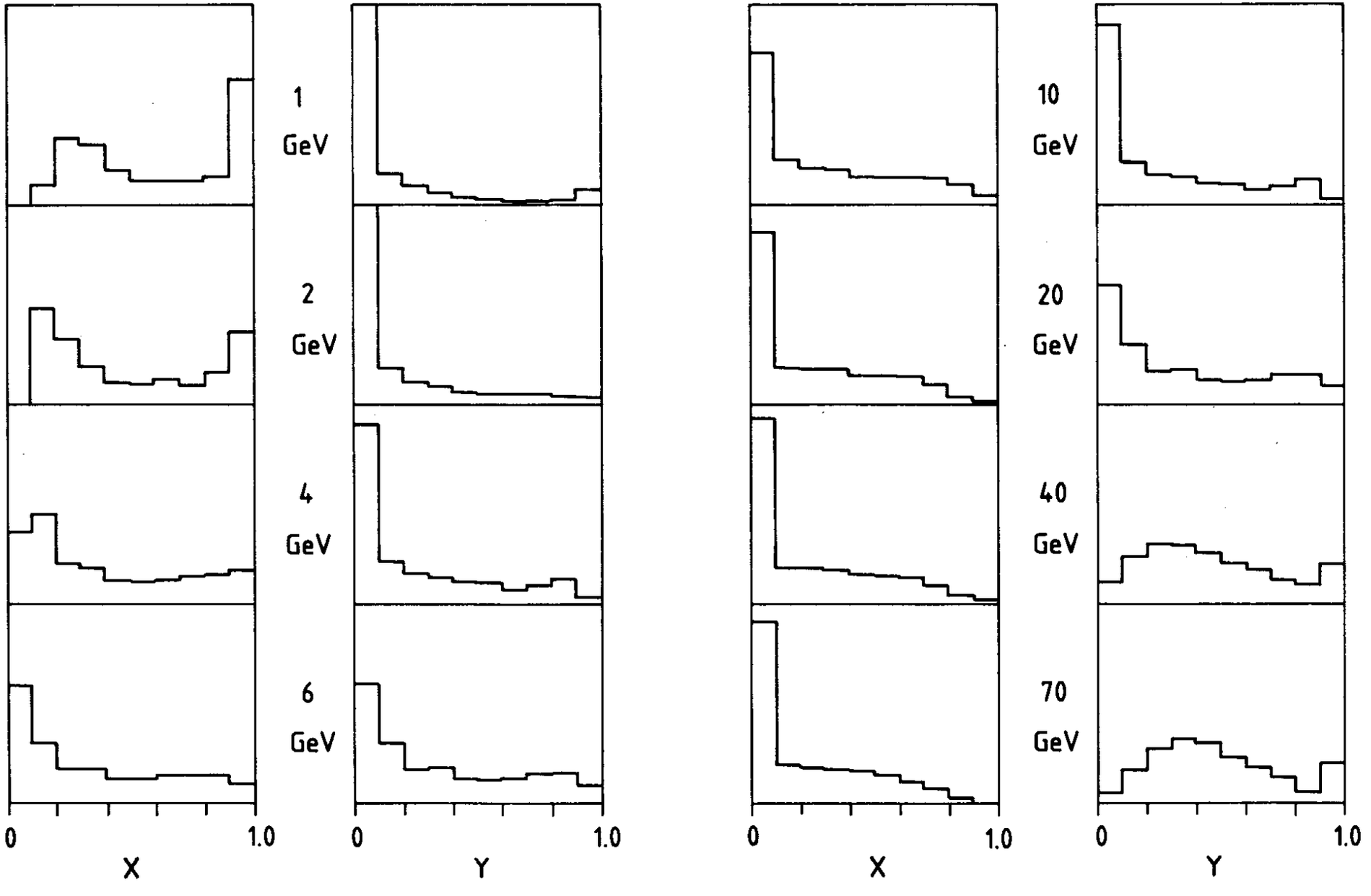
1
GeV
2
GeV
4
GeV
6
GeV
10
GeV
20
GeV
40
GeV
70
GeV
0
1.0
X
0
1.0
Y
0
1.0
X
0
1.0
Y

Fig. 40

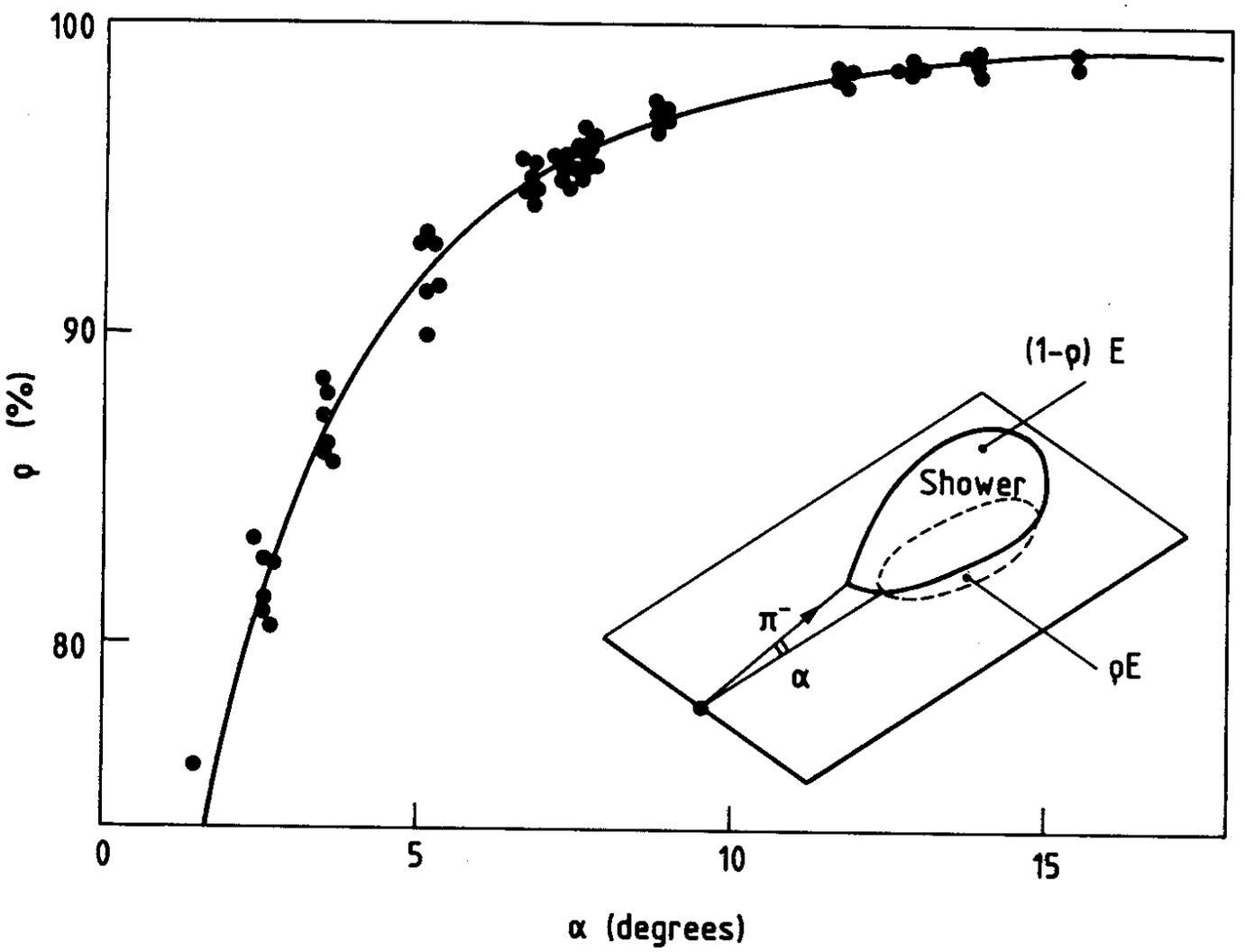

Fig. 41

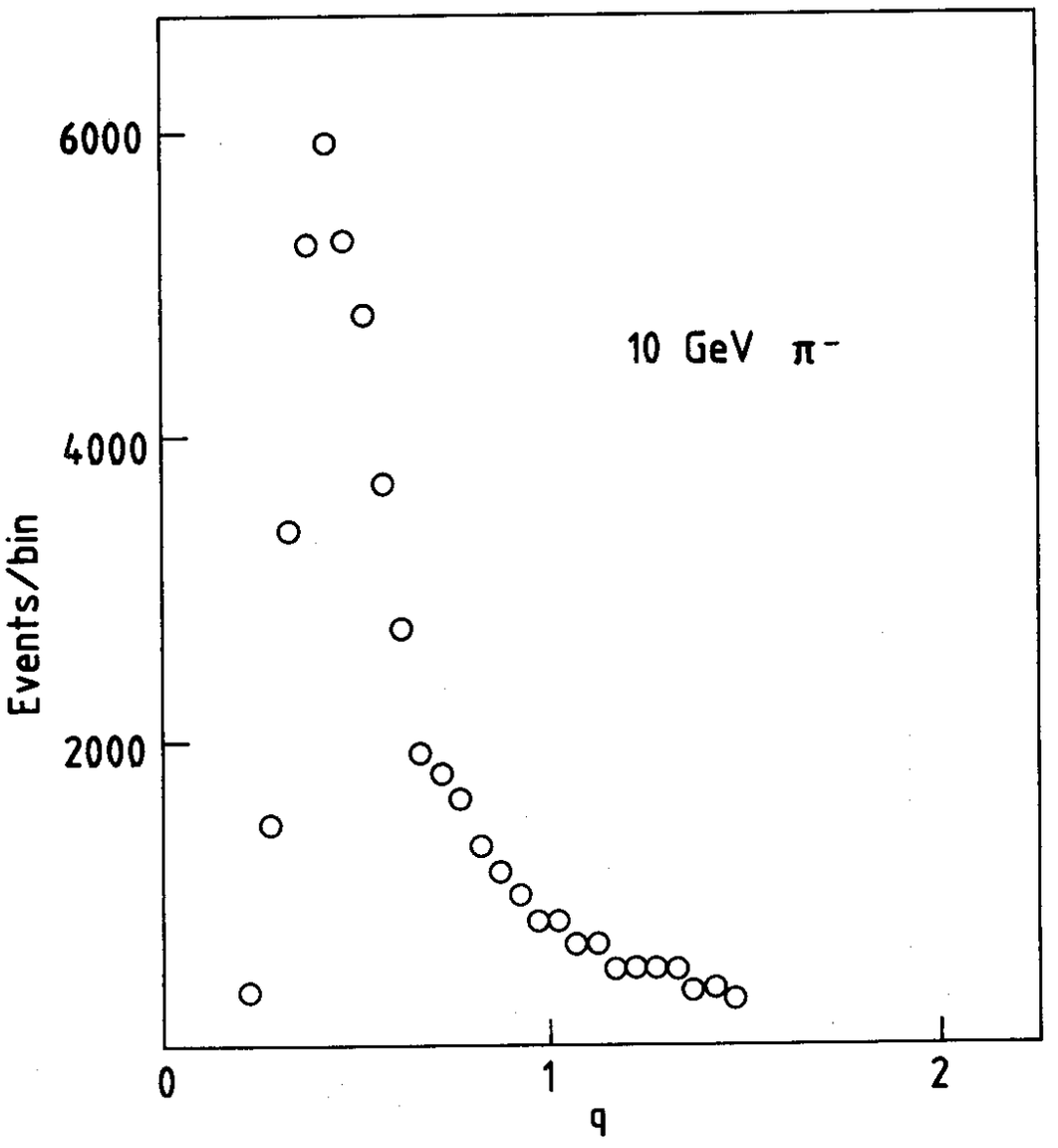

Fig. 42

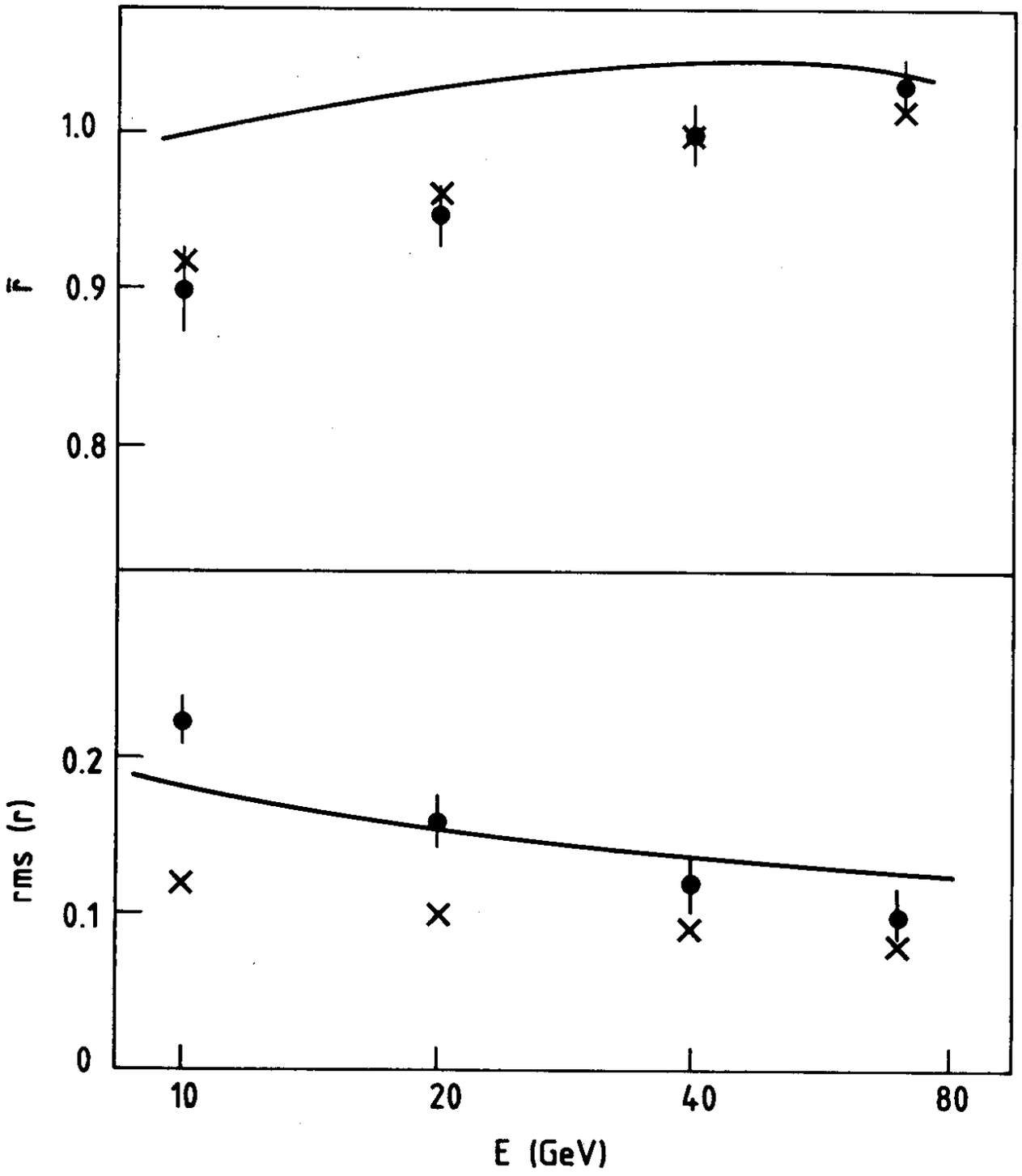

Fig. 43

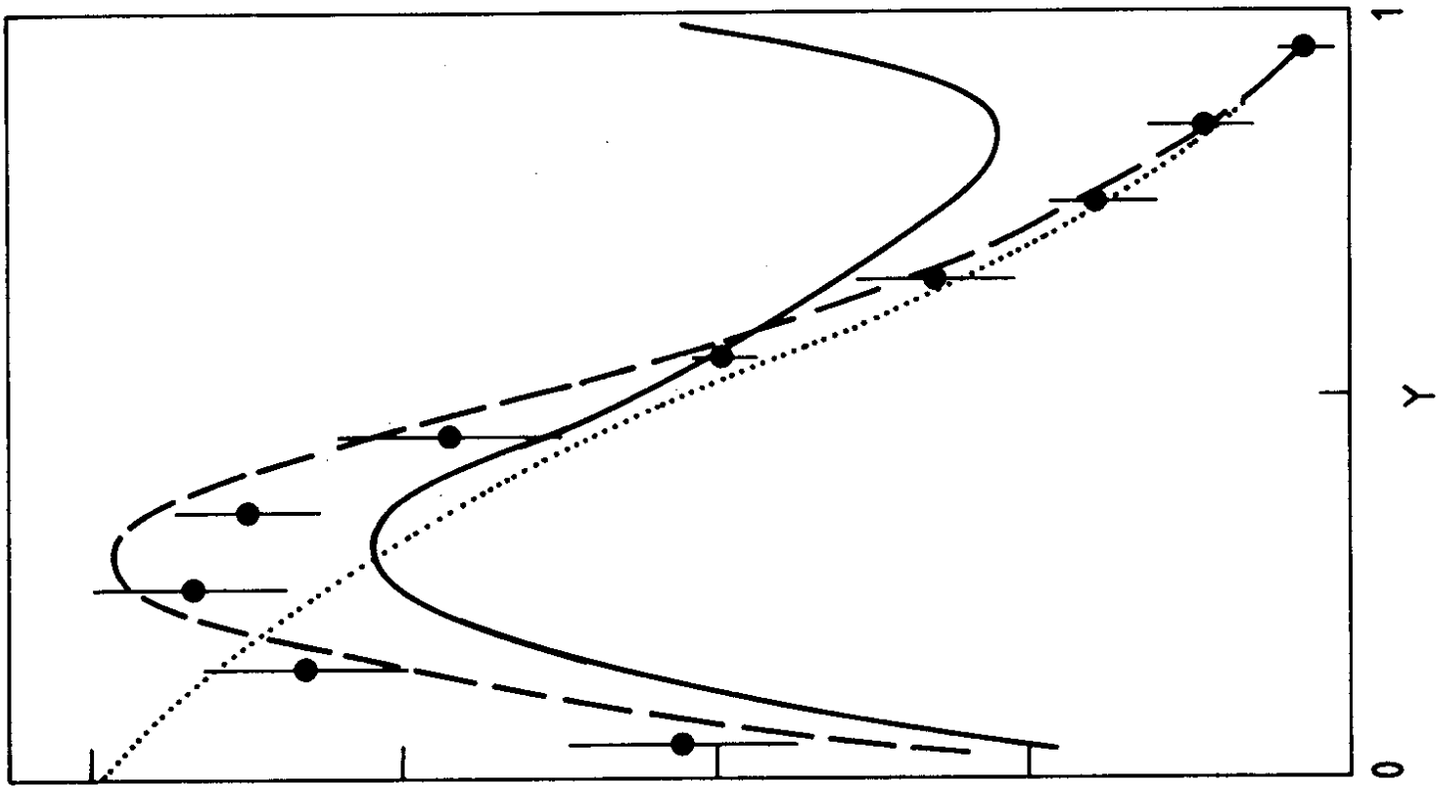

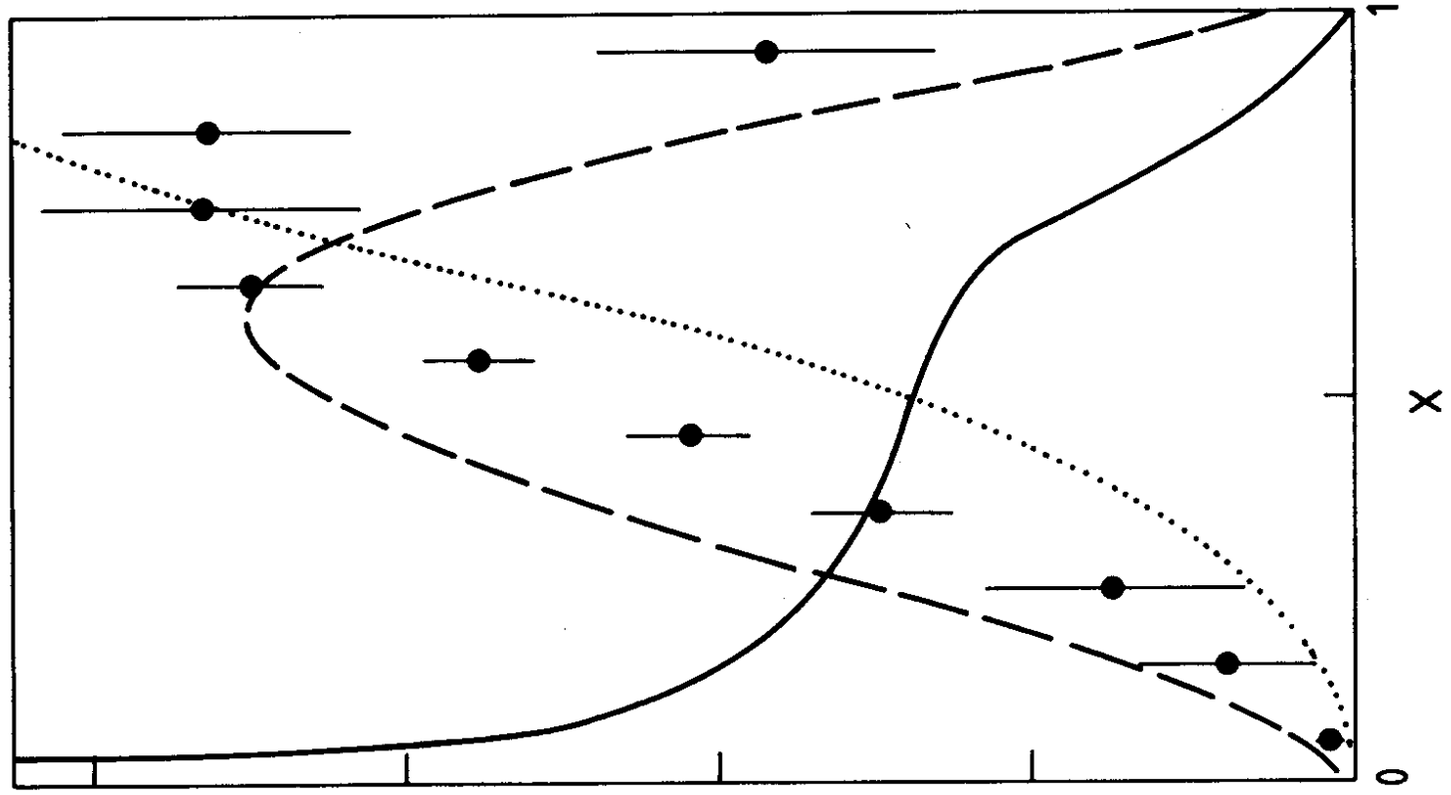

Fig. 44

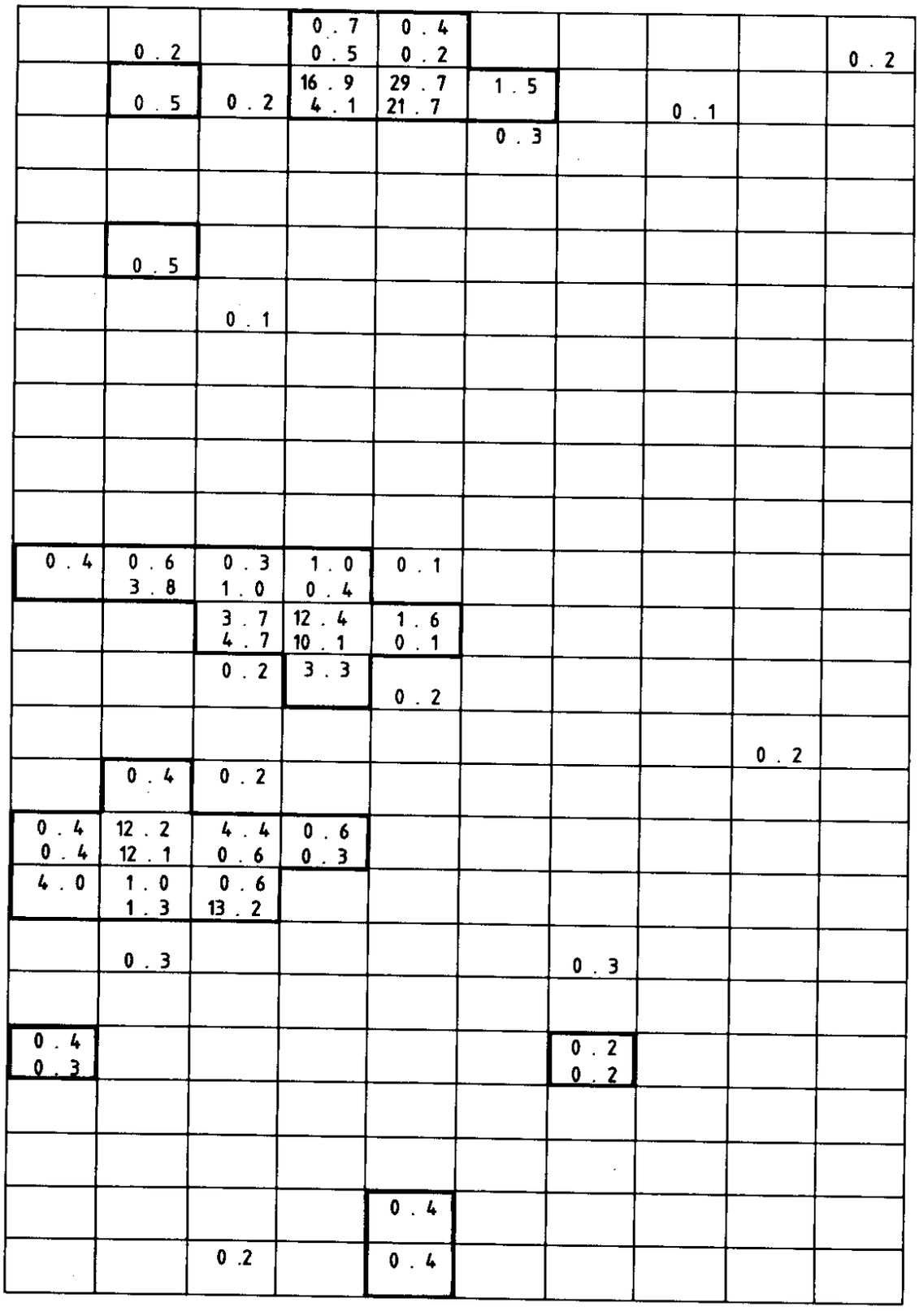
0 . 2
0 . 7
0 . 5
0 . 4
0 . 2
0 . 2
0 . 5
0 . 2
16 . 9
4 . 1
29 . 7
21 . 7
1 . 5
0 . 1
0 . 3
0 . 5
0 . 1
0 . 4
0 . 6
3 . 8
0 . 3
1 . 0
1 . 0
0 . 4
0 . 1
3 . 7
4 . 7
12 . 4
10 . 1
1 . 6
0 . 1
0 . 2
3 . 3
0 . 2
0 . 2
0 . 4
0 . 2
0 . 4
0 . 4
12 . 2
12 . 1
4 . 4
0 . 6
0 . 6
0 . 3
4 . 0
1 . 0
1 . 3
0 . 6
13 . 2
0 . 3
0 . 3
0 . 4
0 . 3
0 . 2
0 . 2
0 . 4
0 .2
0 . 4

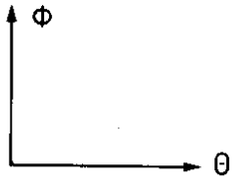
Φ
Θ

FIG. 45

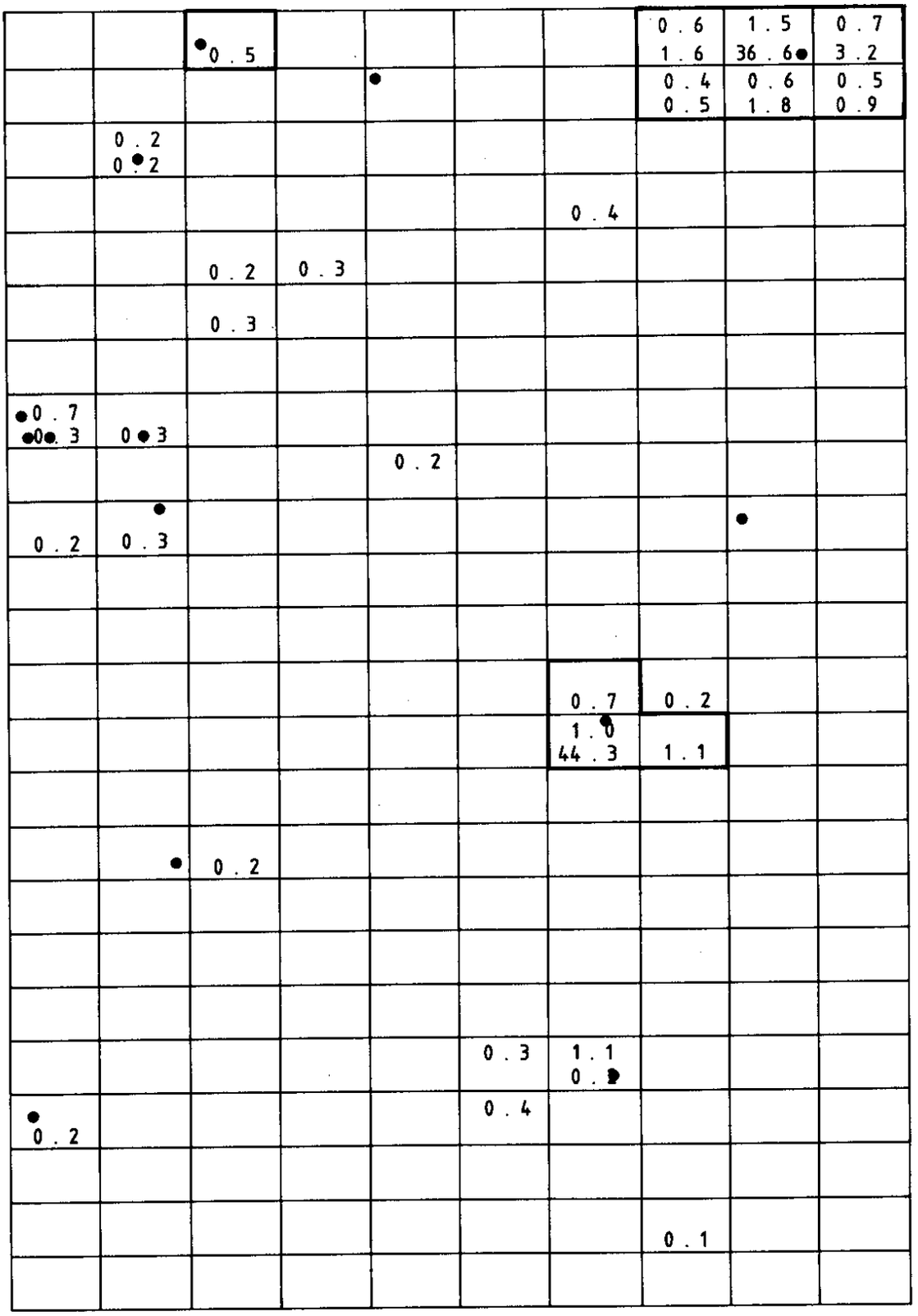
0.5
0.6
1.6
1.5
36.6
0.7
3.2
0.4
0.5
0.6
1.8
0.5
0.9
0.2
0.2
0.4
0.2
0.3
0.3
0.7
0.3
0.3
0.2
0.2
0.3
0.7
1.0
44.3
0.2
1.1
0.2
0.3
1.1
0.4
0.2
0.1
Φ
Θ

FIG. 46